Master thesis

A multi-organ-on-chip platform with integrated oxygen and TEER sensors for the brain-gut axis.

Stijn. F. Robben

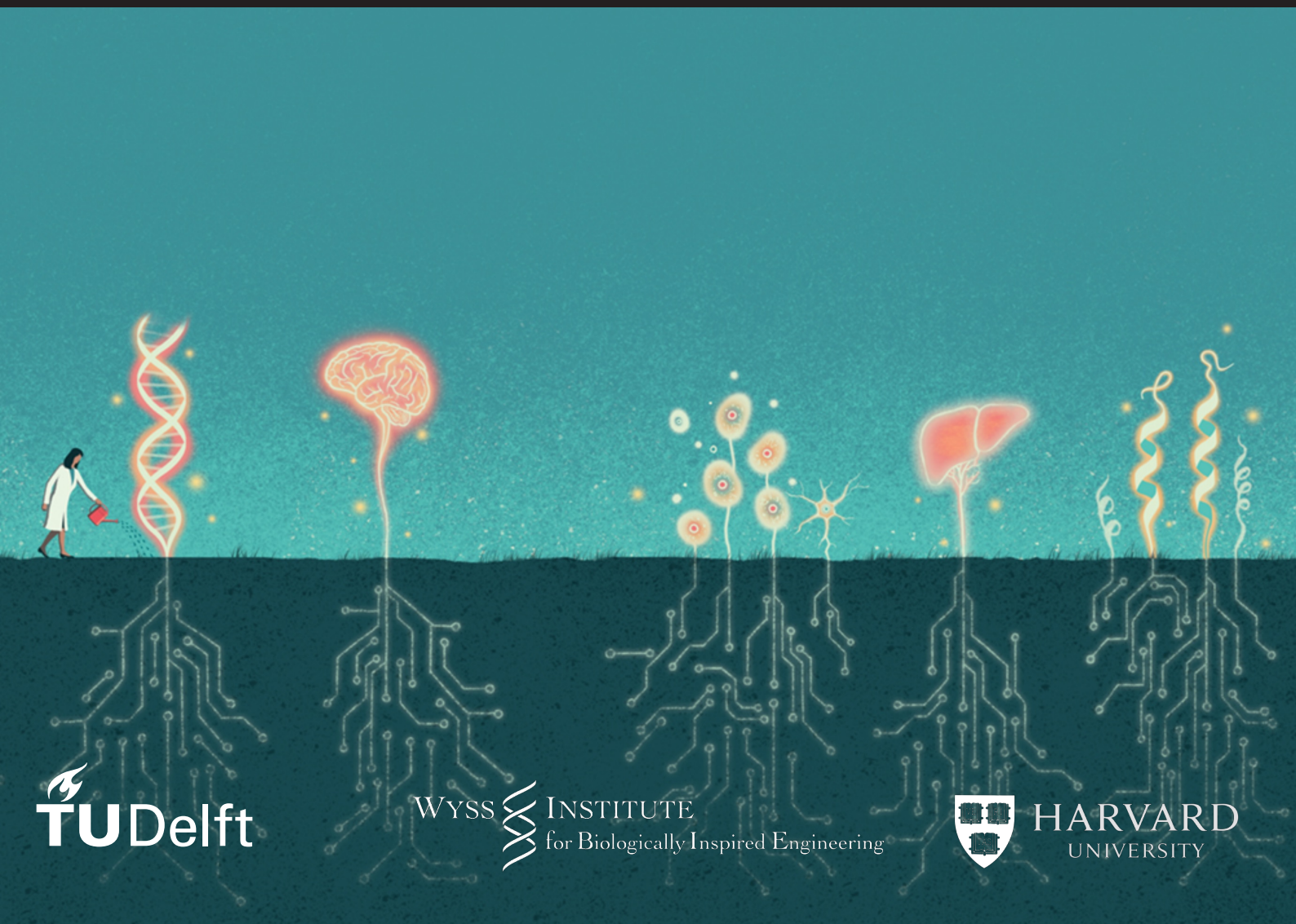

TU Delft

Wyss Institute for Biologically Inspired Engineering

Harvard University

Master thesis

A multi-organ-on-chip platform with integrated oxygen and TEER sensors for the brain-gut axis.

by

Stijn. F. Robben

at the Delft University of Technology,
the Wyss Institute for Biologically Inspired Engineering
and Harvard University

Student number:	4711580
Project duration:	February 1st, 2021 – August 8th, 2021
Supervisors:	Dr. ir. M. Mastrangeli
	Dr. ir. A. Sesay
Committee:	Prof. dr. ir. P. French
	Dr. ir. M. Ghatkesar
	Prof. dr. ir. L. Fratila-Apachitei

TU Delft

Wyss Institute for Biologically Inspired Engineering

Harvard University

Abstract

Predicting the effects of drugs before human clinical trails is at the heart of drug discovery and screening processes. To overcome limitations of conventional models used in pre-clinical research stages, advancements in fabrication, microfluidics, tissue engineering and sensor development allow for platforms that ever more closely emulate human physiology. Organ-on-chip (OoC) devices utilize these advancements to create a favorable cellular environment that more accurately resembles the human physiome. By combining these devices with integrated analytical components, an *in vitro* system is created that can real-time monitor the cellular activity and better predict the effects of drugs *in vivo*. Coupling multiple OoC devices together with microfluidic channels can even provide insights into the complex interactions between multiple organs. Specifically, the connection and the interactions between the gut and the brain is gaining in interest. It was found that this gut-brain-axis plays an important role in the development of various gastrointestinal and neurological diseases. Investigating the interaction between these two organs could provide valuable information about the functioning of the gut-brain axis.

The research presented in this document focused on creating a system that can link a gut OoC model (i.e., gut-on-chip) with a blood-brain-barrier-on-chip device with integrated TEER and O_2 sensors developed by the Wyss Institute in Boston. The final presented system is inexpensive and quick to fabricate, and has proven functional during experiments that included tissue culture. The main fabrication techniques include fused deposition modeling and CO_2 laser cutting. The final design includes a layered microfluidic component comprised of sheets of PMMA and SEBS material, housing the channels through which the medium is perfused. Results based on optical inspection showed that fibroblast growth was normal and fluid outflow was constant for 5 days of culture. Due to cell death prior to a second experiment the sensor functionality and linking could only partly be validated. Suggestions for future improvements include adding a mixing geometry and integrating sensor electronics to make the system more autonomous.

Preface

This Master thesis is part of the Master graduation project for the Medical devices & Bioelectronics track of the Master Biomedical Engineering at the Technical University of Delft. Prior to this thesis, a three months literature study was conducted and relevant parts are included. The two year curriculum of the Biomedical Engineering Master consists of 60 ECTS worth of courses , 15 ECTS in the form of an internship and 45 ECTS for work related to this thesis. All parts need to be finished successfully in order to graduate from the Master.

The thesis project consisted of a collaboration of TU Delft with the Wyss Institute for Biologically Inspired Engineering at Harvard University in Boston. The project consisted of fabricating micro-environments with integrated O_2 and TEER sensors, designing and manufacturing a system for linking two of these micro-environments via microfluidics and validating the system using cell culture. Additionally, the project focuses on the most efficient channel geometries for mixing two microfluidic flows with low Reynolds numbers inside rectangular channels.

I would like to express my gratitude to dr. ir. M. Mastrangeli for fuelling my interest in the OoC field and for providing me with guidance, feedback and help throughout my research. With your help and feedback on both professional and personal matters I was able to shape the project to my interests and execute the necessary research, all the while enjoying my time abroad. Special thanks goes out to dr. ir. A. Sesay and dr. ir. Z. Izadifar and the others of the biosensors team for familiarizing me with everything related to microfabrication, tissue culture and mechanical engineering. I felt very free to pursue my own interests at the Wyss Institute resulting in a great working atmosphere. Also many thanks to prof. dr. ir. P. French, prof. dr. ir. M. Ghatkesar and dr. ir. L. Fratila-Apachitei for partaking in my graduation committee. Finally, I would like to express my appreciation to everyone else at the Wyss Institute that provided a work environment that always allowed me to ask questions and make use of the available expertise.

Thank you Dick, for granting me the time to both conduct my research abroad and say goodbye to you.

Stijn. F. Robben
Delft, September 2021

Contents

List of Figures

List of Tables

List of Abbreviations

μCCA	Microscale cell culture analog
μECT	Micro-engineered cardiac tissue
AMF	Automated membrane fabricator
APTES	(3-Aminopropyl)triethoxysilane
BoC	Body-on-a-Chip
CNS	Central nervous system
DILI	Drug-induced liver injury
DMEM	Dulbecco's modified eagle serum
DMSO	Dymethyl sulfoxide
DPBS	Dulbecco's phosphate-buffered saline
ECM	Extracellular matrix
EGTA	ethylene glycol-bis(β-aminoethyl ether)-N,N,N',N'-tetraacetic acid
ER-1	Emulate reagent 1
ER-2	Emulate reagent 2
FBS	Fetal bovine serum
GPTMS	(3-Glycidyloxypropyl)trimethoxysilane
IBS	Irritable bowel syndrome
iPSC	Induced pluripotent stem cells
MOoC	Multi-Organ-on-Chip
NEAA	non-essential amino acids
NIL	Nanoimprint Lithography
OoC	Organ-on-Chip
PC	Polycabonate
PCB	Printed circuit board
PDMS	Polydimethylsiloxane
PET	Polyethylene terephthalate
PFA	Paraformaldehyde
pHEMA	hydroxyethyl methacrylate
PI	Polyimide
PLA	Polylactic acid

PMMA	Polymethylmethacrylate
PS	Polystyrene
PVC	Polyvinyl chloride
SEBS	Styrene-ethylene-butylene-styrene
SEM	Scanning electron microscope
TEER	Trans-epithelial electrical resistance

Symbols

B	blue color value
f	body force
c	concentration
ρ	density
D	diffusion coefficient
$\mathbf{J}_i$	diffusion flux vector
μ	dynamic viscosity
G	green color value
c_p	heat capacity
D_h	hydraulic diameter
v	kinematic velocity
u	mean flow velocity
M	mixing coefficient
m	mixing performance
c_i	normalized concentration
$\bar{c}$	normalized expected concentration
N	number of samples
∇p	pressure gradient
r	reaction rate
R	red color value

1 Introduction

Organs-on-chip (OoCs) are *in vitro* microfluidic systems that emulate the microstructures, functions and physiochemical environments of whole living organs more accurately than two-dimensional tissue models. While still in their infancy, OoCs hold the potential to bring benefits to a wide range of applications, enabling more human-relevant candidate drug efficacy and toxicity studies and providing greater insights into mechanisms of human disease and physiology. The most advanced OoC systems also have analytical components incorporated to allow for the quantification of cell characteristics [1].

Although OoCs hold an advantage over 2D models (e.g., a monolayer of cells in a culture flask) in terms of single-organ research, it is largely unknown what can be achieved by incorporating multiple organs to enable their interaction and more accurate evaluation of downstream metabolites. An example of such a connection is the interconnection between the barrier and the intestine. Recent studies have unveiled that the so called gut-brain axis is a bidirectional link between the intestine and the brain and is of importance for maintaining homeostasis. For example, people with mental issues like schizophrenia, autism or anxiety are over-represented in the group of people that are diagnosed with irritable bowel syndrome (IBS) [2]. In addition to digestion related issues, an imbalance in the human microbiome can result in severe mental issues like depression and behavioral problems [3].

The research goal of this project is to create and validate a compact and reliable system to link two organ-on-chip models with integrated O_2 and TEER sensors.

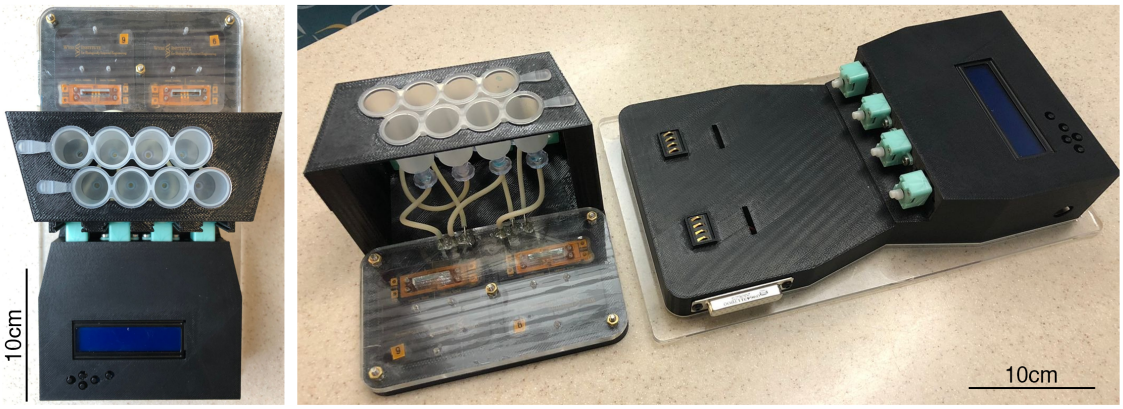

Figure 1.1: Preview of the final designed system. (a) Top view of complete assembly showing the pump unit with interface on the bottom, the fluid reservoirs in the middle and the sensor chips with the microfluidic component on top. (b) Overview of the complete design with the detached chips and reservoir component.

This research was conducted in the context of the Wyss Institute for Biologically Inspired Engineering[1] in Boston and the chips with integrated sensors have been developed by their biosensors team. Ideally, the linking system is simple and inexpensive to fabricate and compact enough to fit multiple systems in a single incubator. Also, the chips should be compatible with conventional imaging techniques when connected to the system.

An image of the final design of the proposed system developed in this work is shown in Fig. 1.1. The chapters in this thesis will each focus on a different aspect of the design and its functionality. The second Chapter will focus on the background of the OoC technology and on the gut-brain axis in particular. Chapter 3 elaborates on the design of the linking systems as well as the fabrication techniques. Chapter 4 discusses the best geometry to fully mix two fluid flows carrying organ specific nutrients in a rectangular micro channel. Chapter 5 describes two methods used to validate the functionality of the linking and the added value of the sensors. Finally, in Chapter 6, the results of the experiments are discussed together with conclusions and future recommendations.

[1] For more information about the Wyss Institute please visit: https://wyss.harvard.edu/

2

Background

This chapter serves as a general introduction to important topics in the OoC field, necessary for understanding the scope of the thesis project. It touches upon existing OoC models and linking systems, provides a foundation for comprehending the blood-brain barrier and gut physiology and discusses three types of sensors.

2.1. The need for Organs-on-Chip

Since the era of modern medicine, the drug development process has always been a multistage procedure. Two of the stages include preclinical and clinical research. During the preclinical stage, drugs undergo laboratory and animal testing to answer basic questions about safety. In a later stage, called the clinical research stage, the drugs are tested on humans to make sure they are safe and effective [4]. The aim of these stages is to ensure reasonable product safety while also facilitating the translation of scientific innovations into commercial products.

Although this approach to drug testing has existed for several decades, it is well recognized that the preclinical stages of current drug development procedures are not always suitable to fulfill the requirements of accurate predictions of drug responses and the way it extrapolates on humans. Despite several successes and advancements in drug development, testing and disease modeling, it remains a challenge to accurately replicate the human biochemical *in vivo* environment in conventional 2D cell cultures and animal models. In fact, only 70% of human toxicity is predicted from animal testing [5]. The main reason for this is that 2D cell cultures, in which the cells are cultivated in a monolayer, and animal models lack the biochemical, physical and cellular complexity specific to human tissue and therefore can not accurately predict the human body response to drugs [1].

This makes the current processes for discovering and developing new therapeutic drugs and treatments costly and complex. In 2018, 90% of the drugs that entered clinical trails failed, the time for a newly developed drug to enter the market could take as long as 15 years and the cumulative development costs could be as high as $2.6 billion [6].

To overcome the limitations of 2D cell culture models, the use of micro-fabrication, bioprinting, and microfluidic technologies create new possibilities for adding a third dimension to conventional methods. In this regard, OoCs are now at the center of much of the activity in the field [7]. OoC devices are a class of microengineered biomimetic systems, containing microfluidic channels lined by living cells, that allow to create biological models. In these microfluidic devices, tissues can be cultured in an environment that better replicates the *in vivo* microenvironment of that tissue by introducing geometrical, mechanical, electrical or biological factors [8]. Additionally, it is possible to integrate real-time readouts (from imaging systems and sensors) to monitor the cells [9]. Liu et al (2018) summarized the most important differences between conventional 2D culture models and 3D OoC models in Table 2.1, further highlighting the improvements OoC technology can bring [7]. Ultimately, it is the aim to have OoC devices incorporated into the drug development process, reducing the need for animal testing and human preclinical trails (Fig. 2.1).

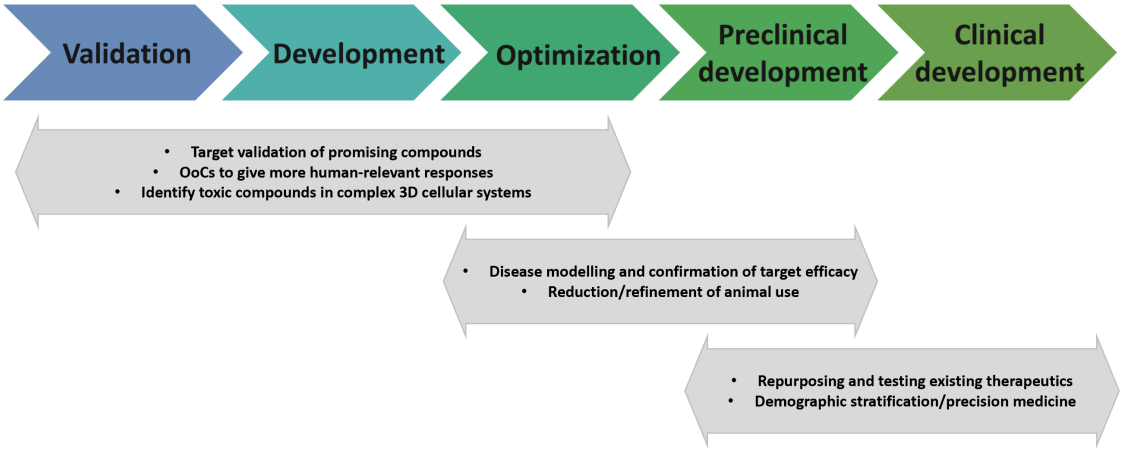

Figure 2.1: A simplified schematic of a potential drug development process with OoC devices adopted, excluding post-approval monitoring by regulatory bodies [10].

While OoC devices are useful products in the first step of predicting the human tissue responses to a drug, true effects are often the result of unpredictable multi-tissue cross-talk [11]. Single-organ OoC devices are often based on a limited number of cell types whose architecture does not represent the respective functional units of organs in the human body . This is why over the past years, OoC technologies have progressed towards the integration of multiple organ functions on a chip [12, 13]. These so called 'Multi-Organ-on-Chip' (MOoC) or 'Body-on-a-chip' (BoC) devices consist of separate chambers, each containing a different OoC device, connected by microfluidic channels which emulate blood circulation. The ultimate goal of these MOoC efforts is to develop a human experimental platform that could refine, reduce and eventually replace animal testing, by providing more relevant data that track human response and toxicity [14].
To analyse the effects of drugs on cells and to monitor or influcence the microenvironment, a variety of (bio)sensors can be incorporated into the microfluidic devices. Such microsensors can quantify important physiolocial and biochemical parameters such as oxygen concentration, pH, flow rate, pressure, trans-epithelial electrical resistance (TEER) [15].
This chapter aims to introduce the most relevant definitions regarding OoC technology, the gut-brain axis and important sensors.

Table 2.1: Comparison between 2D and OoC disease modeling systems [7].

	Conventional 2D systems	**Organ-on-chip**
Production method	Differentiated, grown on rigid flat surfaces as monolayer, fast	Seeded in engineered chambers with perfusion; fast
Maturation	Immature	Improved but still lacking
ECM	Limited composition and contact with cells	Depends on platform design
Tissue architechture	Absent	Complexity depends on platform design
Diffusion of signal factors and nutrients	Short distances (through cell membranes); usually receiving supraphysiological doses	Precisely controlled temporal and spatial gradient
Vasculatirzation or perfusion?	No	Yes
High throughput feasibility; contractability; scalability	Present; high; absent	Present; very high; microscale
Variability; reproducibility; difficulty of use	Low; high; easy	High; sometimes low; difficult
Possibility for genome editing	Straightforward	Straightforward
Characterisation and analyses	Limited, but easy cell retrieval	Real-time tissue/organ function analyses possible, with easy cell retrieval

2.2. Organs-on-Chips

In 1990, the field of biomicrofluidics exploded when polydimethylsiloxane (PDMS) was introduced. This optically transparent, soft elastomer was ideal for biological applications on the small scale [16]. The first time the concept of mimicking the organ-level function of human physiology or disease using cells inside a microfluidic chip had been published was in 2004. Michael Shuler et al. (2004) demonstrated a system that captured the systemic interaction between lung and liver on a one square inch silicon chip The term organ-on-a-chip was first used by Donald Ingber in 2010 when his team developed a microfluidic chip to capture organ-level functions of the human lung [17].

Since then, many more milestones have been reached (Fig. 2.2) that contributed to the development of current OoC technologies [19].
As a result of these technologies, a wide variety of OoC devices has been created. Every device has its own unique qualities and characteristics but they all serve the same purpose which is to expose cells to mechanical, electrical, topological or biochemical stimuli to resemble the natural *in vivo* environment. Since the start of the OoC research field, numerous OoC systems have been explored including brain, intestine, lung, heart, kidney, skin, liver an uterus among many others [17, 20–26].
As the OoC field emerged as a result of developments in tissue engineering, many OoC devices consist of key components that are also used in tissue engineering including microfluidics, living cell tissues, stimulation or drug delivery and sensing [27]. The microfluidic component refers to the use of microfluidics to create a system of culture fluid input and waste liquid discharge during the culture process. The living cell tissue component refers to the cells or cell lines that are being cultured in the device. The stimulation or drug delivery component of the OoC device induces the mechanical, electrical or biochemical stimuli to resemble the natural *in vivo* environment of the cultured cells. Finally, the sensing component is used for detecting and compiling data about the state and functionality of the cultured cells or of the induced stimuli. Each of these four components will be described more in-depth in the following subsections.

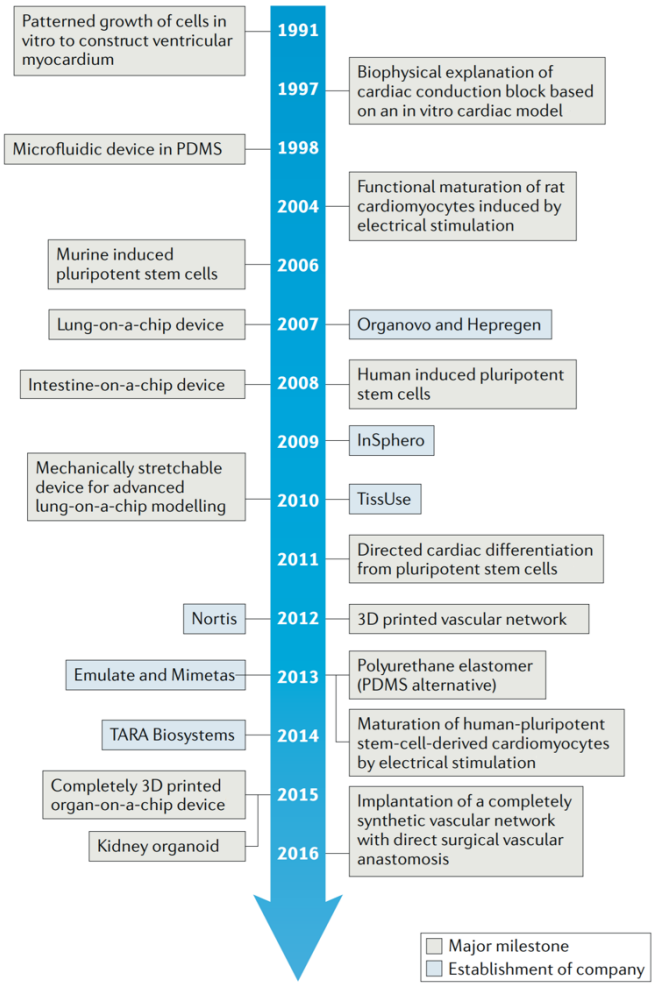

Figure 2.2: Major milestones in organ-on-chip technology and establishment of organ-on-chip companies [18].

2.2.1. Microfluidics

Although the extent to which microfluidics can be used in OoC devices is highly dependent on its design, microfluidic technology has made a massive impact on the reliability and functionality of OoC devices. Fluid flow is so vital, because at the smaller scale, viscous forces are dominant. When the diameter of a channel is less than 1mm and the flow rate is very low, the flow tends to become laminar and allows for the production of physical and chemical gradients [28]. Because the microfluidics field does not only entail the behavior of fluids, but also includes the fabrication of microchannels it is important to get an understanding of the fabrication techniques that are utilized.
The most used materials in the fabrication of microfluidic structures include PDMS, polymethylmethacrylate (PMMA) , polycarbonate (PC) , polystyrene (PS) , polyvinyl chloride (PVC) , polyimide (PI) , and the family of cyclic olefin polymers [29]. These materials are then manipulated by using various techniques in

microfabrication, such as etching, patterning or microforming [30]. Another fabrication technique is soft-lithography. Soft-lithography includes a family of techniques involving a soft polymeric mold replica from an original hard master. The mold masters are fabricated by photolithography in order to define a stamp pattern. The stamps are made by curing a prepolymer onto a mold master [31]. Many other lithographic methods for the fabrication of micro-nanopatterns in soft-lithography exist but will not be discussed in this review. A third technique is hot embossing. This technique is similar to thermal nanoimprint lithography (NIL) , which creates patterns by mechanical deformation of imprint resist and subsequent processes, and is characteristically used to fabricate microfluidic-based products and OoC components. It is a low-cost and flexible fabrication method with unique potentialities to build nanoimprint patterns with high-aspect-ratio microstructures. The forth used technique for the fabrication of the microfluidic component is injection molding. The component is produced by injecting molten material into a mold where it cools and hardens subject to the mold configuration [32].

2.2.2. Living tissues

Another significant component of an OoC device is the tissue grown inside. For OoC development, cell sources currently range anywhere from primary tissue biopsies, to commercially available cell lines, to stem cell-derived cell populations. Primary cells derived from tissue biopsies may be grown and maintained in culture for long periods of time and therefore allow for longer term studies than 2D cell culture systems. Other cell sources are induced pluripotent stem cells (iPSCs) from reprogrammed adult somatic cells, and are often used in OoC platforms. iPSCs may be derived from patients and represent a potentially unlimited cell source, but this technology is still evolving [10].

2.2.3. Stimulation or drug delivery

The *in-vivo* environment differs greatly between organs. In order to replicate this environment, some cell cultures require mechanical stimuli (e.g., lung cells) to create a contractile movement while other prefer electrical stimli (e.g., heart cells). As mentioned before, the different stimuli include topological, mechanical, electrical or biological factors. Within each category many different ways of inducing the stimulus to the cell tissues exists.

2.2.4. Sensing

One of the largest advantages of OoCs is their ability to real-time monitor cell activity. Although the field of OoCs evolves over time, there is still need for more sophisticated OoCs with integrated sensors that will provide continuous information about the viability and metabolic activity of the tissue constructs/organoids in real time. A distinction between sensors can be made based on their purpose. Sensors exist to monitor the culture environment, cell behaviour or stimulations (electrical, chemical or mechanical) [33]. There is a wide variety of functionality between the different sensors to detect the physical or biological parameters, most of which will be discussed in more detail in chapter 3.

2.3. Key priority organs

With the advance in modern techniques, various pharmaceutical companies and academic research groups have shown exceptional improvements by developing more effective and lower cost drug discovery models just in recent years. Every organ model requires specific properties regarding microfluidics, cell tissues, stimulation and sensing. Ronaldson et al. (2018) created an excellent overview of different OoC models and their design considerations, used cell types and readouts shown in Table 2.2 [34]. The organ models are discussed more in depth in the following sections followed by an overview of several MOoC systems.

Table 2.2: Overview of selected OoC models with design considerations, cell types and readouts [34].

Organ Type (Functional Unit)	Design Considerations	Cell Types Used Currently	Readouts	Ref
Gut	Drug absorption, requires a large surface area, viavilli and microvilli formation, mucosa barrier, and symbiotic bacteria present	Cell lines	Transepithelial transport, absorption, toxicity, responses to bacteria and cytochrome P450 3A4 isoform drug metabolism	[22]
Brain/BBB	Selective drug penetration and interactions between endothelium, pericytes, and astrocytes/neural cells	Primary, cell lines and iPSCs	transendothelial resistance (TEER), permeability and drug transport	[35]
Liver (hepatic lobule)	Drug metabolism, cytochrome P450 interaction, and hepatocyte and fibroblast co-culture	Cell lines and iPSCs	Albumin and urea production, cytochrome P450 enzymatic activity, metabolite conversion and drug-induced liver injury (DILI)	[36]
Heart	Contractility and electrical activity	iPSCs	Beat rate, force, excitation threshold, maximum capture rate, and contractility	[37]
Lung (alveoli)	Air-liquid interface and pulmonary drug absorption	Cell lines	Cell imaging and dissolved gas concentration	[1]
Kidney (nephron and proximal tubule)	Drug clearance and proximal tubule epithelium exposed to shear stress	Primary and cell lines	Fltration, reabsorption, urea concentration, epithelial cell polarization, albumin transport, glucose reabsorption, alkaline phosphatase activity, and permeability glycoprotein efflux transporter	[38]

2.3.1. Gut

The main function of the human gut system is to carry out digestion, absorption, secretion and mobility as well as establishing a protective epithelial barrier between the digestive environment and the body [39]. Additionally, it regulates systemic physiology by metabolizing drugs, communicates with other organs and it contains an enteric nervous system that forms a part of the gut-brain axis [3]. Also, the gut system is the major site at which commensal microbes of the gut microbiome live and interact with gut lymphoid tissue and the host immune system [40].

An example of a gut-on-a-chip model was created by Kim et al. (2016) [41]. They used Caco-2 intestinal epithelial cells in flexible microfluidic channels that produced the fluid dynamics and its peristaltic movement. This produced undulating epithelium columns with polarized Caco-2 cells and multiple differentiated intestinal cell types including enteroendocrine cells, Panteh cells, and differentiated Goblet cells that secrete large amounts of mucus found in living small intestine. Later research on the same model could even follow the intestinal inflammation produced by bacterial overgrowth by studying the pathophysiology over a time lapse of weeks, which is an outstanding model for several applications such as creating human intestinal disease models and gaining insights into gut pathophysiology [41].

2.3.2. Brain

As one of the most complex organs, the brain has always been of great interest to medical scientists whose research interests are on neuroscience, neurodegenerative diseases, electrophysiological, and pharmacological studies on blood-brain barrier. The BBB selectively controls the passage of specific molecules into the central nervous system (CNS) . OoCs emulating the function of the BBB would allow testing whether a drug that is targeted at the CNS can actually pass through the BBB to act on its intended target [34].

Current models are based on culturing cells on a membrane with endothelial cells on one side and astrocytes with or without supporting pericytes on the other side [21]. By using TEER as a functional readout parameter, the use of microfluidic perfusion has been shown to physiologically increase barrier function and provide more predictive drug responses [42]. In order to develop a more faithful BBB model, the neurovascular unit OoC was designed to couple a vascularized chamber with a brain chamber through a porous membrane [43].

In addition to the BBB, other structures of the brain are also of great importance because the complexity of the human brain makes it difficult to study on non-human models. This is where the development of 3D cerebral organoids from iPSC-derived neuroectodermal tissues show great promise as an *in vitro* model of brain development [44].

2.3.3. Liver

The liver is crucial to life due to its high metabolic activity. It performs more than 500 functions, some of which can be summarized as removal of toxins (detoxifications), storing of fat-soluble vitamins (A, D, E and K) and regulation of blood glucose levels while synthesizing clotting factors. Additionally, it has an effect on blood circulation and filtration and releases bile, proteins, carbohydrates, cholesterol and so on [46]. Besides the fact that the liver has many important functions, it also suffers majors damage from chronic diseases and viral infections despite its highly regenerative capacity [47]. These factors make the liver a target of drug-induced toxicity and hepatotoxicity.

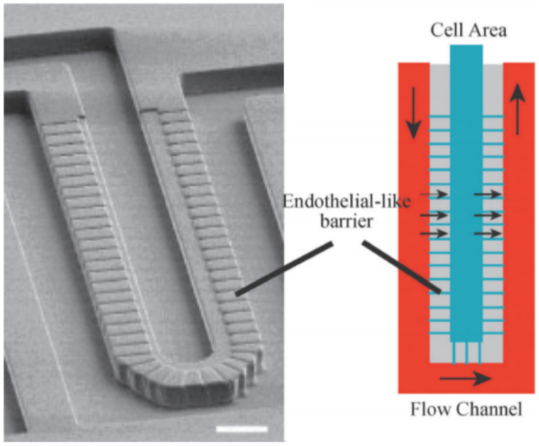

Figure 2.3: Photograph and schematic representation of *in vitro* microfluidic liver sinusoid with the endothelial barrier layer [45].

In the early days of OoC development, Lee et al. (2007) created a PDMS-based microfluidic channel to mimic liver anatomy (Fig. 2.3). They used epoxy-based negative photoresists (SU-8) for silicone replicate molding with photo-lithography to form fluid flow and cell-loading channels [45]. The main features of the device included extensive cell-cell contact, continuous nutrient exchange, mimicking of the natural endothelial barrier layer, and culturing of primary hepatocytes for over 7 days without decreasing viability. A downside of the proposed design was the lack of experiments related to waste and toxicity.

A few years later, Bhushan et al. (2013) constructed a microfluidic device to mimic functional human liver tissue of the acinus and oxygen gradient that contains four different cell types of hepatocytes, stellate cells, Kupffer cells and endothelial cells [48]. A key feature of the model is that it has fluorescent markers, which can visually indicate changes in cell function when a toxic drug is added. This allows for the investigation of drug-induced liver injury such as fibrotic scarring, cell damage from free radicals and liver failure.

2.3.4. Lung

The lung is the primary organ in the respiratory system. In the respiratory system, the trachea transfer the inhaled air into the lungs through the tubular branches, also called bronchi. Bronchi are divided into smaller branches ending with the alveoli, where the exchange of gases occurs. Oxygen passes from the air into the blood and carbon dioxide passes from the bloodstream into the atmosphere through the alveoli, which are covered with capillaries carrying blood plasma. The membrane between the alveoli and capillaries consists of epithelial cells from the alveoli side and endothelial cells from the capillary side [49].

One of the first OoC models to recapitulate human lung function was created by Huh et al. (2010). Their device was formed by two closely apposed microchannels separated by a flexible, porous and thin membrane (10μm) from PDMS that was coated with extracellular matrix (ECM) . An overview of the device is shown in Fig. 2.4. Human alveolar epithelial cells and human pulmonary microvascular endothelial cells were cultured on the opposite sides of the membrane and air was introduced into the epithelial compartment, while the bottom microchannel was filled with endothelial cells and was infused with a blood-like liquid. In order to mimic human breathing, a vacuum was applied to the microchambers to enable mechanical stretching of the PDMS membrane. This system was the first of its kind and has successfully allowed visualization and characterization of inflammatory processes and response to bacteria numerous times[17].

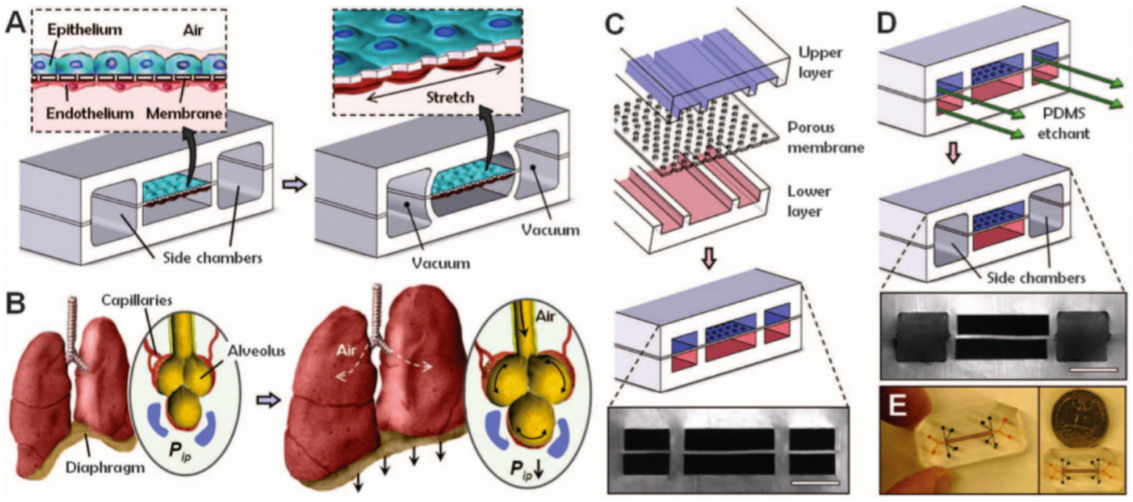

Figure 2.4: Schematic representation of a lung-on-a-chip microdevice. (A) PDMS microchannels with ECM-coated porous and flexible PDMS membrane representing an alveolar-capillary barrier. Vacuum is applied to the side chambers to induce mechanical stretching. (B) Schematic of the lung functioning principles. (C) Device construction. (D) PDMS etchant is used in the side chambers to remove the membrane for vacuum applications. (E) Images of lung-on-a-chip microdevice [17].

2.3.5. Heart

The cardiovascular system, which consists of the heart, blood, blood vessels and the lymphatic system, has a crucial function. It is responsible for the transport of O_2, CO_2, nutrients, cellular waste and hormones by pumping blood throughout the body. It manages many sensitive processes in the body very well. During diastole, the ventricles are filled with blood properly and the degree of contractions is sufficiently adequate. The heart includes permanent cells, such as cardiomyocytes, cardiac fibroblasts and endothelial cells, and transient cell groups which include lymphocytes, mast cells and macrophages. These two groups of cells have complex interactions between each other and have an important influence on the functioning of the cardiac system [46].

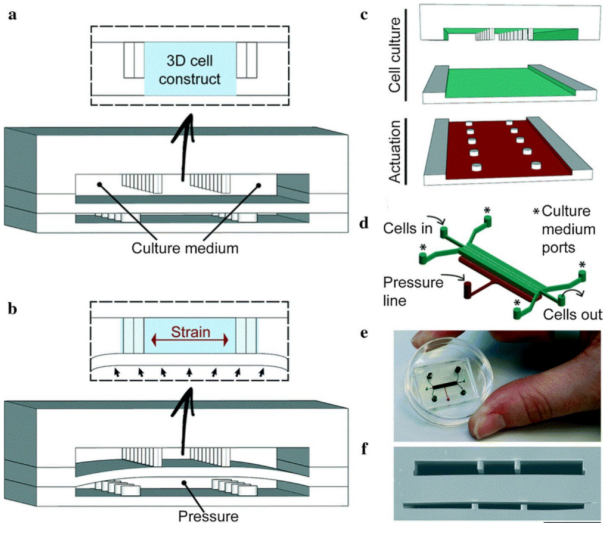

Figure 2.5: 3D heart-on-a-chip. (a) Two separate PDMS microchambers. The compartmentalized microchambers are positioned in the central channel to create a 3D construct, whilst the medium is replaced trough side-channels; (b) the lower end of the compartment is pressurized to deform the PDMS membrane and compress the 3D structure; (c) PDMS layers are aligned and irreversibly combined. Upper layers are present in the culture chamber and the drive chambers represent the lower layers; (d) 3D illustration; (e) Actual chip; (f) SEM of the chip cross-section [37].

In the past, the correlation between electrophysiological and contractility properties of cardiac cells was observed from a single cardiomyocyte. These models do not give the whole response and structure of cardiac tissue. This is why Grosberg et al. (2011) created a 'heart-on-a-chip' based on a muscular thin film technique that comprised a ventricular myocardium on an elastomeric thin film [50]. With this device researchers were able to study contractility, combined with a quantification of action potential propagation and cytoskeletal architecture in multiple tissues in the same experiment.
Since then, many techniques have been utilized by researchers to mimic the *in-vivo* environment of the heart including 3D printing technologies, hydrogels, surface acoustic waves and many more [51–53]. Another interesting device was created by Marsano et al. (2016), shown in Figure 2.5, which allowed for the generation of mature and highly functional micro-engineered cardiac tissues (μECTs) , from both neonatal rat and human induced pluripotent stem cell-derived cardiomyocytes. The stimulated μECTs showed superior cardiac differentiation, as well as electrical and mechanical coupling, owing to a remarkable increase in junction complexes. Mechanical stimulation also promoted early spontaneous synchronous beating and better contractile capability in response to electric pacing [37]. Their device has been used in many studies investigating cardiac cell functioning.

2.3.6. Kidney

The kidney is responsible for the maintenance of osmotic balance and drug excretion. Filtration and reabsorption take place in the nephrons that consist of the glomerulus, renal capsule and renal tubule. Kidney toxicity can lead to an irreversible loss of renal filtration, which highlights the need for drug screening systems [9].
Jang et al. (2010) were the first to produce a multi-layered microfluidic system (Fig. 2.6a) [54]. Mouse kidney medullary collecting duct cells were used in the device to simulate renal filtration. It provided a biomimetic environment that enhanced polarity of the inner medullary collecting duct through promoting cytoskeletal reorganization and molecular transport in response to hormone stimulation. The same device was used to culture human primary renal epithelial cells, which allowed for the first ever toxicity studies of human primary kidney cells.

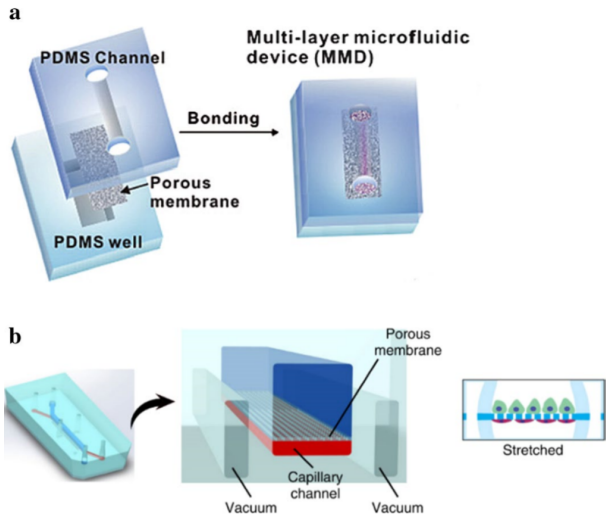

Figure 2.6: (a) Kidney tubular chip. Sandwich assembly of the PDMS channel, porous membrane, and PDMS reservoir; (b) the channel can replicate the urinary cavity and capillary lumen of the glomerulus. The porous flexible PDMS membrane can be used to functionalize the protein laminin to mimic the glomerular basement membrane. Cyclic mechanical pressure to the cell layer via vacuum stretching of the PDMS layer can be produced [9]

A major disadvantage of conventional cell culture systems is that cell differentiation into functional cells requires extended culture times as well as an external signal detection system. Musah et al. mimicked the structure and function of the glomerular capillary wall by inducing pluripotent stem cell-derived podocytes to form human glomerular cells (Fig. 2.6b). This device could be applied for nephrotoxicity assessments, regenerative medicine, therapeutic development and kidney development and disease.
Recently, Sakolish et al. (2019) developed a microfluidic chip in human proximal tubules and golmeruli that

permitted renal epithelial cells to grow [55]. Schutgens et al (2019) designed stable tubule culture systems that permitted extended expansion and human kidney tissue analyses [56]. Finally, Nieskens et al (2019) created a strategy to generate human islet organoids from human induced pluripotent stem cells. The strategy was applicable to a wide variety of applications for stem cell-based organic engineering and regenerative medicine [57].

2.3.7. Multi organ-on-chips

Single OoC devices fail to fully reflect the complexity, functional changes and integrity of organ function. MOoC devices culture cells of different organs and tissues simultaneously which are connected by channels to achieve multi-organ integration, permitting the examination of interactions to establish a system. These systems can be separated into static, semi-static and flexible devices [58]. Static MOoC systems are integrated into single connected devices. In semi-static systems, the organs are joined via fluidic networks with transwell-based tissue inserts. In the flexible system, individual organ-specific platforms are interconnected using flexible micro channels. Although the MOoC concept is still in its infancy, major breakthroughs have been made including the design of two-organs, three-organs, four-organs and ten organs on a chip systems. Zhao et al. (2019) created an overview listing several succesfull MOoC models along with the fabrication approach and the outcome of the research conducted with the MOoC device [13].

Table 2.3: Overview of the biomedical applications of MOoC platforms [13]

Application	Multi-organ/tissue system	Fabrication approach	Outcome	Refs
Disease modeling	Liver, heart and vascular system	Interconnected iPSCs-derived cardiomyocytes and hepatocytes by 3D-printed rigid filament networks of a carbohydrate glass with endothelial cells and perfused the networks with blood flow.	Helpful for predictions of physiological responses in the diseased microenvironment.	[59]
Drug screening	Liver, heart, lung and kidney	Adopted allometric scaling for coupled non-linear OoC/MOoC systems to create micro-organs maintained by a universal media.	Helpful for the screening of new drugs for efficacy and potential side-effects	[60]
	Liver, marrow, megakaryoblast, and cancerous tissues	Integrated a μCCA device into a silicon chip, on which four functional tissues were cultured in corresponding chambers connected by tubing, with recirculating flow being provided by a peristaltic pump.	Helpful to predict the selectivity of chemotherapeutic/modulator mixtures for killing or reducing the growth of multidrug resistance tumor cells *in vivo*.	[61]
	Liver, intestine, and breast carcinoma cells	Containing microtissues of liver, gut and the breast carcinoma cells cultured in the target components consisting of a slide and PDMS layers, having microchannels.	Helpful for the evaluation of properties of orally ingested foods, drugs, and chemicals.	[62]
Cancer metastasis	Marrow, mesenchymal stem cells, and breast cancer cells	Bonded a PDMS layer to a cover glass to create microfluidic channels with plasma treatment, and provided multiple cell-culture gel regions connected to the central media channel.	Helpful to mimic the dissemination of breast cancer cells into bone.	[63]
	Brain, bone, liver and lung carcinoma cells	Combined three PDMS sheets and two thin PDMS microporous membranes to create parallel microchannels connecting an upstream micro-lung and downstream micro-organs.	helpful for observing lung cancer cell behaviors in a physiologically relevant context.	[64]
	Gut, liver, and colon carcinoma tissues	Comprising two independent cell-culture chambers connected by a circulating fluid flow. Fabricated with a hyaluronic acid-based hydrogel system in which the metastatic colon carcinoma tumor foci were created.	Helpful for studying the process of the migration of colon carcinoma cells.	[65]
Biomarker detection	Heart, liver, and lung	Comprised lung tissues based on the PDMS model and bioprinted spherical liver- and heart organoids, connected via a central fluid channel with fluid flow driven by a pump.	Helpful to utilize enzyme-linked immunosorbent assays to determine the effect of bleomycin to quantify the levels of interleukin-8 and interleukin-1β.	[66]
	Liver, intestine, cancer and connective cells	Contained two culture chambers interconnected in each culture unit via microchannels with a medium driven by a pneumatic pressure-control system.	Helpful for liquid chromatography coupled with a mass spectrometry system, to measure the concentrations of capecitabine in the medium.	[67]
Drug testing/ toxicology	Liver, tumor and marrow	Combined a three-compartment microscale cell culture analog (μCCA) device exposed to a pumpless gravity-induced flow with a mathematical pharmacokinetic and pharmacodynamic model.	Promoted the prediction and analysis of the effects of 5-fluorouracil.	[68]
	Liver, intestine, skin and kidney	Integrated two peristaltic on-chip micropumps and microfluidic channels connecting four tissue culture chambers for two microfluidic circuits into the device.	Helpful for repeated dose toxicity testing of drug candidates and further *in vitro* metabolism, elimination, absorption and distribution observation.	[69]
	Liver, colorectal tissues	Cultured spherical microtissues in parallel, connected by a microfluidic-channel network, with liquid flow controlled through a hanging-drop device.	Helpful for testing drug effects at different concentrations.	[11]
	Liver, nerve tissues	Connected two tissue compartments exposed by microfluidic channels and was maintained in a combined media circuit.	Showed the dose-dependent cytotoxicity result of a neurotoxic compound.	[70]
	Liver, heart	Contained human iPSCs-derived liver and heart tissues, which were exposed to serum-free medium flow using a pumpless system.	Helpful for the prediction of the cardiotoxicity transformation of drugs through hepatic metabolism.	[71]

Liver, skin tissues	Used a single PDMS layer integrating the respectively arranged channels interconnecting the tissue counterparts, peristaltic on-chip micropumps, openings for culture compartments and media reservoirs.	Tested the liver toxicity of troglitazone at different molecular levels.	[12]
Lung, gut, skin, vascular, liver, and kidney	Using physiologically-based pharmacokinetics with pharmacodynamic models for estimating ADME parameters, was made of PDMS and microfluidic channels for connecting different organ compartments.	This model was helpful for pharmacodynamic modeling and drug development in different stages.	[72]

2.4. Relevance of gut-brain axis

The relationship between the gut and the brain has been of interest to researchers ever since orally administered medicine were meant to reach the brain. Numerous studies exist in which the research focuses on the fraction of medicine molecules that reach the brain after being absorbed by the gut. In 2014, the field got a new impulse when researchers found a new connection between these organs [73].
It has become apparent that there is a correlation between the composition of the gut microbiome and behavioral conditions [73]. Bacterial waste products can influence the brain. An example is the neurotransmitter γ-aminobutryic acid (GABA) which can be produced by at least two types of intestinal bacterium [74]. In one study, it was found that mice born by caesarean section, which hosted different microbes from mice born vaginally, were significantly more anxious and had symptoms of depression. The fact that the animals were unable to puck up their mother's vaginal microbes during birth, which are the first bacteria that they would normally encounter, had caused lifelong changes in mental health [75].
Similarly, in another study in 2013, it was found that a mouse model with features of autism had much lower levels of a common gut bacterium called Bacteroides fragilis than did normal mice [76]. The mice were stressed, antisocial and had gastrointestinal symptoms often seen in autism. Feeding Bacteroides fragilis reversed the symptoms. Mice with these symptoms also had higher levels of bacterial metabolite called 4-ethylphenylsulphate (4EPS) in their blood. When this chemical was injected into normal mice, they showed the same behavioral problems.
The mechanisms for these effects are still unclear and researchers are skeptical that the findings will translate into treatments for humans. OoCs technology could potentially prove itself usefull in this field by connecting gut- and BBB OoC models.
The following sections will focus on current existing gut- and BBB OoC models. The final section mainly focuses on possible techniques to connect these two different models.

2.5. Blood-brain barrier

The BBB is a highly organized and dynamic structure that regulates the passage of molecules from the brain vasculature into the central nervous system (CNS) and functions as a defense system that protects the brain from infections and toxins. The barrier results from a combination of tight and adherens junctions between cerebral endothelial cells (CECs). These junctions dramatically reduce the rate of transcytosis relative to vessels outside of the CNS. Critical support for the BBB is provided by pericytes (PCs) and astrocytes, located on the abluminal side of the endothelium. Both the CECs and the PCs are closed by, and contribute to, the local basement membrane which forms a distinct perivascular extracellular matrix. Axonal projections from neurons onto arteriolar muscle contain neurotransmitters and peptides and regulate cerebral blood. Microglia are the immunocompetent cells of the brain, acting as the first and main immune defence of the CNS. The movement of solutes across the BBB is either passive, driven by a concentration gradient or may be facilitated by passive or active transporters in the endothelial cell membranes. A schematic overview of the structure is shown in Figure 2.7. Dysfunction of the BBB is associated with several CNS diseases such as multiple sclerosis, Alzheimer's disease and neurological tumors including glioblastoma multiforme [77].
Currently, *in vivo* models (mostly mouse models) are the standard for studies on the BBB and the related CNS diseases. While these models have significantly contributed to new discoveries of BBB mechanics, they are limited by physiological differences between humans and rodents. This is why several BBB-on-a-chip models have been developed.

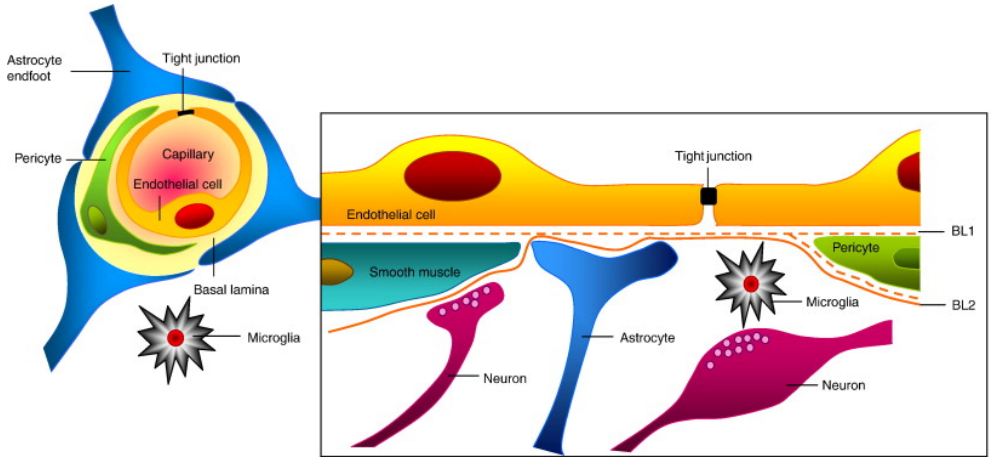

Figure 2.7: Close up of the BBB showing the most prominent cell types it consists off. [77].

2.5.1. Current state of BBB OoC models

Over the past two decades, different approaches have been used to mimic the BBB *in vitro*. The exact development and working of these devices greatly vary. This diversity will be discussed according to the four key components of OoC models previously mentioned in Sections 2.2.1 to 2.2.4 from the first Chapter. An overview of recently created BBB OoC models including the the four key components is shown in Table 2.4.

Microfluidics

In order for an *in vitro* BBB model to closely resemble the *in vivo* environment, it should account for the following features of the BBB: (i) a 3D vessel-like structure of cerebrovascular endothelial cells (ECs); (ii) cell-cell interactions; (iii) flow-induced shear stress on ECs; (iv) a thin molecule -permeable basal membrane (BM). To date, various BBB models have been created to meet these requirements. Oddo el al (2019) defined four basic microfluidic device designs used for BBB OoC models: the sandwich design, parallel design, 3D tubular structure design and vasculogenesis design [78].

The sandwich design comprises of an upper and lower PDMS channel that is separated by a porous membrane (Fig. 2.8a). Usually ECs are seeded in the upper channel while astrocytes, pericytes and other brain cells are cultured in the lower channel. One critical drawback of this design is that capturing high-resolution images and monitoring of biomolecule transport and cell growth in real-time is almost impossible. Also, cell-cell contacts between brain cells and ECs are inhibited because of the separation distance [79].

In the parallel design, two aligned channels are separated horizontally by an array of PDMS microchannels (Fig. 2.8b). The PDMS-based microchannel 'membrane' significantly simplifies the assembly of the BBB devices because no further steps are necessary to chemically modify the membranes or to bind the individual components together. In addition, the planar parallel design allows better cell-cell interactions and enhances imaging quality [80].

Another popular BBB design is the 3D tubular structure design (Fig. 2.8c). This design aims at constructing cylindrical microchannels, which benefit from a constant shear stress along the inner walls, contrary to microfluidic designs with a rectangular shape [14].

The majority of BBB designs focus on creating microvessels conforming to a predetermined scaffold such as microneedles or microfluidic channels. An interesting approach is the vasculogenesis design which has been exploited to reconstruct microvessels *de novo* (Fig. 2.8d). It allows ECs to sprout into ECM gels to form a vascular network *de novo*. This results in natural microvessels but with less structural reproducibility [81].

Living tissues

As mentioned in Section 2.2, the BBB consists of several components with the most important being endothelial cells, pericytes and astrocytes. From these components, ECs are the main players forming the physical barrier between the brain and blood which is why these cells will be discussed in this section for the sake of conciseness. Oddo et al. (2019) describe three types of ECs: primary ECs, immortalized EC lines and stem-cell derived ECs [78].

Primary ECs are obtained from the fore brain cortex *ex vivo* by surgical removal, followed by various purification steps. To this date, brain microvascular ECs from humans, rats, bovines and procines have been

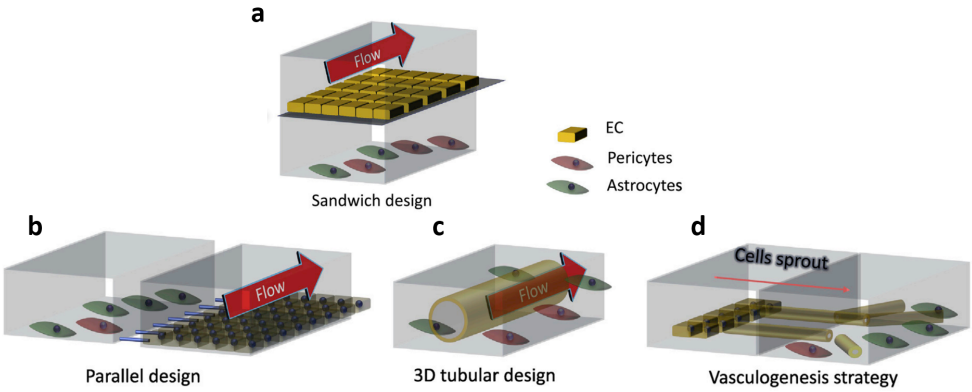

Figure 2.8: Visual representation of different microfluidic designs in BBB devices [78].

successfully isolated and cultured *in vitro*. The most favorable properties of these ECs include less genotopic mutation/loss and better resemblance of the BBB phenotype *in vivo*. However, drawbacks of using primary cells include inevitable contaminations from other cells during isolation, limited number of cells obtained, labor-intensive cell extraction and loss of cell phenotype after several passages *in vitro* [82].
Immortalized cell lines are a population of cells which would normally not proliferate indefinitely, but due to mutation have evaded normal cellular senescence and instead can keep undergoing division [83]. The obvious advantage of immortalized cell lines is that they offer cell purity and robustness over long periods of passages. It is currently highly controversial which immortalized cell line is the better model for BBB *in vitro* studies. Whilst human brain microvascular endothelial cells (hCMEC/D3 and hBMECs) can exhibit high expression levels of a number of tight junction (TJ) proteins and form tight barrier under both static and fluid shear culture conditions, the most commonly used immortalized EC line are human umbilical vein endothelial cells (HUVECs). HUVECs are controversial for BBB model use because they form barriers *in vitro* that are leakier than other cell models [84]. Alternatively, miruine cell lines have also been reported for *in vitro* studies and have shown to express relatively high levels of TJ proteins [83].
Stem-cell derived ECs or human pluripotent stem cells (hPSCs) hold great potential to overcome the limitations of the other cell lines. hPSCs have a virtually unlimited self-renewal capability and can be differentiated into many different somatic cell types. Furthermore, the hPSCs respond positively to co-culture with astrocytes by forming tighter TJs and posses a molecular permeability that well mimics *in vivo* BBB characteristics [85]. This makes hPSCs an attractive candidate for usage in BBB *in vitro* models. However, hPSC protocols for differentiation are costly, complex and time consuming. Additionally, a small permutation can have catastrophic effect on their quality and robustness.

Stimulation or drug therapy
Generally, BBB models do not require any forms of stimulation other than the flow-induced shear stress on ECs. Regarding drug therapy, any types of drugs or molecules administered to the system are dependent on the aim of the research.

Sensing
In order to assess the quality of the *in vitro* BBB model, two main types of measurements are conducted: transepithelial electrical resistance (TEER) measurements and permeability measurements.
TEER is the measurement of electrical resistance across a cellular (mono)layer and is used to confirm the permeability and integrity of the cellular layer. This is especially important for blood vessels in the brain because these often have considerable tighter vascular beds than other peripheral organs. In order to measure TEER values, the first electrode is placed inside the 'blood' vessel and the second electrode on the 'brain' side. Although TEER measurements is the gold standard to quantify the quality of the created BBB, sometimes these measurements are not possible due to the design of the BBB models. Additionally, it remains a challenge to introduce electrodes into the emulated blood channel of ECM gel-based devices without breaking the endothelial layer [78].
A less invasive method for quantifying the tightness of the BBB is the small molecule permeability measurement, which measures the diffusivity of carefully chosen probes across the barrier. Generally, size and polarity

are the main physiochemical properties that influence the BBB permeability of molecules and on which probes are chosen [86]. It is important that the probes do not interfere with the physiological functions of the BBB. In previous experiments, fluorescently labeled dextran is commonly used as a probe in many BBB models. Using dextran is worrisome because of its different molecular weights causing false BBB integrity results. Therefore, other molecule dyes have been used such as sodium fluorescein and Cascade Blue to test BBB integrity [79].

Table 2.4: Selection of BBB OoC devices showing the design type, main cell types, induced shear stress, additional external stimuli, TEER and probes to test permeability [78].

Device design	Cell cultures	Shear stress (Pa)	External stimuli	TEER ($\Omega \cdot cm^2$)	Probes	Refs
PDMS sandwich	b.End3 (mouse)	1-2 x 10^{-3}	Histamine	250-300	Dextran	[87]
PDMS parallel	HUVECs (human)	0.028-0.8	H_2O_2	NA	Dextran	[88]
PDMS sandwich	hCMEC/D3 (human)	0.58	TNF-α	120	NA	[42]
PDMS sandwich	RBE4 (rat)	NA	TNF-α	NA	Dextran	[89]
PDMS parallel	RBE4 (rat)	3.8 x 10^{-4}	NA	NA	Dextran	[90]
PDMS parallel	RBE4 (rat)	3.8 x 10^{-4}	NA	250	Dextran	[80]
ECM gel-based tubular structure	RBE4 (rat)	NA	TNF-α and oxygen-glucose deprivation	NA	Dextran	[87]
ECM gel-based tubular structure	b.End3 (mouse)	NA	D-mannitol	NA	Dextran	[91]
PDMS sandwich	Primary hBMVEC (human)	2 x 10^{-3}	Cold shock and glutamate	350	Dextran	[43]
PDMS sandwich	b.End3 (mouse)	0.5	NA	NA	Dextran	[92]
PDMS sandwich	hCMEC/D3 or primary rat ECs	1.5 x 10^{-2}	NA	175	Dextran, albumin and sodium fluorescein	[93]
ECM gel-based tubular structure	hBMVEC (human)	NA	TNF-α	40-50	Dextran	[94]
ECM gel-based tubular structure	Primary BMEC (rat)	1 x 10^{-2}	NA	1298	Sodium fluorescein	[95]
PDMS sandwich	bEnd.3 (mouse)	1.5 x 10^{-2}	NA	1150	NA	[96]
PDMS sandwich	hiPS-derived BMEC (human)	1.4-25 x 10^{-3}	NA	4000	Dextran	[21]
ECM parallel	HUVEC or hCMEC	NA	NA	NA	Dextran	[84]
ECM gel-based tubular structure	hBMVEC/D3 (human)	0.07	TNF-α	1000-1200	Dextran	[97]
PDMS parallel	HUVEC (human)	1.9 x 10^{-4}	NA	NA	Dextran	[98]
ECM vasculogenesis	HUVEC (human)	NA	NA	NA	Dextran	[99]
Tubular structure	b.End3 (mouse)	NA	NA	75	Dextran	[100]
PDMS structure	Primary hBMVEC or astrocyte (human)	2 x 10^{-3}	TNF-α	NA	Cascade blue/BSA/anti-GluR2 Ab	[79]
ECM parallel	TY10 (human)	0.12	NA		Dextran	[101]
PDMS sandwich	Primary BMVEC (mouse)	0.1-3	Histamine	3500	Dextran	[102]
PDMS sandwich	b.End3 (mouse)	0.1-0.6	NA	172	Dextran	[103]

2.6. Gut

The word gut refers to the small and large intestines. This part of the digestive system is often the first barrier for orally administered medicine to cross before they can reach their intended location. Its main purpose is to digest food, but it also produces various substances that carry messages to other parts of the body and plays an important role in fighting germs and regulating the body's water balance [104].

The epithelium of the intestine consists of several components, the most important being enterocytes, goblet cells and crypts of Lieberkuhn. The enterocytes are tall columnar cells which have an absorptive function. This absorptive function is enhanced by an increase in surface area created by villi, the structure that enterocytes form, and microvilli which are located on the luminal side of the enterocytes. These cells also contain the essential enzymes necessary for digestion. The goblet cells make up a part of exocrine glands which secrete mucin, a family of glycosylated proteins with a main function of protecting the intestine's inner surface. The crypts of Lieberkuhn are glands in the epithelial lining. They contain numerous cells such as enteroendocrine cells to synthesize and secrete hormones, as well as stem cells to produce new cells to replenish the cells lost to abrasion. More detail of the small intestine is shown in Figure 2.9. The intestine propels food by radial symmetrical contraction and relaxation of muscles called peristalsis [105].

Analysis of gut microbiome interactions with human intestinal cells has been limited to genetic or meta genomics analysis, because co-cultures of microbes with living epithelium in conventional models only last for about 1 day. Therefore, great efforts have been made to develop *in vitro* and *ex vivo* models of human intestine that permit analysis of intestinal functioning [106].

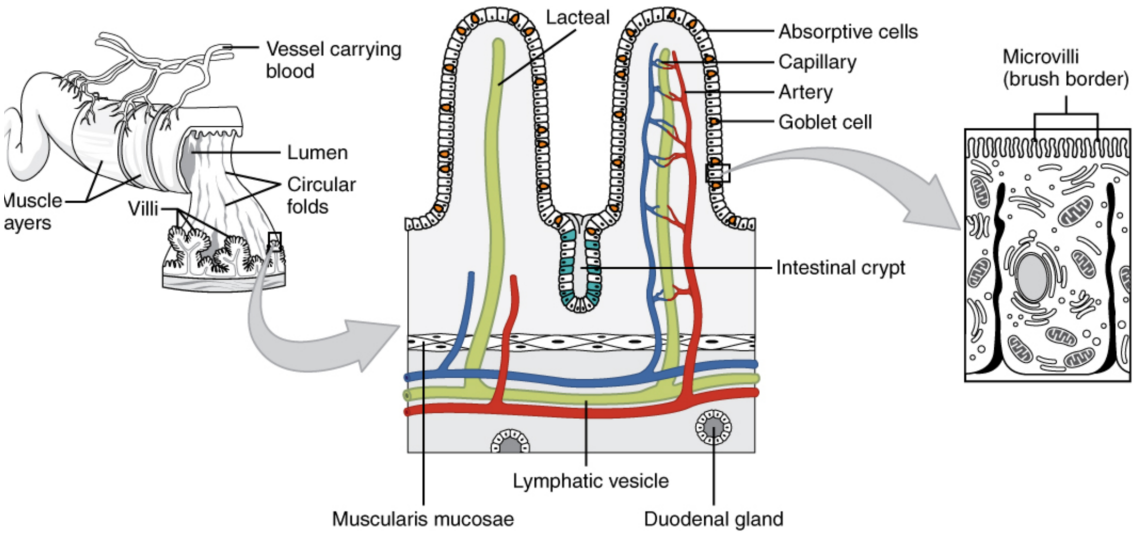

Figure 2.9: Schematic overivew of the small intestine. The absorptive surface of the small intestine is enlarged by the presence of circular folds, villi and microvilli [104].

2.6.1. Current state of gut OoC models

As is the case with BBB OoC models, also the gut OoC systems have experienced numerous developments and recent progress will again be discussed on the basis of the four key components mentioned in sections 2.2.1 to 2.2.4 from the first chapter.

Microfluidics

Most of the OoC gut models involve two microchannels that are separated by a flexible and porous membrane. This is the most common arrangement because it is used to simulate the barrier between the draining vasculture and the intestinal lumen. The dynamic microenvironment found *in vivo* is simulated by media pumped through the channels using pressure, syringe or peristaltic pumps. Generally, one of the channels represents a blood vessel and is lined with vascular endothelial cells, the other channel is lined with gut epithelial cells and represents the lumen of the gut [107]. The membrane in between these two channels can be made of an array of different materials and a variety of pore sizes, but its main function remains to allow the transport of soluble molecules between the simulated intestine and blood vessel. An example of a standard gut OoC model is shown in Figure 2.10. It is noteworthy that although most gut OoC models use membranes, Trietsch et. al (2019) created a membrane-free gut OoC model to improve the similarity to native tissue. Instead of a membrane, only a extracellular matrix gel as a barrier was used between the two channels [108].

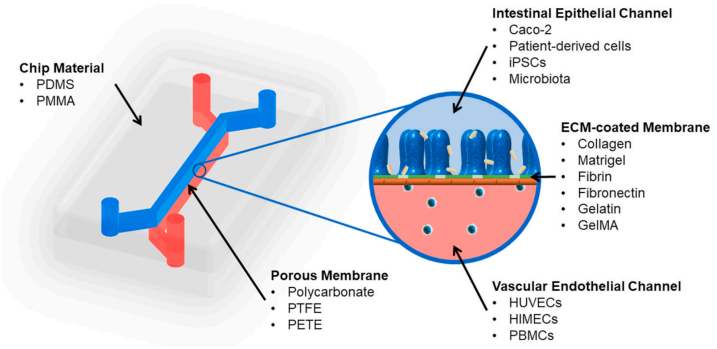

Figure 2.10: General overview of the structure and materials of a gut OoC model. [107]

Living tissues
The main differentiating factor of cell types for usage in gut OoC models is the source. Four sources can be categorized when it comes to gut OoC models: vasculature endothelial cells, immortalized intestinal cells, primary cells and stem cells.
As the name implies, vasculature endothelial cells are used to model the vasculature found in the intestines. Commonly used cell lines include HUVECs and HIMECs [109].
Many studies incorporate immortalized Caco-2 cells as intestinal cells. These cells are derived from human colon carcinoma and have been the standard for studying the human intestines [110]. Although Caco-2 cells are easily accessible, robust and can form crypt and villi structures within five days, they are also severely limited by their inability to produce a mucosal layer [111]. This greatly influcences the physiological microenvironment because a mucus layer increases solubility of compounds at the surface of cells which in turn impacts the permeability of molecules and drugs [110].
An alternative source are the primary cells. These cells have greater physiological relevance than immortalized cells becasue of the lack of genetic modifications. Disadvantages of these cells are the fact that they require exogenous growth factors, are less accessible and tend to be less robust [111].
The most recent development regarding living cell tissues in gut OoC models are the use of stem cells. Although reseach with this cell source is limited, stem cells are believed to have the potential to revolutionize gut OoC systems by differentiation into cellular subtypes of the intestine. The most commonly used stemcells include pluripotent embryonic stem cells (ESCs), induced pluripotent stem cells (iPSCs) and multipotent mesenchymal stem cells (MSCs) [112].

Stimulation or drug therapy
The presence of fluid flow to induce biomimetic shear stress has been the most important stimili in gut OoC models to create mature tissue *in vitro*. It has been shown that mucin-2 and actin expression was upregulated under flow compared to transwell models [113]. Fluid flow also reduces the number of *E. coli* in the system and has the ability to induce Caco-2 cell morphogenesis, polarization and differentiation into complex villi [111]. A variation of this stimulus that appears to induce villous structures is peristalsis-like strain on cells. In addition to villous structures, cell that were subject to peristalsis-like strain also showed expression of tight junctions, production of mucous and presentation of a brush layer.
Such mechanical stimuli also impact resident microorganisms. In recent studies, it was observed that the inversion of certain bacteria that can cause intestinal infections increased in the presence of simulated intestinal peristalsis. It was concluded that these bacteria leverage the intestinal microarchitecture and mechanical forces to invade the tissue. This means that models with mechanical stimuli are more useful to study bacteria induced infections than static models [114].

Sensing
Analytical methods are used to characterize the cells and tissues within most gut OoC models and to quantify the function of the gut cells. It is possible to use optical analytical methods, including light microscopy, fluorescence microscopy and confocal microscopy, due to the optically transparent chip materials that the models consist of such as glass and PDMS [115].
Another way of characterizing tissues and cells can be done with the effluent from the device. The used liquid from both the vascular and intestinal channels can be assayed for dissolved pH, metabolites, drug concentration, signalling molecules and O_2 [116].
The final analytical component found in gut OoC models are TEER sensor. As mentioned before, TEER is a non-invasive method for characterizing the barrier function of formed layers of cells inside the gut OoC model. In many OoC models that have cellular barriers, TEER measurements can be performed with electrodes placed on opposite sides of the barrier. It is important to note that TEER values can be influenced by many factors such as temperature, medium formulation and passage number of cells. This can make it hard to compare different OoC models on cell barrier function [117].

2.7. Coupling techniques
As mentioned in Section 1.3.7, coupling techniques used to connect different OoC models can be divided into three categories: static, semi-static and flexible. Currently, only very few gut-brain OoC models exist.The only group that explicitly tried to connect a gut and a BBB model was Raimondi et al. (2019) using a static

connection [118]. This group investigated the existence of the Microbiota-Gut-Brain axis hypothesis for Alzheimer's disease and Parkinson's disease, which states that intestinal microbiota can have a pathogenic role in neurodegeneration. Their system, called the MINERVA platform, relies on five miniaturized, sensitized, optically accessible OoC devices. The OoC included gut microbia, gut epithelium, the immune system, the BBB and the brain. Each device is hydraulically connected to the next with a microfluidic pipeline. Medium flows through this pipeline under positive pressure. In the microbiota, gut epithelium and immunse system models cells were cultured in standard conditions while the brain device contained cultured neurons, microglia and astrocytes embedded in a hydrogel matrix. A schematic overview of the complete system set-up is shown in Figure 2.11 [118].

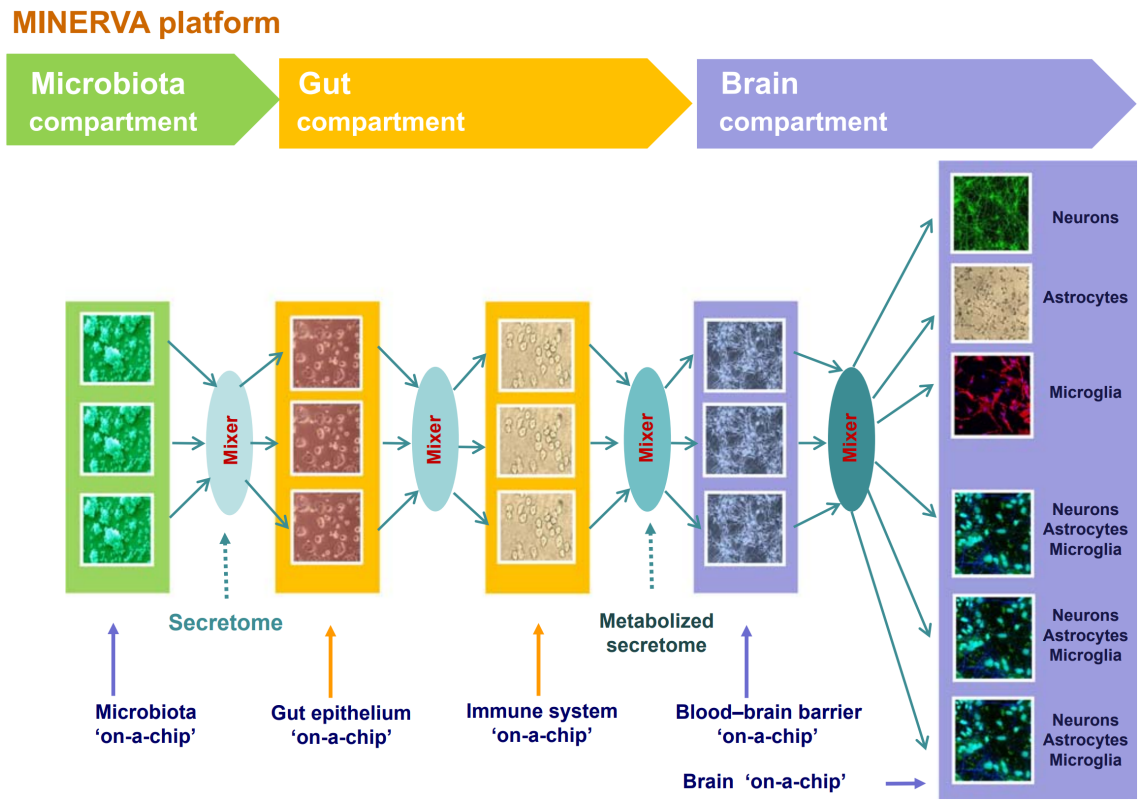

Figure 2.11: Schematic overview of the MINERVA platform. The microbiota compartment features one microfluidic device hosting microbial cultures. The secretome will flow to the next compartment, such as for the passage of microbiota-secreted neurotoxins. The gut compartment hosts two OoC devices modeling the gut epithelium and the strictly related immune system cells. The brain compartment recapitulates the BBB and the main brain cells relevant for neurodegeneration in 3D condition because of the presence of an hydrogel matrix in which the cells are embedded [118].

Although no other direct gut-brain-axis OoC systems are described in literature, besides the MINERVA system, other organs have been connected to either a gut or a BBB OoC model. One relevant example is the gut-liver connection created by Tsamandouras et al. (2017) [119]. The aim of their model was to investigate the pharmacokinetics (PK) of diclofenac and hydrocortoisone. The model incorporates distinct compartments to accommodate a transwell-style gut system, a 3D-perfused liver system and a mixing chamber that aims to represent the systemic circulation compartment. These compartments are connected with microfluidic channels which in turn are connected to peristaltic micropumps. Flow rate can be dynamically controlled, allowing variations in pump rate and direction. The organ physiology and flow partition was mirrored as close as possible by connecting the gut and liver systems in series and the total ouput from the mixing chamber was partitioned as 75% and 25% respectively with a flow of 15 mL/day. The liver system and the basolateral side of the gut system received the same medium (500 mL Williams E medium, 20 mL Gibco Cocktail B, 80 nM HC and 1% penicillin/streptomycin) and the apical side of the gut system was provided with an apical medium (phenol red-free DMEM with 1x ITS, 1x NEAA, 1x GlutaMax and 1% penicillin/streptomycin).
As for the living cell tissues, the liver system consisted of human primary cryopreserved hepatocytes and Kupffer cells at a 10:1 ratio. The gut system consisted of Caco2-BBe epithelial cells and mucin-producing

goblet cells at a 9:1 ratio. An immune component was added consisting of primary monocyte-derived dendritic cells at a 10:1 ratio.
Aside from the shear stress induced by the fluid flow no other external stimuli were added to the system.
In order to assess cell culture health and function several associated metrics were analyzed including albumin production by the liver cells, TEER and mucin production in by the gut cells. [119]

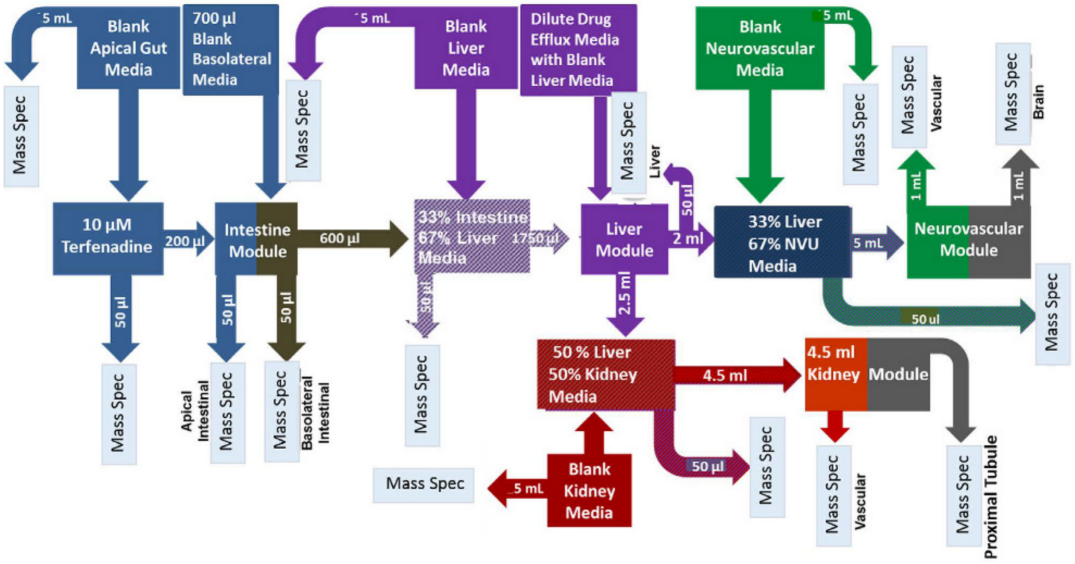

Figure 2.12: Schematic overview of the work flow for functional coupling experiments involving liver-, kidney, intestine- and neurovascular models [120].

Another relevant study regarding the coupling of different OoC models was published by Vernetti et al. (2017) [120]. This group used functional coupling to link four human OoC models: human intestine, liver, kidney and BBB. This was done by transferring the medium from one OoC model to the next in a physiological sequence, wherein each OoC model functionally transforms the media composition based upon the specific metabolic activity of that system. The main take away from this research regarding the microfluidics is that every system uses its own influx medium, which is mixed with the efflux from the preceding model, a similar method to the MINERVA system discussed previously. Figure 2.12 shows the complexity of the functional coupling and the volumes that were used of efflux and general medium. Other microfluidic variables that were taken into account include media components, perfusion speed and perfusion times.
Mature enterocytes and goblet cells were used for the gut system, while human iPSC-derived neurons, pericytes and astrocytes were cultured in the BBB model.
Again, no other stimuli were induced to the cells by the OoC models other than the shear stress of the fluid flow.
The metrics associated with cell culture health and function included TEER, dextran diffusivity and the transport of vitamin D, terfenadine and trimethylamine. [120]

2.7.1. Challenges

Linking multiple OoC models poses many challenges. Besides using correct medium and flow speeds, various other problems need to be assessed as well. Vernetti et al. (2017) listed the key biological and key technical challenges for coupling individual OoC models, which are listed in Table 2.5 [120]. For linking gut-on-chip devices with BBB OoC devices specifically, the biggest additional challenge will be to construct a solution for the missing metabolic processes that take place in the liver.

Table 2.5: Key challenges for coupling multiple OoC models [120].

Topic	Challenges
Biological	Implementing a universal medium. Proper scaling of OoC models to reproduce maximal functions. Further developing of gut in OoC device. Implementing a combination of real-time fluorescent labeled biosensors in multiple organs. Establishing a source of renewable adult iPSC for all/most cell types to provide single donor disease phenotype cells and to overcome current need to mix primary cells or established cell lines from genetically diverse sources. Vascularization of all OoC models
Technical	Minimizing drug/biomolecule binding to PDMS, tubing, membranes and devices made from various materials. Minimizing connection volume and bubbles while maintaining sterile conditions. Creating oxygenation conditions for each organ, including different oxygenation on apical and basolateral surface of the gut. Creating optimal flow rate in each OoC model. Establishing PK analytics and modeling from data captured in database. Integrating dynamic, chemical and electrical cues, including contributions of missing organ system.

2.8. The need for sensors in OoC systems

With the increasing complexity of OoC systems, the necessity to integrate relevant assessment methods increases as well. Advanced monitoring tools and read-out of *in vitro* systems are required to be able to provide temporally and spatially resolved information about cell microenvironment and physiology as well as pharmacodynamics drug responses [121]. To achieve this, several engineering approaches have been used to develop chemical, biological and physical sensors that can be integrated to OoC systems. Such sensors have shown to provide reproducible results with multiplexing, data transmission and on-line monitoring capability by analyzing low volume samples [122]. For the sake of completeness, Table 2.6 shows an overview of all sensors that have been used in OoC systems to this date.

Table 2.6: Overview of current metrics analysed by sensors in OoC to date [33].

Category	Metrics
Metabolism products	H_2O_2, glucose, lactate, cytokines and other secretoms such as albumin, GTS-α, transferrin, reatine kinase-MB, troponins
Phyhiscal system parameters	pH, strain, oxygen, temperature, glucose and lactate
Cell fate	Oxygen consumption, pH, membrane potentials, flow speed, ion concentrations and release of various metabolic compounds and proteins
Cell viability	Cell impedance
Single cell analysis	Cell impedance, glucose
Cell differentiation analysis	Cell impedance, cell mobility, membrane capacitance, ATP, ADP, UTP, oxygen consumption, pH, cell metabolites, TEER.

The need for sensors in OoC systems seems obvious as it is the only way of validating whether or not the systems emulates an *in vivo* environment, but there are actually three different types of information that sensors can provide about an OoC system. These three different types of information can be detected by sensors that are either integrated in the design of the device or external (e.g., optical sensors).
The first and most prominent function of sensors is to provide information about the culture environment. The biggest determinant for the formation of functional tissue is the cell culture environment. Parameters that are associated with this environment include temperature, pH, humidity, oxygen levels, nutrient content and many more. The exposure of the cells to these parameters together with interactions with secreted

metabolites from neighboring cells and mechanical interactions from cell-cell and cell-ECM contact are essential to the quality of the formed cell culture. The integration of sensors in OoC systems can enable a reproducible and controllable culture environment [123] .
A second factor that sensors can monitor is the cell behavior, which would be a result of the environment that they are in and the stimuli that they receive. To this date, sensors have been developed to monitor cellular adhesion, death, contraction properties, electrical properties, detachment, sepsis and response to osmotic stress.
The third domain in which sensor are applied is to monitor the stimulations applied to the system and the cell culture. A distinction can be made between sensors that monitor mechanical stimulations such as deformations induced by stretching, sensors that monitor chemical gradients such as hormones and cytokines, and sensors that monitor electrical stimulations. These stimulations all contribute to the cell environment and the cell behavior, therefore being essential for creating a controlled and realistic micro environment [33].

2.9. Suitable sensors for a gut-BBB OoC model

In order to develop a gut-BBB OoC model that can monitor the culture environment, cell behavior and input stimuli in real-time many possible sensors could be chosen as candidates to do so. However, in this thesis project the sensors developed by the Wyss Institute will be utilized to achieve this goal. In recent years, the Wyss Institute has developed integrated TEER sensors and has used optical pH and oxygen sensors is several different OoC devices. In the next sections will discuss each sensor's functionality and how it could be used in a gut-BBB OoC model.

2.9.1. TEER

Because the electrical impedance across an endothelium or epithelium is directly related to the formation of TJs between neighboring cells, measurement of TEER is a non-invasive, conventional and quick metric to evaluate the level of integrity and differentiation of *in vitro* epithelial monolayers in conventional static cultures [124]. In OoCs however, the use of TEER measurements of cell cultures remains technically challenging because of the close, micrometer-sized and microfluidic environment of the cells that makes it difficult to access.

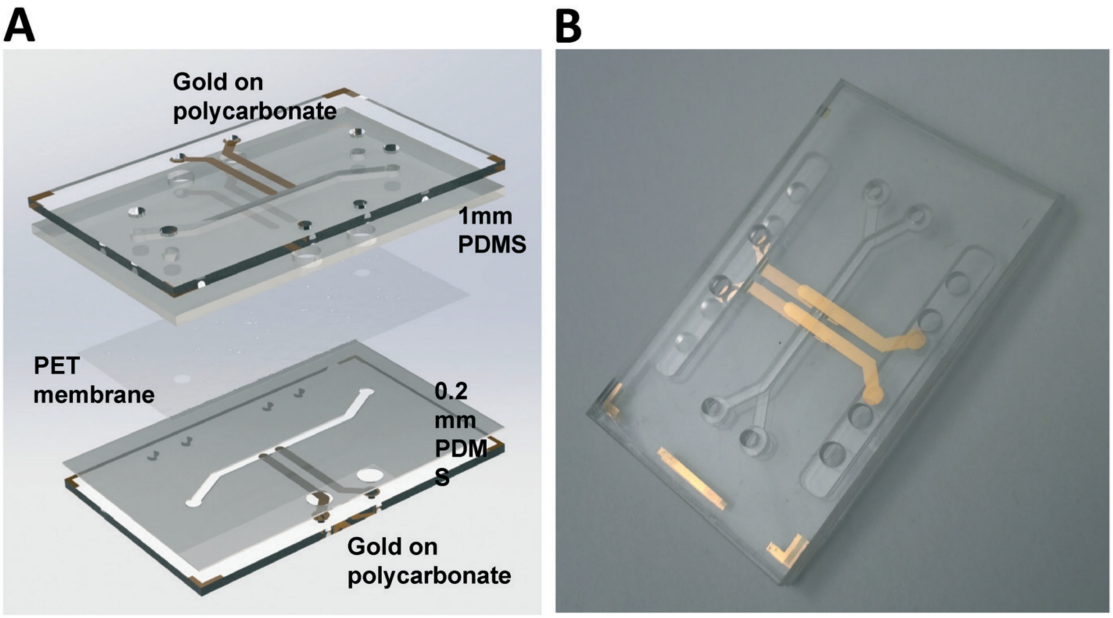

Figure 2.13: TEER sensor system develop by the Wyss Institute. (A) CAD model of the chip with TEER sensor. Gold electrodes are patterned onto polycarbonate substrates and laser cut PDMS layers and a PET membrane are assembled by silane-based surface modification to bond together. (B) Assembled chip with TEER sensor with dimensions 25 x 40 mm [125].

To achieve *in situ* TEER measurements on-chip, many different attempts have made by direct insertion of metal wires into pre-molded locations below and above membrane-supported cell monolayers, repeated insertion of manipulated electrodes normally used in Transwell experiments, construction of cell culture chambers around large electrodes, or by integrating glass or polymeric substrates that contain electrodes formed using conventional metal patterning techniques into microfluidic culture devices [35, 126–128]. The problem with these techniques is the large measurement variability, low sensitivity and the fact that they can be affected by non uniform cell cultures. To address this issue, Henry et. al (2017) developed a 2-channel layer-by-layer OoC design with integrated electrodes that enables real-time measurement of TEER values across the cells (Fig. 2.13) [121] .
In this TEER sensor, a small current of 10 μA of varying frequency is applied between two semi-transparent electrodes which are located on each side of the cell culture and the drop in potential between the second set of electrodes is measured (Fig. 2.14). The OoC device in which the TEER sensors was integrated was assembled following a layer-by-layer approach, as can be seen in Figure 2.13A, and has a microfluidic sandwich design. Standard Lonza's BEGM growth medium was used with a perfusion speed of 60 μL h^{-1}. The device was tested with human intestinal epithelium (hAECs) for 12 days. In a later study, conducted with the same OoC device, tests were done with human intestinal epithelial cells (Caco2) [126]. Both studies showed stable results compared to the mathematical models in the range of 0.5 Hz to 100 Hz, although lower frequencies resulted in instabilities. By measuring the electrical impedance and capacitance, these TEER sensors may open up more applications including measurement of action potentials of electrically active cells or short circuit current, something that could be specifically relevant for BBB OoC models.

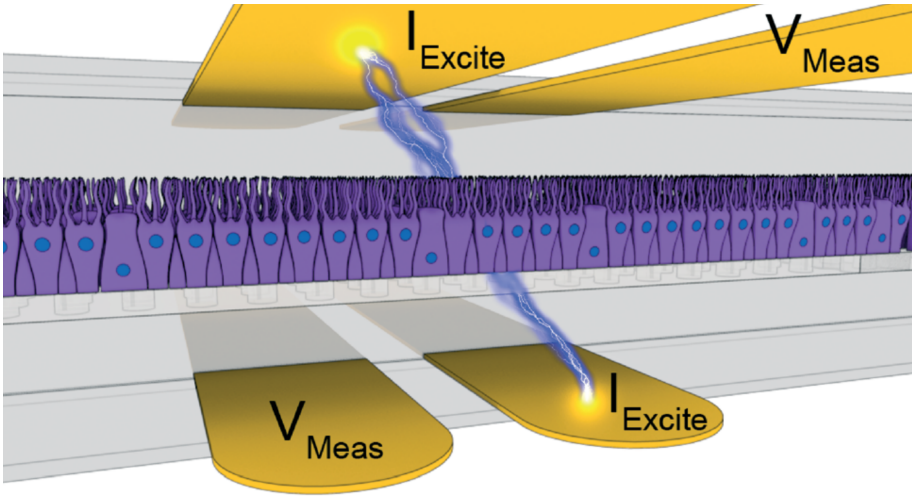

Figure 2.14: Schematic cross section of TEER model. (A) CAD model of the chip with TEER sensor. Gold electrodes are patterned onto polycarbonate substrates and laser cut PDMS layers and a PET membrane are assembled by silane-based surface modification to bond together. (B) Assembled chip with TEER sensor with dimensions 25 x 40 mm [125].

2.9.2. Oxygen

As mentioned in Section 3.1, oxygen concentration is a very significant regulatory parameter for cell culture and OoC devices. By measuring changes in oxygen concentration, information can be extracted about cellular activity, cell differentiation, cell viability and response to external stimuli [129]. Especially in gut OoC devices, oxygen concentration is a specifically important parameter. The commensal microbiome in the lumen of the human intestine resides under anaerobic conditions. This results in a steep oxygen gradient along the radial axis of the intestine [129]. To this date two kinds of oxygen sensor have been implemented in OoC devices: electrochemical oxygen sensors and optical oxygen sensors. The electrochemical sensors are based on the reduction of molecular oxygen at an electrode made of a noble metal [123]. Different types of oxygen sensors are direct amperometric sensors which are in direct contact with cell culture medium and Clark-type sensors that are separated from the medium by a gas-permeable membrane. The advantage of the Clark oxygen sensor is the fact that it is independent of electrode reactions from interfering or electrode poisoning substances present in the cell culture medium. Optical oxygen sensors

are based on the principle of fluorescence quenching by oxygen. A pulsed light is directed onto a fluorescent oxygen-sensitive dye which causes it to fluoresce. The rate at which this fluorescence decays is translated to the amount of oxygen present [130]. The fluorescent dye can be embedded as a single sensor spot or as a membrane coating on the whole surface in order to detect spatial oxygen concentration changes.

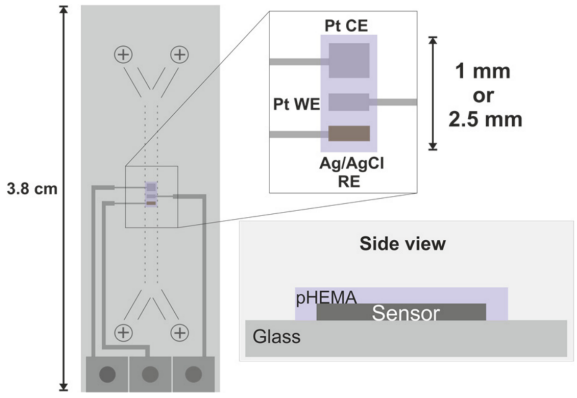

Figure 2.15: Top view of the clark oxygen sensor on glass with platinum working electrode (Pt WE), counter electrode (Pt CE) and Ag/AgCl reference electrode (Ag/AgCL RE). The purple area illustrates a layer of pHEMA [123]

The biggest advantage of optical sensors opposed to electrochemical oxygen sensors is the reusability, easy handling and sterilization [123]. Optical sensors are also less prone to drifts in interference caused by ions, proteins or drugs present in the cell medium. Also the performance of optical sensors is not influenced by the flow rates. The Wyss Institute, in collaboration with other research groups, has used both electrochemical and optical oxygen sensors which will be discussed next.
Bossink et al. (2018) created a miniaturized three-electrode Clark oxygen sensor. The sensor consists of three electrodes (Fig. 2.15), has a response time of 7.5s, is biocompatible and protected from biofouling. The group tested the sensor by integrating it in the same device from Figure 2.13. It showed to have a stable Ag/AgCl quasi reference electrode with a potential drop of 0.1 mV/hour, which is low compared to a 0.6 mV potential difference by a temperature change of 1°C. The sensor was covered by a thin protective biocompatible layer consisting of poly(hydroxyethyl methacrylate) (pHEMA) that is in direct contact with cells in the microfluidic channel. The biocompatibility was tested by exposing the pHEMA to a culture of Caco-2 cells for 48 hours. During this period no significant difference in cell death was observed. Although this sensor can be integrated into existing OoC devices with a 1 mm wide microfluidic channel, no articles have appeared since 2018 utilizing this clark type oxygen sensor [129] .

The optical oxygen sensor was developed two years earlier by Shaegh et al. (2016) [131] . This group developed an optical multi-analyte sensing module integrated with a microfluidic bioreactor for in-line monitoring of dissolved oxygen in the circulating culture medium [131]. The module consists of a microfluidic detection chamber integrated with optical components such as low-cost Si photodiodes and light emitting diodes (LEDs). To measure oxygen levels, an oxygen-sensitive dye was immobilized within a film inside the detection chip. A blue LED was used to excite the dye while the two Si photodiodes measured the degree of quenching in the luminescent intensity.
The dye used for the oxygen sensor was $[Ru(dpp_3)]^{2+}Cl_2$-tris(4,7-diphenyl-1,10-phenanthroline)ruthenium(II) chloride (Signma-Aldrich) because of its moderate brightness and high photostability. The dye was deposited at the bottom of the detection chamber. The fabrication of the detection chamber was finished with layers of optical filters and black PMMA (Fig. 2.16). The high-power blue LED was positioned directly above the fluid detection channel and two Si photodiodes were placed below the detection channel in anti parallel configuration.
The bioreactor, with a volume of 106 μl, was cultured with human dermal fibroblasts (HDFs). The volume of the culture medium inside the reservoir was 1.5 ml and the flow rate was 200 μl/h. The volumes of the sensing module and the tubing were 12.3 μl and 21 μl respectively.
The sensors were tested by monitoring oxygen levels in the system for 3 days. The sensors showed a constant oxygen concentration within the solution during the course of the experiments. Although high cell proliferation and viability were observed, no significant alterations in the oygen concentration tension within the medium was observed. This could be explained by the fact that the PDMS bioreactor, which is highly permeable to oxygen diffusion, was continuously supplied with oxygen. Overall, the sensing module showed a robust performance.
This optical system of oxygen detection in microfluidic systems provides a non-invasive method with minimal maintenance after installation. Once integrated with a control system, the system can indicate how the oxygenation process should be modulated [131] .

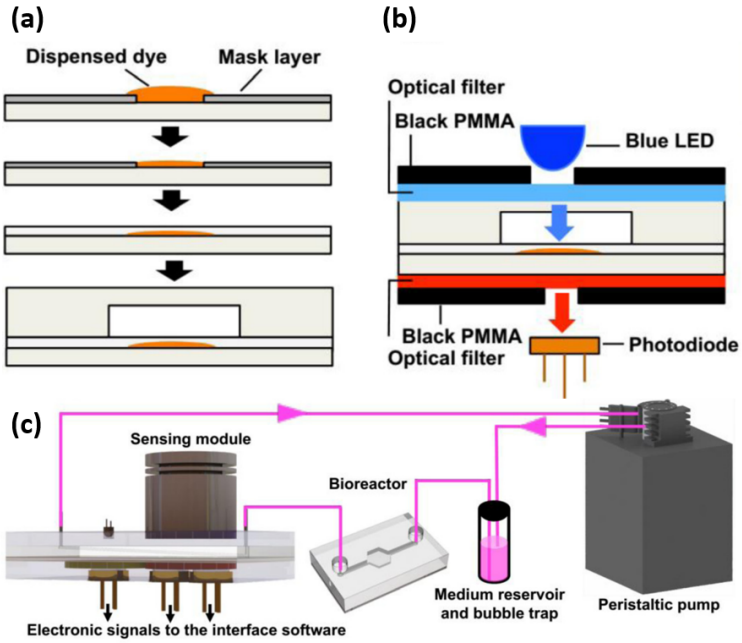

Figure 2.16: Schematic overview of the assembly of the detection chamber. (a) Deposition process of the oxygen-sensitive dye. (b) Arrangement of deposited dye in the detection chamber for signal read-out. (c) Complete setup [131].

2.9.3. pH

pH is a measure of the acidity or basicity of solutions, depicting the concentration of H+ ions. The pH scale is logarithmic and ranges from 0 - 14 on which 7 is neutral and lower values are considered acidic. The pH level is a key factor in the regulation of cellular microenvironments. It also plays a significant role in the process of cell growth and apoptosis, enzymatic activity, ion transport and endocytosis. Furthermore, intracellular pH is organelle-specific. For example, lysosomes and endosomes have acidic compartments with pH levels between 4.5 and 6.5, while mitochondria and cytosol have pH levels ranging between 6.8 and 7.4. Abnormal intracellular and extracellular pH levels are associated with cellular dysfunctions, leading to diseases such as cancer, neurodegenerative disorders and Alzheimer's disease [132–134]. In addition, cellular microenvironments have shown to become more acidic when present inside a tumor with pH values in the range of 6.2-6.9 [135]. Therefore, quantitative determination of changes in pH in cellular microenvironments is of great importance for cellular analysis and diagnosis.

Just as for oxygen sensors, a variety of optical and electrochemical techniques have been developed to measure pH in microfluidic and cellular environments. Also in the pH domain, optical sensors tend to be preferred over electrochemical sensors because of their reduced vulnerability to electrical interference introduced by cells in the cell culture solution and they are less prone to interference caused by ions, proteins or drugs in the cell culture medium.

To optically measure pH levels, the optical absorption by flowing culture medium containing phenol red is measured. Phenol red is a pH indicator whose color exhibits a gradual transition from yellow to red over the pH range of 6.8 to 8.2, a range well suited for cellular environments [136].

The same group that developed the optical oxygen sensor also developed an optical pH sensor that can be applied in OoC systems.

The optical pH sensor developed by Shaegh et. al (2016) measured optical absorption by flowing culture medium containing phenol red with fixed electro-optics [122]. These electro-optics consisted of a broadband LED used as an excitation source and a Si photodiode to detect the amount of light absorbed while passing through the media. The characterization of the amount of light absorbed in a phenol red solution at different pH values, solutions in pH of 6,7 and 8 were tested by using a microvolume UV-visible spectrophotometer. Results of this characterization is shown in Figure 2.17.

To test the setup, HDFs were again seeded in the bioreactor that were subject to a continuous perfusion of culture medium at a flow rate of 200 μl/min for 3 days. The pH level of the culture medium steadily decreased during the experiment, which can be associated with cellular activities. Over time, several cellular

metabolites accumulated inside the setup which shifted the pH level towards acidic values.
Although the pH sensor is deemed functional and reliable, it is noteworthy to mention that there are a few parameters that can affect the sensitivity of the pH measurements. These parameters include the concentration of the dissolved phenol red in the culture medium, the intensity of illumination from the broadband LED and the height of the detection chamber [131].

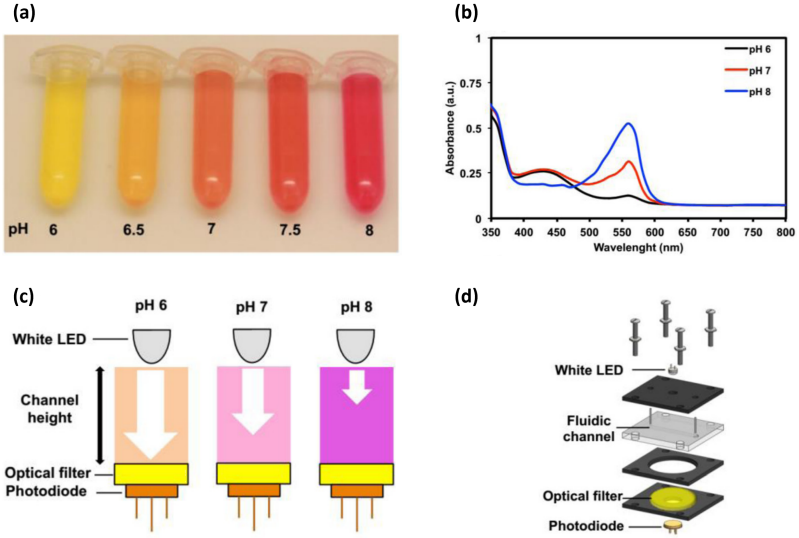

Figure 2.17: Functionality principle of pH sensor and characterization. (a) Color change of phenol red at different pH levels, (b) absorbance spectra of culture medium at different pH values, (c) schematic overview of detecting level of light absorption in culture medium, (d) schematic overview of the fabricated detection chamber for pH sensor [131].

2.10. Summary

This Chapter elaborated on a number of OoC definitions that are important for understanding the project. The key organs that are used in OoC technology were discussed regarding the subjects microfluidics, tissues, stimulation and sensing. It also introduced the physiology of the BBB and the gut and the importance of the interrelation between those two organs was made clear by the fact that an imbalance in signalling can cause severe mental issues or digestion problems. In addition, different types O_2, TEER and pH sensors that can play an important role in quantifying cell behavior were elaborated on. O_2 levels give insight into cell behavior and differentiation, TEER values provide information about level of integrity of the cell barrier and pH levels can be a measure of cell behavior, enzymatic behavior and cell death.
Since the context of the research has been made evident, the next Chapter describes the device that was developed to incorporate all topics discussed in this Chapter.

3

Design and fabrication

With sufficient background provided by the previous Chapter, this Chapter delves into the design and fabrication of the linking system of the multi-OoC device. The goal of this Chapter is to create context on how the Wyss Institute uses the conventional chips so that it is clear why certain design choices were made. It also elaborates on how the sensor chips are fabricated and discusses the separate components of the linking system.

3.1. Wyss OoC set up

The Wyss Institute for Biologically Inspired Engineering uses components and materials from Emulate[1], a former Organ-on-chip technology spin-off from the Wyss institute and currently a fully independently operating company. It is important to understand the Emulate set up in order to comprehend why certain decisions were made at a later stage.
The commercial OoC setup consists of four main components (Fig. 3.1): The ZOË culture module, the ORB hub module, the POD system and the CHIP-S1 stretchable chips.

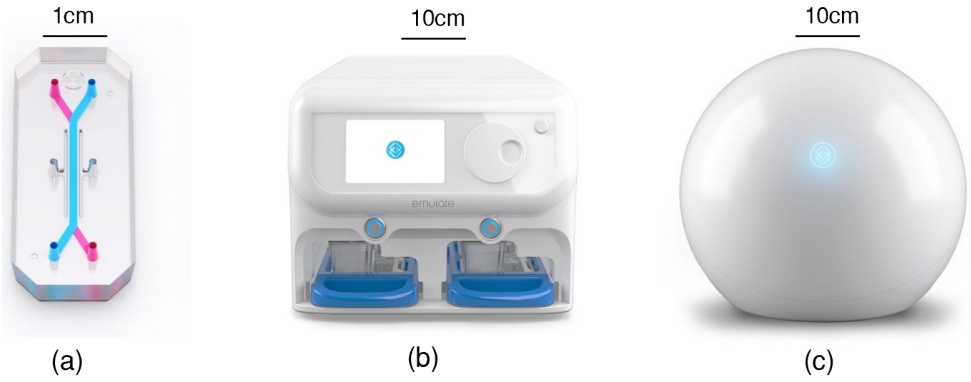

Figure 3.1: The three main Emulate components. (a)CHIP-S1 stretchable chips. (b) ZOË culture module. (c) ORB hub module [138].

The CHIP-S1 is made from 100% PDMS and consists of two channels separated by a porous membrane that allows for cell-cell interaction like those that are seen *in vivo*. The top channel is seeded with epithelial cells and the bottom channel with endothelial cells. On both sides of the fluid channels a vacuum channel is located that provides the mechanical stresses in order to emulate the *in vivo* environments of some cell types.

[1]Emulate was founded by Donald Ingber in 2013 and is the current market leader in commercial OoC products [137]. More information on www.emulatebio.com.

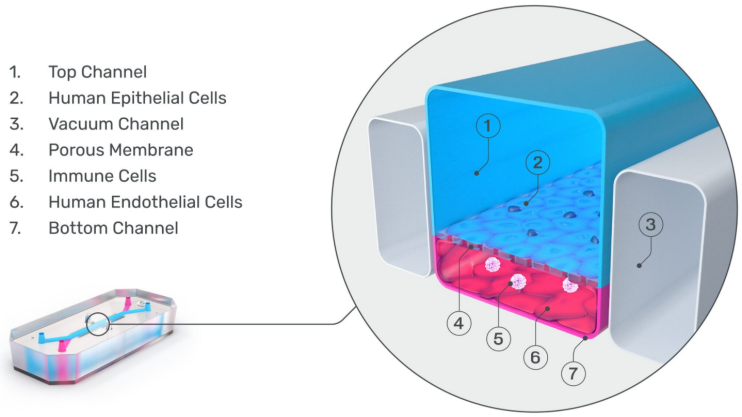

Figure 3.2: Cross-section of Emulate PDMS chip showing the basal channel (lined with endothelial cells), the apical channel (lined with epithelial cells) , the membrane and the vacuum chambers. [138]

The ZOË culture module's main goal is to provide the dynamic flow of media and the mechanical forces that help to recreate the microenvironment that cells normally experience *in vivo*. Two trays carrying up to a total of 12 chips can be loaded into the ZOË (Fig. 3.3a. Each chip is housed within a portable module that holds both the inflow and outflow of the basal and apical channels and guides the flows to the corresponding inlets and outlets of the chips (Fig. 3.3b). The connectors on top of the reservoir lid are connected to the ZOË module which in turn provides the correct pneumatic pressures.
The ORB hub module is located outside the incubator and connects to the ZOË. It generates a mix of 5% CO_2 supply gas to the ZOË and provides the vacuum required to apply chip stretching (-70 kPa).

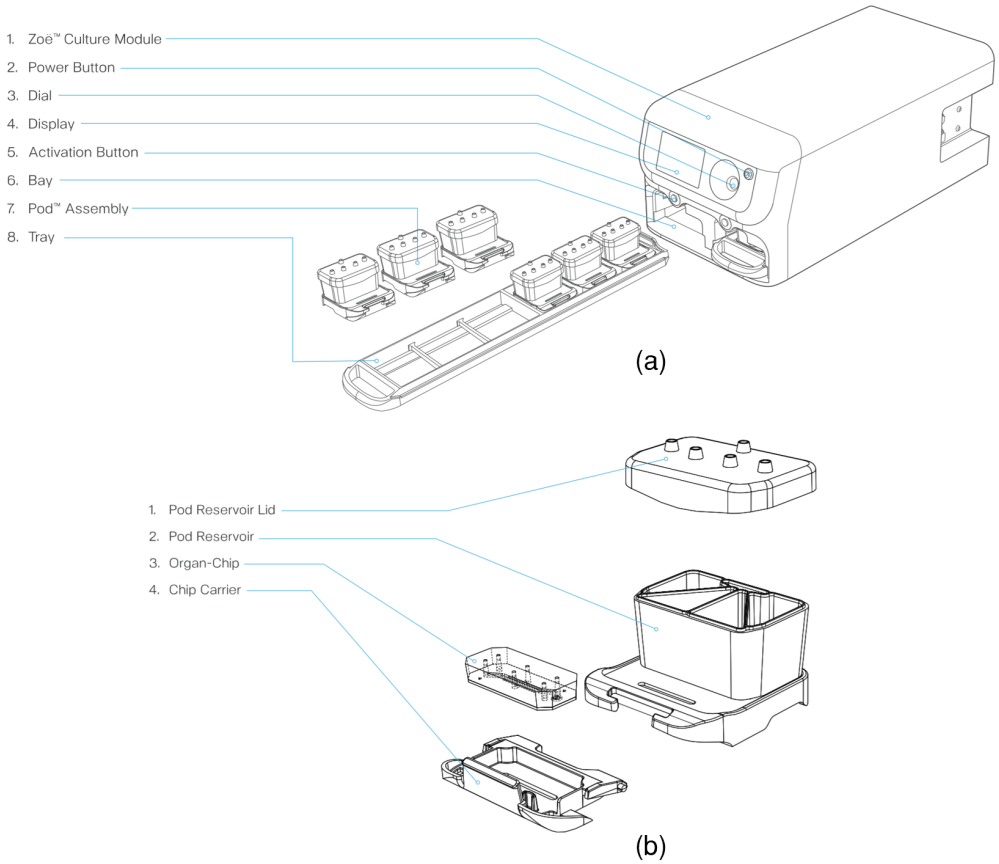

Figure 3.3: In-depth schematic of Emulate ZOË and pod module used for conventional chip usage [138].

3.1.1. Wyss sensor chip

The Wyss Institute has developed a chip compatible with the Emulate system that can monitor TEER and O_2 values of the cells in the apical and basal channels. These chips are comprised of several layers of PDMS bonded together, housing channels, outlets, inlets and a PDMS membrane all with the same dimensions as the Emulate chip. Both the apical and the basal channels contain two spots of fluorescent dye necessary for oxygen level sensing. The PDMS parts are sandwiched in between two polyethylene terephthalate (PET) films with gold electrodes deposited on them used for TEER readings. This layering and assembly can be observed in Fig 3.4a. Everything is fit into a printed circuit board (PCB) with electrode connections running from the electrodes on the PET to the back side of the PCB. Thereafter, this assembly is sandwiched between two thermal adhesive layers and a 1mm thick PDMS layer is added on the top part. These chips can than be screwed together with the same microfluidic component and pod as in the conventional Emulate assembly (Fig. 3.4b). This piece can in turn be fit into a custom made 3D printed tray that can hold six sensor chips and has rectangular spring-loaded male connectors at each chip location that can transport signals to a DB25 female connector located on the out most part of the tray. The tray fits in the ZOË which provides the necessary dynamic flow of media and the mechanical forces.

3.1.2. Fabrication of the sensor chip

The apical, basal and membrane components of the chips were fabricated from PDMS (Ellsworth Adhesives #4019862)[2] with a 10:1 ratio of base to curing agent ratio. In order to create the thin PDMS slabs, the PDMS was spin coated onto a 150mm by 150mm sheet of polycarbonate. The sheet was placed into a vacuum chamber for 5 minutes to remove any air bubbles after which it was placed in a 60°C oven for 1 hour. The 1mm apical layer consists of 2 layers of spincoated PDMS with a 400 μm thickness and one layer of 200μm thickness. In between spincoating, the previous PDMS layer was plasma treated to increase adherence of the new layer. The Graphtec CE5000-60 plot cutter was used to cut out the gaskets from the PDMS slabs (maximum of 24 gaskets per slab). The gasket designs were loaded in the Graphtec Studio Software in DXF format and settings from Tab. 3.1 were used to cut the different gaskets.

Table 3.1: CE5000-60 Plot Cutter settings.

Material	Blade height	Blade type	Offset	Speed	Acceleration	Cut force	Passes
1mm PDMS	1.1mm	CB15U- 60°	0	1	1	22	2
200μm PDMS	300μm	CB15U- 30°	0	1	1	17	1
Thermal adhesive	300μm	CB15U- 60°	0	1	1	17	2

Silane bonding was used to bond the electrodes to the PDMS gaskets. A 300ml solution of 5% (3-Aminopropyl) triethoxysilane (APTES) and a 500ml solution of 1% (3-Glycidyloxypropyl)trimethoxysilane (GPTMS) in MiliQ water was prepared. Before silane bonding the gaskets and electrodes were plasma treated to activate the surface of the materials. The gaskets and electrodes were then lowered in the silane solutions for 20 minutes. After the 20 minutes, the materials were washed with water and dried using compressed air. Then, the electrodes were manually aligned with the PDMS gaskets and pressed together to allow for bonding. The bonded parts were left in a 60°C oven with 3kg of added weight on top for at least 3 hours.
In order to allow for oxygen sensing in the chips, oxygen nanoparticles from Pyroscience[3] were added to specific locations on the inside of the channels. A suspension of 10mg of particles with 15ml of chloroform was made and a P2 pipette was used to spot 0.4μl of nanoparticles on the basal channel and 0.5μl on the apical channel. The O_2 spotted and bonded components were stored in a dark 60°C oven until the membrane fabrication was completed. The membranes were fabricated using the automated membrane fabricator (AMF) and pre-made silicon membrane wafers. 0.09ml of PDMS was added to the center of each silicon membrane wafer and plasma treated PC sheets were placed on top of the PDMS to allow for even spreading. On top of the PC sheets a PDMS solid block was added before the assembly was placed into the AMF to allow for equal pressure distribution across the wafer. The AMF was turned on and left overnight to exert pressure on the PDMS in order to form thin sheets of PDMS membranes. The next day the wafers were taken from the AMF, the PDMS block was removed and the wafer was detached from the PC film with the adhered PDMS membrane. The membranes as well as the O_2 spotted apical gaskets were then plasma treated. The

[2]Both the silicone and the curing agent were purchased from: https://www.ellsworth.com/products/by-market/consumer-products/encapsulants/silicone/dow-sylgard-184-silicone-encapsulant-clear-19.9-kg-kit/
[3]Purchased from: https://www.pyroscience.com/en/products/all-sensors/oxnano

PDMS side of the gasket was then lowered onto the plasma treated side of the PDMS membrane, pressure was applied with fingers to allow for bonding and the components were placed into a 60°C oven for 2 hours. After bonding, excess membrane was removed from the sides and the ports that access the bottom channel. For the full assembly of the PDMS and electrode parts, both the basal and the apical PDMS gaskets were plasma treated and aligned under a microscope. Again, pressure was applied using fingers to allow for bonding of the two components before the bonded components were transferred to a 60°C oven overnight. The different layers of the chip and an example of the assembly is shown in Figure 3.4a
The O_2 spotted PDMS and electrode assemblies are connected to a PCB using silver epoxy. A small amount of silverepoxy was added to the two pads on the top service of the PCB and on the two basal pads of the chips. The chips is then pressed into the PCB so that the silver epoxy connects both components. The assemblies were left overnight in a 80°C oven overnight and checked for functionality with a multimeter the next day. The PCB is then sandwiched in between two thermal adhesive layers (3M™ Thermal Bonding Film 583) and a 1mm PDMS layer was added on top. Both the thermal adhesive layers and the PDMS layers were cut with the Graphtec CE5000-60 plot cutter with settings shown in Tab. 3.1. The adhesive layers were aligned to the PCB and run through a laminator set at a temperature of 140°C and speed 6 several times between two sheets of paper to prevent the thermal layers to stick to the laminator. The PDMS layer was plasma treated and also aligned under a microscope to the PCB-thermal adhesive assembly and run through the laminator set at a temperature of 140°C and a speed of 8. The full assembly as well as the Emulate pod can be observed in Fig. 3.4b.

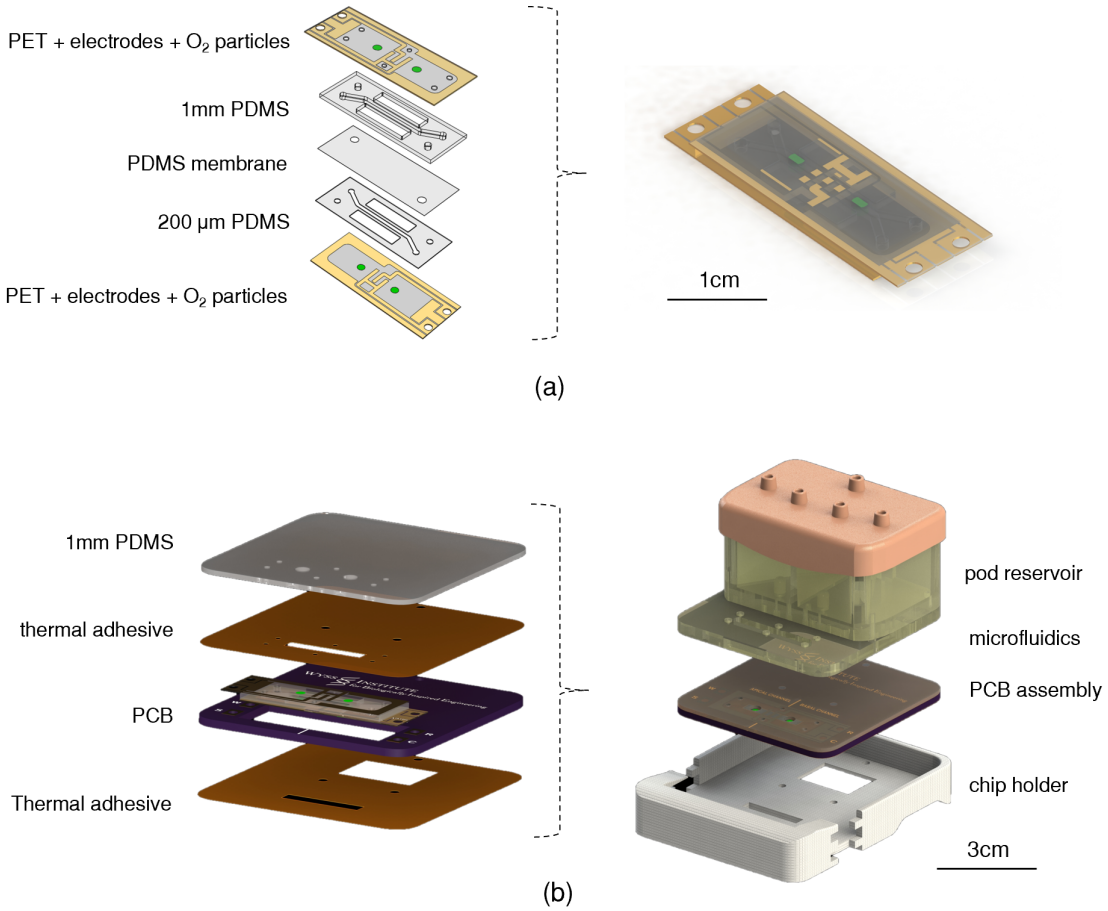

Figure 3.4: Sensor chip complete assembly(a) Sensor chip layering and assembly. (b) PCB assembly and compatibility with Emulate pod and microfluidics.

3.2. Design considerations

From the information in the previous Section, it is now clear what the Wyss Institute OoC set up looks like and why the sensor chip has its specific shape and dimensions. In order to create a platform that can link two of these chips with integrated sensor components, it is necessary to establish the constraints of the design in an effort to make it as functional as possible within the goals of the Wyss Institute.
In the short term, the Wyss Institute aims to use the linking platform to substantiate the functioning of their integrated TEER and O_2 sensors, using this information in their publications[4]. On the long term, it will be used for experiments on linking BBB tissue with the microbiome using iPSCs. These short term and long term goals make that the device has to meet certain requirements in order for it be practical. The main requirements are listed here:

- First and foremost, the device should be a compact as possible. For both the short term and the long term goals of the Wyss Institute, it will be necessary to run multiple devices in parallel. When performing tissue culture work, devices are used inside tissue hoods and incubators. Both environments have limited space available and bulky instruments can make it challenging to work efficiently.
- The device should be relatively inexpensive to produce. This prototype will be the first linking system at the Wyss Institute with integrated sensor components and it is likely that it will undergo several other iterations.
- Additionally, it should be easy to fabricate. Since the system will be used by several research groups within the Wyss Institute, it is vital that the device fabrication is intuitive and accessible. Researchers and research assistants should be able to get trained in the fabrication process, which means that it should only involve manufacturing techniques that are available for everyone at the Wyss Institute.
- When the chips are connected to the device, the tissues should still be available for standard imaging techniques (e.g., microscopy). The working distance of a microscope is defined as the distance between the front end of a microscope objective and the surface at which the sharpest focusing is obtained [139]. The most used objectives for visual inspection of the cells range between a 5X and 20X magnification. The maximum working distance of these objectives is 8.7mm [140].
- The microfluidic component should be a separate item that is easily detachable and replaceable. Since different experiments require different linking strategies, variations of the microfluidic components with the same dimensions should be able to fit onto the system without having to build a completely new device.
- The total length of the channels through which the fluids are perfused should be as short as possible to limit pressure drop. The pressure drop is defined as the difference in total pressure between two points of a fluid carrying network [141]. Since cells are sensitive to pressure differences, it is necessary to reduce the channel length in order to keep the environment as homogeneous as possible between the two connected tissues.

These main requirements were taken into account when designing the system. The next Section describes the linking system and elaborates on how it satisfies the demands mentioned above.

3.3. The linking system

An overview of the final complete assembly is shown in Figure 3.5. The system is comprised of 4 main components: the microfluidics, the detachable holder, the base and the pump unit. All parts in the design are developed using Solidworks 2021 software. Each component will be discussed more in depth in the following Sections. For a more detailed description regarding fabrication, please refer to Appendix A. To see the various iterations of the design, please refer to Appendix B.

[4]The Wyss Institute is yet to publish the design and validation of their sensor chip and is still gathering information about its functionality.

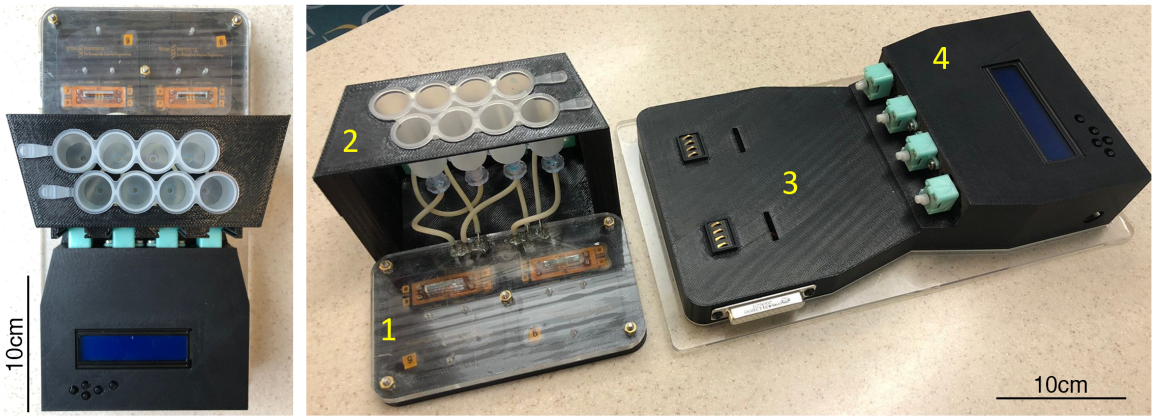

Figure 3.5: Complete device assembly. (a) Top view of complete assembly. (b) Overview of different components: 1. Microfluidics 2. reservoir component 3. base 4. pump unit.

3.3.1. Microfluidics

The microfluidic component contains the channels that guide the fluid, coming from the input reservoirs, through through the chips to the output reservoirs. It consists of three layered PMMA sheets with a 1.5mm thickness, separated by 2 layers of Styrene-ethylene-butylene-styrene (SEBS) with a 100μm thickness (Fig. 3.6c). This thermoplastic elastomer has great properties to be used in the system. It is optically transparent, biocompatible, allows for low osmolarity changes and can adhere to PMMA relatively well. Depending on the aim of a specific experiment, the SEBS layers have channel cut-outs connecting different inlet and outlet ports, with a 1.2mm diameter, that are present in the PMMA (Fig. 3.6a). All parts are cut using a Epilog Legend 36EXT 75 Watt CO_2 laser cutter with settings shown in Table 3.2. The layers are aligned on top of each other and left in a 90°C oven for 1 hour under 4 kg of weights to enable adhesion.
On the bottom part, around the inlets and outlets that are in contact with the chips, eight 400μm thick PDMS rings are attached to the PMMA with an inner diameter of 1.6mm and an outer diameter of 2.5mm using PSA rings of the same dimensions (Appendix C.7). This increases the connection between the microfluidics component with the chips and prevents leakage. These rings are visible in Figure 3.6b. The in- and outflow connection points are made from steel connectors with an inner diameter of 0.9mm and an outer diameter of 1mm that are attached to the PMMA using epoxy glue. The whole microfluidic component is pressed down onto the chips using 5 M4 screws and nuts.

Table 3.2: Epilog 36EXT laser cutter setting for PMMA and PSA.

	Speed	**Power**	**Frequency**
1.5mm PMMA	20	60	5000
PSA	100	20	2000
100μm SEBS	75	15	2000

Initially, the microfluidic component consisted of two layers of pressure sensitive adhesive (PSA) in stead of SEBS. However, the first experiment (described in Chapter 5) revealed that PSA releases from the PMMA after 5 days of incubation. This is why several experiments were done with the 100μm thick SEBS sheets to determine the best protocol for adherence of the SEBS material to PMMA. It was tested whether plasma and heat treating the PMMA and SEBS would influence the adherence of the two materials. For the experiment, twelve serpentine channels were laser cut from the SEBS sheet and sandwiched between two laser cut PMMA parts. For six of the assemblies the SEBS and PMMA surfaces were plasma treated. Three of the plasma treated assemblies were then left in a 90°C oven under weights for 24 hours and three for 1 hour. The other six assemblies were not plasma treated. Half of these six were left in the oven for 24 hours and half were taken out after 1 hour. After this step, the channels were perfused with water containing blue food dye for 7 days (Appendix C.2). No leakage was observed for the assemblies that were not plasma treated and were left in the oven for 1 hour. The other protocols all showed at least one sample that leaked. Therefore, the PSA was replaced by SEBS using this assembly protocol.

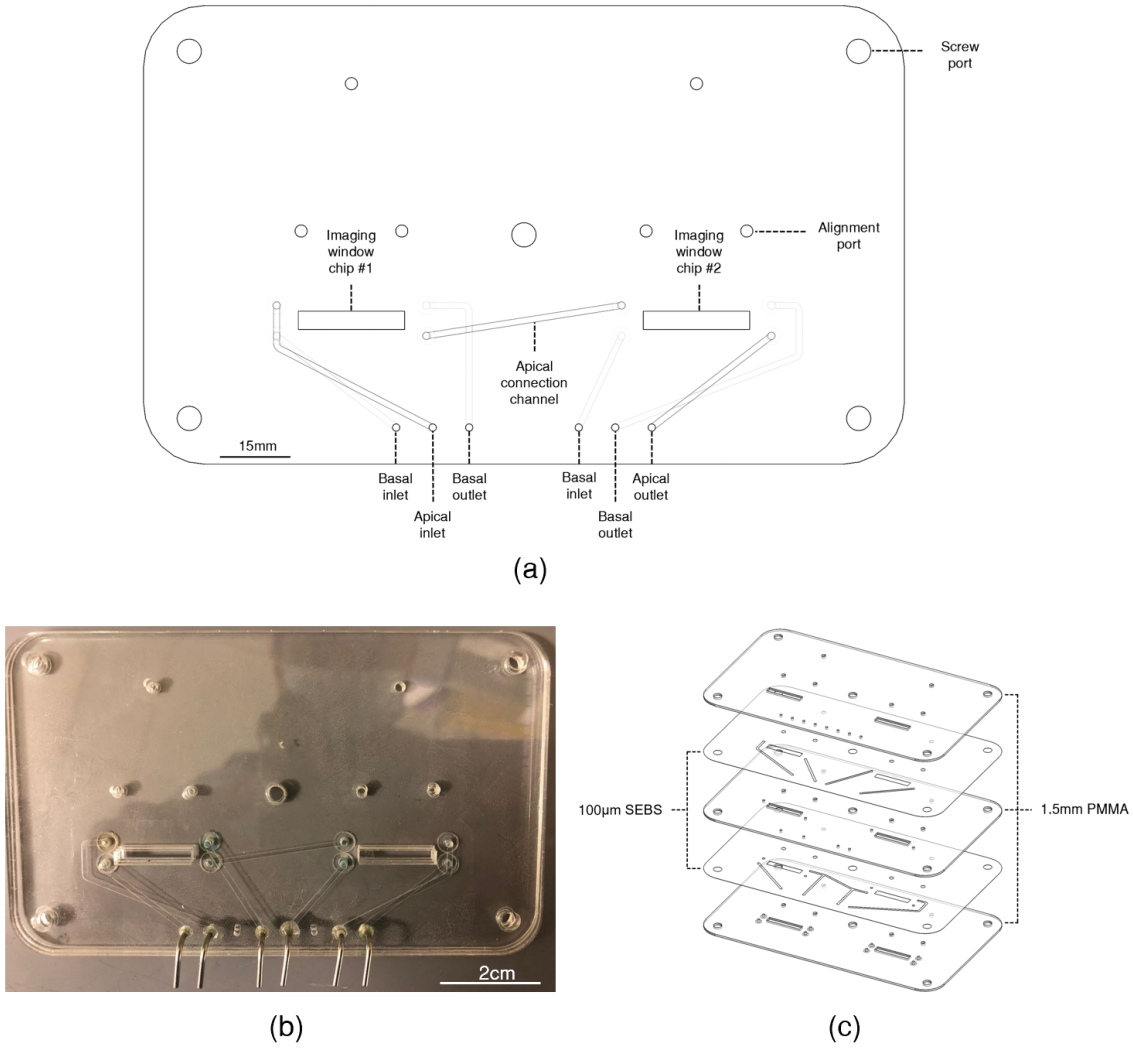

Figure 3.6: Complete microfluidic assembly with apical connection overview. (a) Top view of the complete microfluidic CAD assembly. (b) Top view of complete microfluidic assembly. (c) Overview of different layers. The PMMA layers contain several inlets and outlets for the microfluidic channels, screw holes and cut outs for visual inspection of the cells. The SEBS layers also contain the channels.

3.3.2. Detachable holder

The detachable holder (Fig. 3.7a and 3.7b) acts a portable component that, when fully assembled, can be detached from the base and pump unit and transport the chips, microfluidics, reservoirs and pump heads. The detachable holder is 3D printed with the Fortus 400mc printer, which uses fused depositioning modeling with the material Polylactic acid (PLA) . The reservoir containers that are located in the holder are provided by Chipshop[5] and have 4ml of volume in each tank (Fig. 3.7c). Tubing is used to connect the microfluidics with the reservoirs and have an inner diameter of 0.8mm and outer diameter of 2mm. 8 female plastic luer locks are used to connect the tubing to the reservoirs. On the backside of the component, four slots are located in which the detachable pump heads can be slit, as is shown in Fig. 3.7d. The whole component is detachable to allow for imaging without having to detach any of the tubing and decreases the possibility of air being introduced into the channels.

[5]Acquired via: https://www.microfluidic-chipshop.com/catalogue/accessories/liquid-storage/liquid-storage-tanks/row-of-four-4-5-ml-tanks-with-luer-interface-cap-fluidic-233/

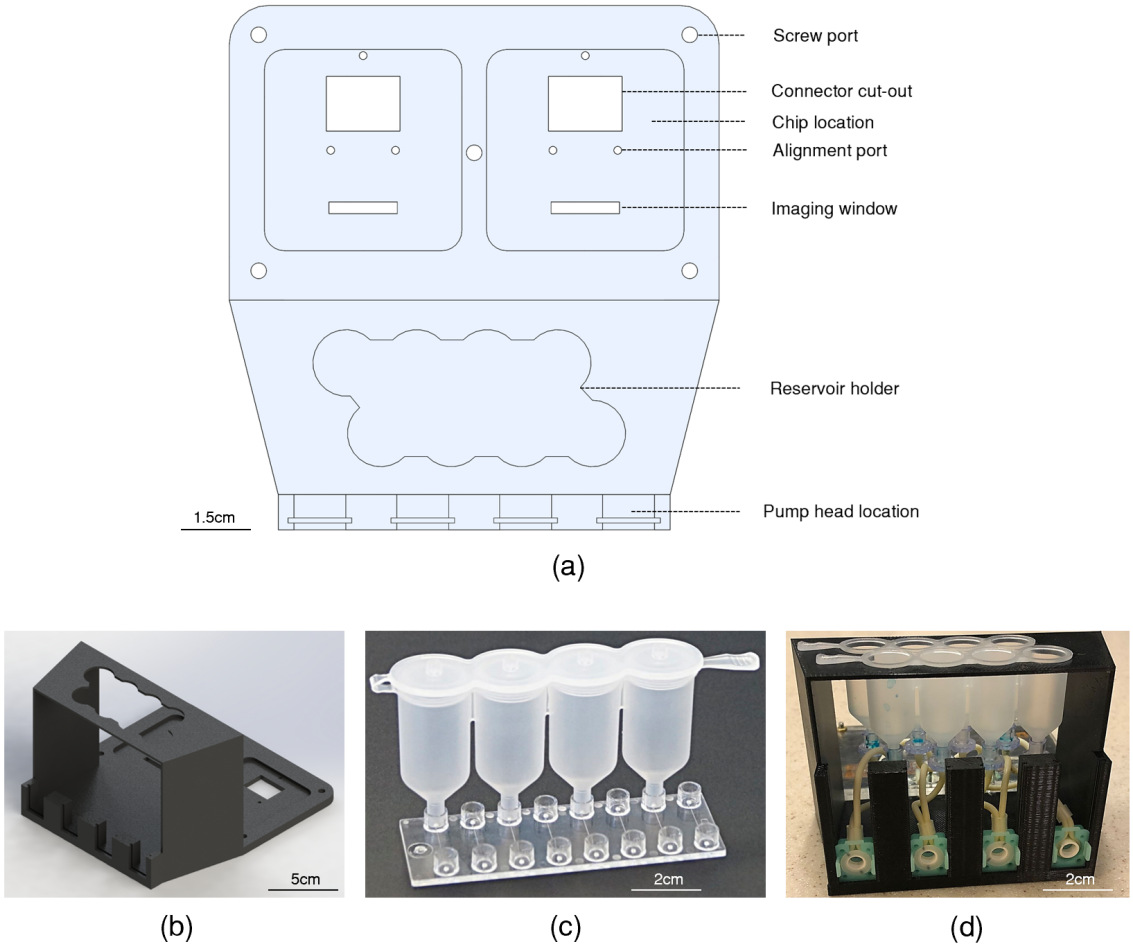

Figure 3.7: Main detachable holder components. (a) Top view of the detachable holder CAD model. (b) CAD render of the detachable holder. (c) Chipshop 4ml plastic reservoirs.(c) Back view of the reservoir component showing the detached pump heads and plastic reservoirs in place.

3.3.3. Base

The base acts as a hollow structure on which the detachable holder is placed. It contains all of the electronics that guide electrical signals from the sensor chips to external computers and vice versa and shields these components from the humid incubator environment.
The base (Fig. 3.8a and Fig. 3.8b) was also 3D printed with the Fortus 400mc printer using PLA. On the left side of the base, a DB-25 female connector obtained from McMaster-Carr[6] (Fig. 3.8c) is connected with two M3 flat head screws. Two rectangular spring-loaded connectors (Fig. 3.8d), also obtained from McMaster-Carr, are used to make contact with the exposed electrode connectors located on the bottom side of the sensor chips (See Appendix E.1). The rectangular spring-loaded connectors are elevated 3mm above the rest of the base, since this is the thickness of the bottom of the detachable holder component that has to be bridged in order to make contact to the sensor chips. Standard wiring soldered to the rectangular spring-loaded connectors and the DB-sub connector links the two. For a more detailed description, please refer to Appendix A.
It is worth noting that the base could be designed with much smaller dimensions, but extra space is reserved inside of the base for extra electronics such as a compact potentiostat or a custom made O_2 sensor[7]. The decision was made to leave this space available in the current design considering the long term goals of the Wyss Institute.

[6] https://www.mcmaster.com/serial-connectors/circuit-board-d-sub-connectors/connection-type computer/
[7] Currently being developed by the biosensors team at the Wyss Institute

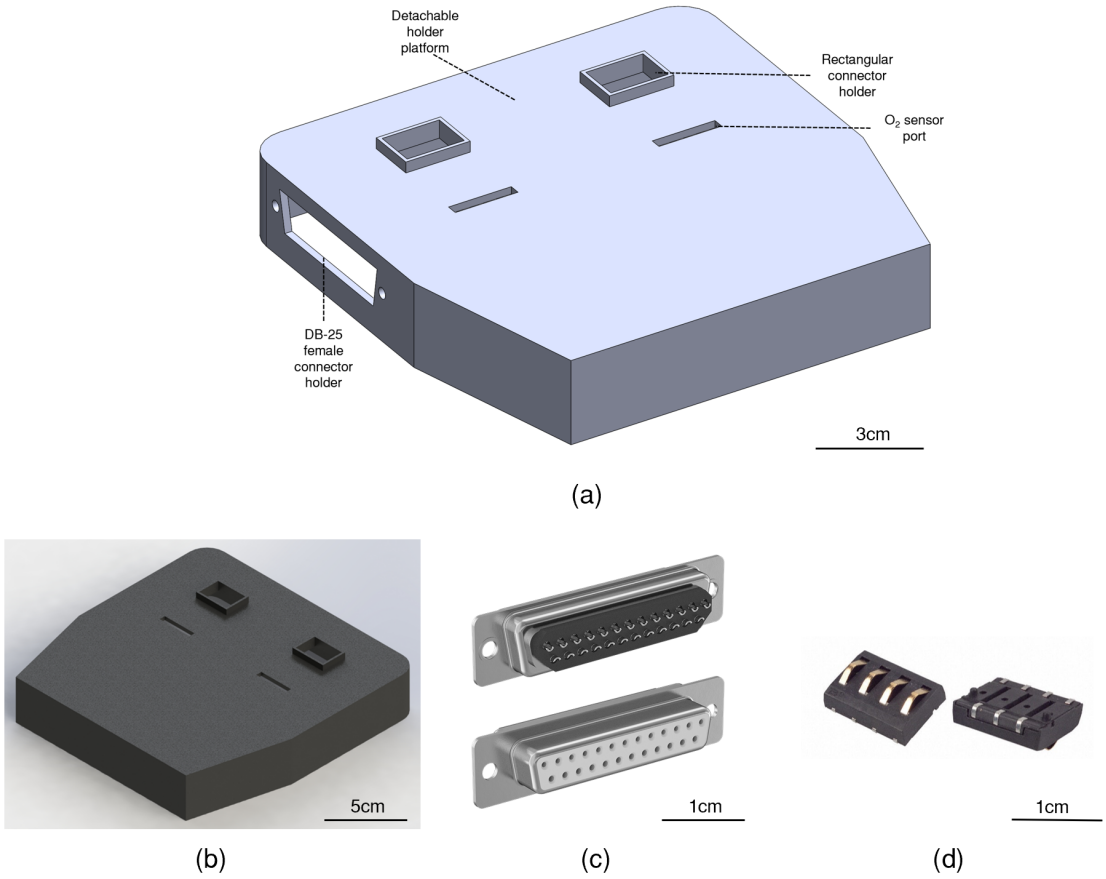

Figure 3.8: Main base components (a) Perspective view of the CAD base model. (b) CAD render of the base. (c) Back (top) and front (bottom) of the DB-25 female connector (d) Rectangular spring-loaded connectors.

3.3.4. Pump unit

The pump unit serves as a housing to both shield the micro-controller from the humid incubator environment and as a holder for the pumps with detachable heads.
It is comprised of a 3D printed housing made from PLA (Fig. 3.9a and Fig. 3.9b), a control unit provided by the Wyss Institute (Fig. 3.9c) and four DC peristaltic ring pumps with detachable pump heads[8] (Fig. 3.9d). The housing contains open spaces for the four pumps and the screws to secure them, the screen and power cable of the control unit and it's buttons to control it. The pump control unit allows for the control of a total of eight pumps via a visual interface (Appendix A). Flow rate can range from 1μl/min to 30μl/min and can be set for every pump individually. The pump control unit is connected to the pumps by standard wiring and the pumps are secured on the PLA housing with eight M3 flathead screws. The extended part, located on the bottom of the housing underneath the pump spaces, has two functions. First, it provides extra space for the wiring running from the pumps to the control unit, making it easier to work with when assembling the different components. Second, it makes contact to the backside of the base. This is important because when the detachable holder is removed from the rest of the assembly, a small amount of force is needed to disconnect the pump heads from the pumps. The direct contact of the pump unit with the base prevents the pump unit from moving during this process.

[8]https://www.pumps-valves.eu/rp-q2-rp-q3-miniature-peristaltic-pumps-head-exchangeable/

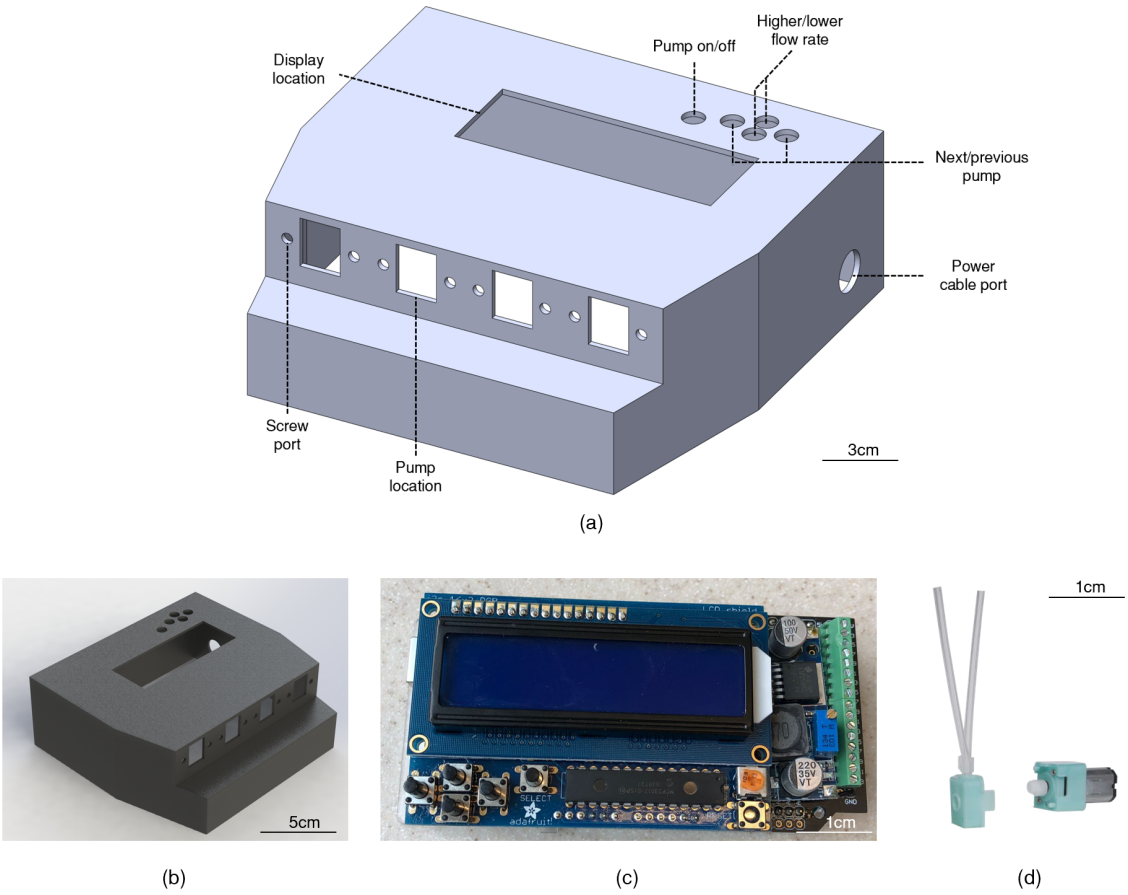

Figure 3.9: Pump unit components. (a) CAD model of the PLA housing. (b) CAD render of the PLA housing (c) Pump control unit. (d) DC peristaltic ring pumps with detachable heads.

3.3.5. Obtaining O_2 and TEER values

In this design, no sensor components could be completely integrated into the base due to limited resources and time. Therefore, sensor read-outs have to be carried out using external instruments. Here, the measurement protocols are described for doing O_2 and TEER read-outs.

O_2 values can be obtained by separating the detachable holder (including the sensor chips, microfluidic component and reservoirs) from the system and transferring it into a tissue culture hood. Put the component on a heat tray that is set to 32°C. Since the O_2 measurements can be influenced by temperature, position the temperature sensor near the O_2 spotted locations. Place the fiber optic sensor on the areas that contain the O_2 particles and connect the FireSting-O2[9] meter (Appendix F.1) to a laptop. Use the Pyroscience software to start and save the O_2 data and repeat this for all four O_2 spots on both chips.

In order to gather TEER information, a VGA cable is used to connect an external Ivium potentiostat[10] (Appendix F.2), set at 100μA and a frequency range of 10 - 100000Hz, to the system. The potentiostat is also connected to a laptop containing IVIUM software that is used to start the measurements and save the data.

An example of TEER data output is shown in Fig. (3.10). This example shows that for lower frequencies, the chip with the empty channels has much higher resistance compared to the chip filled with PBS. This is in line with a study done by Henry et. al. (2017), in which they found the resistance to be relatively stable for frequencies in the range of 0.5Hz to 100Hz [125]. It was decided by the biosensors group of the Wyss Institute to quantify the change in barrier function according to the resistance values at 100Hz.

[9]All sensor components can be obtained from Pyroscience: https://www.pyroscience.com/en/products/all-meters/fso2-c4
[10]https://www.ivium.com/product/compactstat/

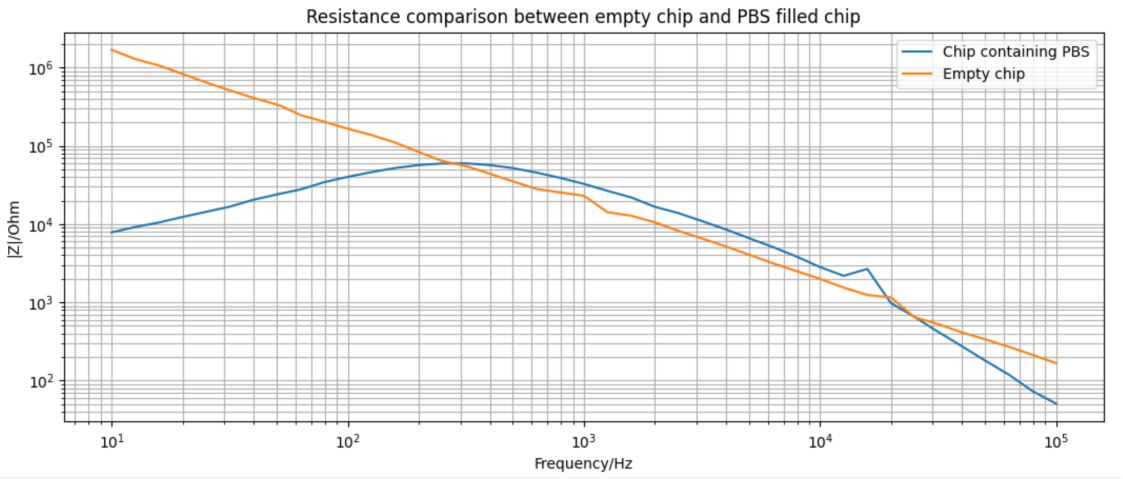

Figure 3.10: Example of TEER data. The measured resistance at varying frequencies is shown for two different situations. In the empty chip, resistance shows a straight path of decreasing resistance for an increasing frequency. The chip containing PBS shows a similar pattern for higher frequencies, but is relatively stable for lower frequencies.

3.4. Results

With respect to the design considerations mentioned in Section 3.2, the final design meets most of the main requirements.

- The final device has a total height of 10.35cm, a width of 12.50cm and a depth of 24.1cm. With these dimensions, 16 linking systems could fit into a single Thermo Fisher 3121 Incubator[11], of which the Wyss Institute owns several.

- The main materials from which the components of the linking system are made include PLA, PMMA and SEBS. All three are relatively inexpensive. Most of the other components (e.g., connectors, pumps and the Raspberry Pi 4 micro-controller) are commercially available and reusable.

- The dominant fabrication instruments include the Epilog Legend 36EXT 75 Watt CO_2 laser cutter and the Fortus 400mc 3D printer both of which are available to all employees of the Wyss Institute after 1 hour of training. Additionally, fabricating the device can generally be completed within a day, assuming all materials are in-house. The printing process takes 7 hours and 10 minutes. In the meantime, the PMMA, PSA and SEBS can be cut with the laser cutter and assembled to form the microfluidic component. After the printing has finished, the pumps and connectors can be screwed in place and wiring can be soldered. It should be noted that this does not include the fabrication of the sensor chips, which can take up to 6 days.

- When the chips and the microfluidic component are connected to the detachable holder, the minimal working distance of a microscope is limited by the thickness of the microfluidic component for the apical channel and by the thickness of the bottom of the detachable holder for the basal channel. With the current materials, this means that the minimal working distance of a microscope used for the apical channel can be 6.8mm and for the basal channel 3.1mm. This is sufficient since objectives (5X, 10X and 20X magnification) used at the Wyss Institute can have a working distance of up to 8.7mm [139].

- The microfluidic component is a separate item and is easily detachable using screws and bolts. This is discussed more in-depth in Chapter 6.

- The total channel length was kept as short as possible, with the longest path being 274mm, including the proposed mixing geometry of Chapter 4. Suggestions for decreasing this total length are discussed in Chapter 6.

[11] Visit https://store.clarksonlab.com/3121.aspx for more information

3.5. Summary

This chapter provided context about the usage of the sensor chip and its design. It also provided insight into the different components of the linking system and the way they are fabricated. The final design consists of a microfluidic component, a detachable holder, a base and a pump unit. It is easy and inexpensive to fabricate and is compact enough to fit multiple systems in one incubator. Additionally, it is compatible with standard microscopy.

Many parts of the design could have been optimized for usability or functionality, but due to limited time it was decided to focus on the microfluidic component. The next Chapter explains how it was attempted to find the most efficient geometry to mix the effluent of the first chip with a new flow that contains medium for the second chip.

4

Mixing

Now it is time to dive deeper into fluid mechanics. When different cell types are linked with microfluidics, it is important to understand the way particles behave inside these flows. Additionally, this chapter focuses on the most efficient way to mix the outflow of the first chip with a nutrient rich flow for the second chip. It concludes with a proposed mixing geometry that can incorporated using the same fabrication techniques mentioned in the previous Chapter.

4.1. Mixing of two laminar flows

In order to provide the effluent basal flow of the first chip with new nutrients for the cells in the second chip, these two channels need to be mixed. It is important that the two fluids fully mix to make sure the cells are provided with a sufficient amount of nutrients while also getting exposed to effluent molecules from the first chip. The reliably of the final results is therefore largely dependent on the reliability and accuracy of the mixing component.
To combine both flows in the linking model, passive mixing seems the most promising as it is the form of mixing that is easiest to fabricate with low fabrication costs and has a low probability of creating bubbles as compared to some active mixing methods [142]. Due to low flow velocity and small feature size in microchannels, Reynolds number is low and there are no turbulent fluctuations in a homogenize fluid at the microscopic scale [143]. For the specific dimensions of the PSA-PMMA microfluidic component, Reynolds number is determined as follows.

$$Re = \frac{u \cdot D_h}{v} \tag{4.1}$$

With

u = mean flow velocity ($\frac{m}{s}$)
D_h = hydraulic diameter (m)
v = kinematic viscosity ($\frac{m^2}{s}$)

Taking into account the parameters for our specific system that has a steady flow rate of 60μl/h, a kinematic viscosity of $6.969 \cdot 10^{-7}$ $\frac{m^2}{s}$ at 37°C and a rectangular channel with a width of 1mm and a height of 0.1mm, we get a Reynolds number of 0.043. Fluid flow with $Re << 1$ is a also known as Stokes flow or creep flow. Stokes flow is characterized by the phenomenon that inertial forces are negligible in comparison to the viscous forces. In terms of mixing, this is vital information since inertial forces play an important role in mixing imposed by structural changes. The absence of these forces create a mixing environment that is mainly dominated by diffusion.
The fact these parameters indeed induce diffusion dominated mixing is supported by the Peclet number, a dimensionless number that depicts the ratio of the rate of advection of a physical quantity by the flow to the

diffusion rate of that same quantity [144]. The Peclet number is defined as:

$$Pe = \frac{u \cdot \rho \cdot c_p \cdot D_h}{k} \tag{4.2}$$

Where

u = mean flow velocity ($\frac{m}{s}$)
ρ = density ($\frac{kg}{m^3}$)
c_p = heat capacity ($\frac{J}{kgC}$)
D_h = hydraulic diameter (m)
k = thermal conductivity ($\frac{W}{mC}$)

Calculating the Peclet number for the PSA-PMMA parameters leaves us with $Pe = 0.2$, showing again the importance of diffusion over convection.

4.2. Geometry testing using numerical simulations

4.2.1. Structures

The geometric models used for the simulations are variations of a standard T-micromixer. The main regions include two inlets both with a width of 1mm, one structural design area and two outlets with a width of 1mm. Inlet 1 merges with the second inlet in a curve with a radius of 1mm and outlet 1 splits from the structure in a curve with a radius of 1mm (Fig. 4.1).

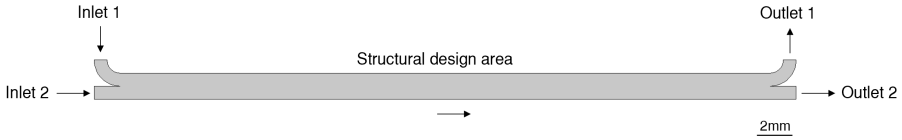

Figure 4.1: An example of a schematic diagram for the mixing area. Every geometry has two inlet channels and two outlet channels. The structural design area will be adjusted in order to find a difference in mixing performance. The arrows depict the flow direction.

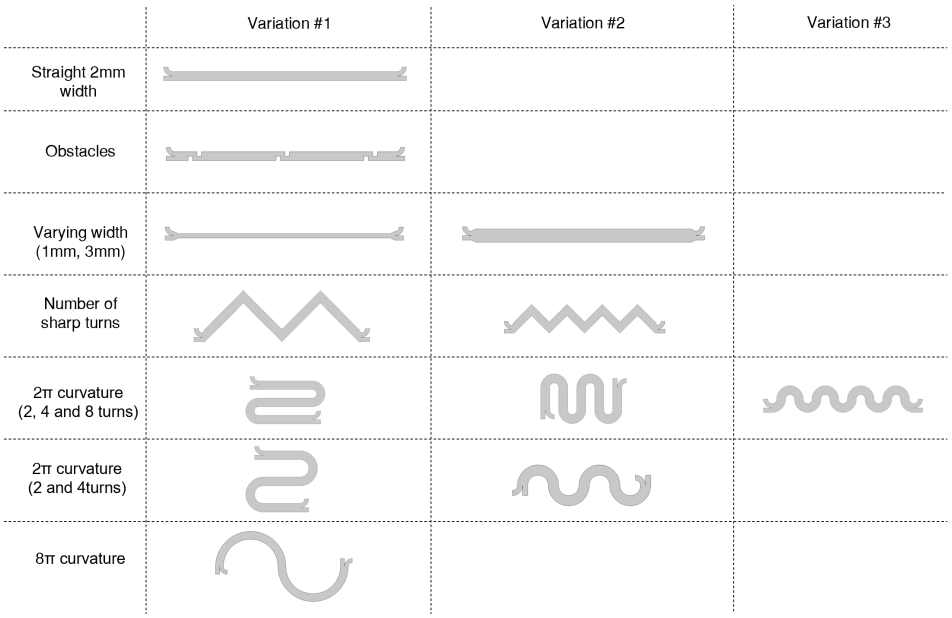

Figure 4.2: Overview of various geometries tested. The goal of using these geometries is to determine the effect of the number of turns, the shape of the turns and the channel width on the mixing performance.

The structure variations for the structural design area were chosen based on literature and on the findings from Section 2.1 [145]. Knowing that the mixing in our system will be mainly diffusion driven and that there is limited space on the microfluidic platform, structures varying in width, number of curves, curve radius, number of sharp turns and obstacles were introduced. All structures are exactly 16π mm in length. Creativity was limited by the fabrication of the microfluidic component by the laser cutter (Appendix C.1).

4.2.2. Flow dynamics

The flow behavior was simulated using the laminar flow module of COMSOL Multiphysics 5.6 which numerically solves the Navier-Stokes equations and the continuity equation [146]. Incompressible flows under steady-state conditions were used for the simulations and the boundary conditions include a constant velocity for the two inlets, no-slip velocity for the walls and zero pressure for the two outlets. These laminar flow properties lead to a Navier-Stokes equation defined as:

$$\mu\nabla^2\mathbf{u} - \nabla p + \mathbf{f} = 0 \tag{4.3}$$

And the following continuity equation:

$$\nabla \cdot \mathbf{u} = 0 \tag{4.4}$$

where $\mathbf{u}$ is the fluid velocity, ∇p is the pressure gradient, μ is the dynamic viscosity and $\mathbf{f}$ is the applied body force. In terms of discretisation of the mesh, for both the velocity components and the pressure pressure field linear elements were chosen.

4.2.3. Species transport

To simulate the movement of compounds carried by the effluent flow, the transport of diluted species module was used. A concentration of diluted species of 1 mol/m^3 was added to the top inlet at time step 0 to an initial concentration of 0 mol/m^3. The diffusion coefficient for the simulations of the different geometries was set at $2.75 \cdot 10^{-10}$ m^2/s, which is the diffusion coefficient for food dye in water at room temperature [147]. The convection-diffusion equation was used and described as equations 4.5 and 4.6.

$$\frac{\partial c_i}{\partial t} + \nabla \cdot \mathbf{J}_i + \mathbf{u} \cdot \nabla c_i = R_i \tag{4.5}$$

$$\mathbf{J}_i = -D_i \nabla c_i \tag{4.6}$$

In which c_i is the concentration of the species, D_i the diffusion coefficient, R_i the reaction rate expression for the species, $\mathbf{J}_i$ the diffusion flux vector and $\mathbf{u}$ the same velocity vector as used for the laminar flow module.

4.2.4. Mixing performance

The performance of the mixing was determined by measuring the concentration values of the diluted species at a cross section at the end of the bottom effluent channel. The mixing efficiency M ranges from 0 (no mixing) to 1 (100% mixing) was calculated by the following formula:

$$M = 1 - \sqrt{\left(\frac{1}{N}\sum_{i=1}^{n}\left(\frac{c_i - \bar{c}}{\bar{c}}\right)\right)^2} \tag{4.7}$$

Where

M = mixing coefficient
N = total number of sampling points
c_i = normalized concentration
$\bar{c}$ = normalized expected concentration

With the initial conditions of an input flow with a concentration 1 mol/m^3 at inlet 1 and an input flow with a concentration 0 mol/mm^3 at inlet 2, it is expected that in an ideal case with perfect mixing the output concentration at outlet 2 is 0.5 mol/m^3 across the whole channel. M represents the total average percentage of standard deviation of the data points at the outlet 2 cross-section from the perfect mixing concentration.

4.2.5. Mesh

Because numerical solutions strongly depend on meshing parameters, several variations were used to find a balance between computational costs and mixing accuracy. It was concluded that for every structure, most accurate results were obtained with a total number of elements in the range of 50.000 to 60.000. Additional mesh variables were physics controlled.

4.3. Simulations validation

Numerical approximations of real world systems can create quite accurate representations of real life phenomena. However, experimental research can promote numerically approximated fluid behavior even more. Therefore, the mixing simulations were validated by recreating the structures experimentally.
To recreate the simulation structures, the COMSOL structures were laser cut into a sheet of double sided adhesive which was sandwiched in between two layers of PMMA, one of which contained the inlet and outlet ports. Two steel rods were connected to the inlet ports and sealed with epoxy glue. These rods were then connected to two syringes containing a yellow or blue food dye (Ward's science[1]). Everything was then loaded into a NE-4000X double syringe pump programmed with same parameters as in the simulations. An example of a structure being perfused with the food dye is shown in figure 4.3a. Flow was perfused for 2 hours before pictures were taken of the two outlets with the Zeiss Axioplan 2 microscope with 5X magnification without any filters, light intensity 5 and an I/H condenser (Fig 4.3b). In addition, the same images were obtained in which the structure was perfused with a 1:1 mix of the two food dyes (Fig 4.3c). An overview of the mixing set up is shown in Appendix D.1.

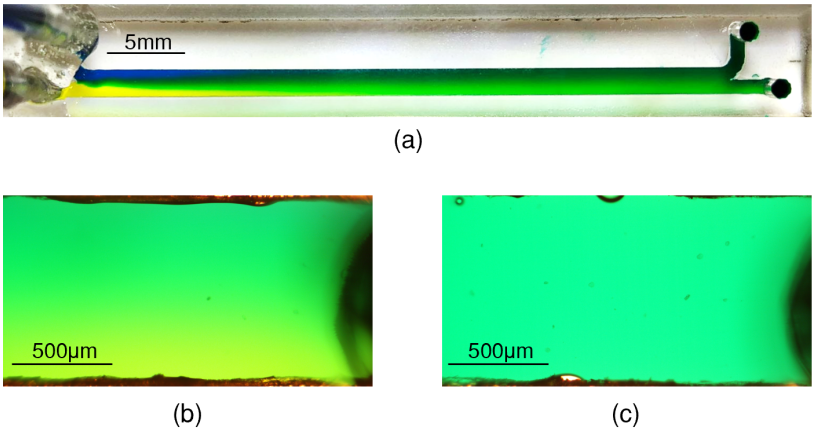

Figure 4.3: Validation example with food dye mixing. (a) 2mm wide straight channel structure perfused with a blue and a yellow food dye. (b) 5X magnified microscopic image of bottom outlet after 2 hours of perfusion with a blue colored food dye in inlet 1 and a yellow colored food dye in inlet 2. (c) 5X magnified microscopic image of bottom outlet after perfusion with a 1:1 mixed liquid of the blue and yellow colored food dyes.

A script was written in Python 3.7 that takes an image as input and analyses the red, green and blue (RGB) from pixels within two specified locations on the image. The script first analyses the RGB values of the pixels from the image in which the two separate colors were perfused for two hours. Then, the RGB values of the pixels within the same locations are analyzed from the image in which the structure was perfused by a 1:1 mixed liquid. Figure 4.4 illustrates this principle and shows a scatter plot visualizing the difference in RGB values of the two images for every pixel. Next, the Euclidean distance was calculated between the RGB values of the pixels from the first image and the RGB values of the pixels from the second image. The Euclidean distance was then normalized over the Euclidean distance between the RBG values of a completely mixed liquid with a completely unmixed liquid. To express the value in terms of mixing index, this ratio was subtracted from 1 and multiplied by 100%. Equation 4.8 shows the complete calculation of the mixing percentage.

[1] https://www.wardsci.com/store/

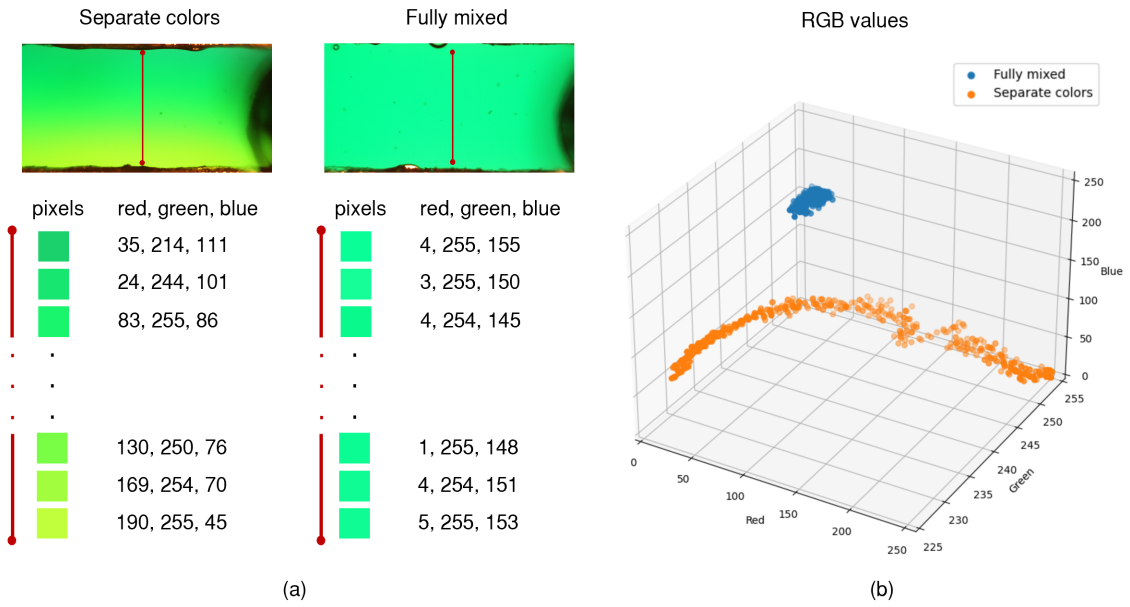

Figure 4.4: Example of pixel analysis. (a) All pixels on a line between two manually determined locations on the image are analyzed for their RGB values. (b) Visualization of difference in RGB values of the pixels in the two outlets.

$$m = \left(1 - \frac{\sqrt{(R_s - R_m)^2 + (G_s - G_m)^2 + (B_s - B_m)^2}}{\sqrt{(R_u - R_m)^2 + (G_u - G_m)^2 + (B_u - B_m)^2}}\right) \cdot 100\% \tag{4.8}$$

Where

R_s, G_s, B_s = RGB values of the image with two separate colors as input flows
R_m, G_m, B_m = RGB values of image with 1:1 mixed color as input flows
R_u, G_u, B_u = RGB values of an unmixed flow
m = Percentage of relative mixing

4.4. Results

The results of the simulations described in Section 4.2 are displayed in Tab. 4.1 showing the average mixing index across the outlet channel and the increase or decrease of the mixing index compared to the control structure (straight with a width of 2mm). The obstacle geometry and the 1mm width geometry show the biggest increase of mixing index with 15.3% and 16.3% respectively. The geometry with 9 sharp turns performs worst with a decrease in mixing index of 9.2%.

Table 4.1: Results of COMSOL mixing simulations showing mixing index and difference in mixing index with control structure.

Structure	**Mixing index (%)**	**Increase/decrease (%)**
Straight channel 2mm width (control)	45.9	-
Obstacles	61.2	+15.3
1mm width	62.2	+16.3
3mm width	40.4	-5.5
5 sharp turns	42.2	-3.7
9 sharp turns	36.7	-9.2
2π curvature, 2 turns	46.4	+0.5
2π curvature, 4 turns	47.5	+1.6
2π curvature, 8 turns	47.4	+1.6
4π curvature, 2 turns	48.0	+2.1
4π curvature, 4 turns	47.5	+1.6
8π curvature, 2 turns	48.4	+2.5
1π curvature, 16 turns	41.9	-4.0

Due to limited time, only five geometries were chosen to validate the simulations. The lack of effect on the mixing efficiency by an increasing number of turns and the positive effect of the decreasing channel width were deemed most interesting, which is why these geometries were used in the validation experiments. Fig. 4.5 shows the images taken from the outlet channels and Fig. 4.6 shows the mixing index across the outlet channel of the structures for both the COMSOL simulations and the experimental validations. In terms of the channel width geometries, it shows similar mixing profiles for the 2mm and 3mm geometries and an overall higher mixing in the thinner 1mm geometry. For the curved channels, all three mixing profiles are similar. Both phenomena are supported by the experimental data.

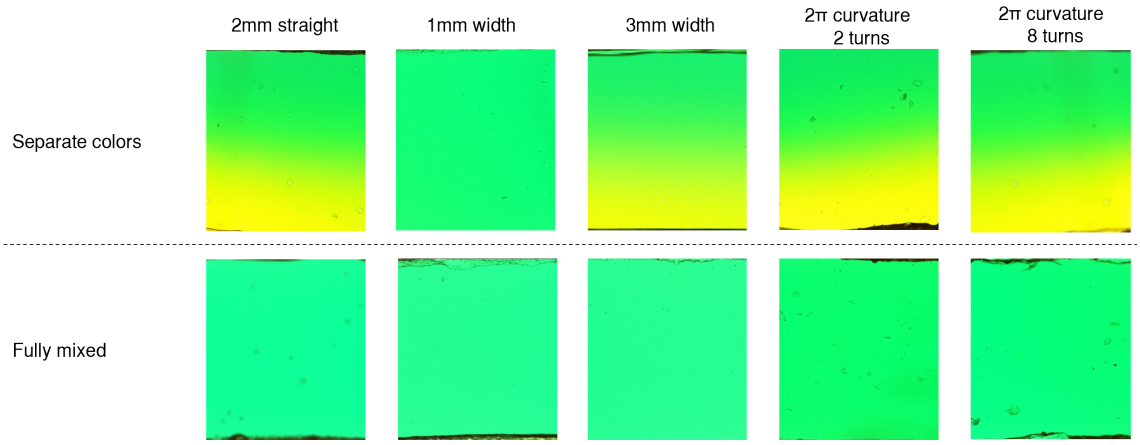

Figure 4.5: Images obtained for validation experiment. The Zeiss Axioplan 2 microscope with 5X magnification was used to image the outlet channel of the five different geometries. The top row shows the images taken after the geometry was perfused for 2 hours with a blue colored flow going into inlet 1 and a yellow colored flow going into inlet 2. The bottom row shows the images taken after the geometry was perfused with a fluid that consisted of a 1:1 mix of both colors.

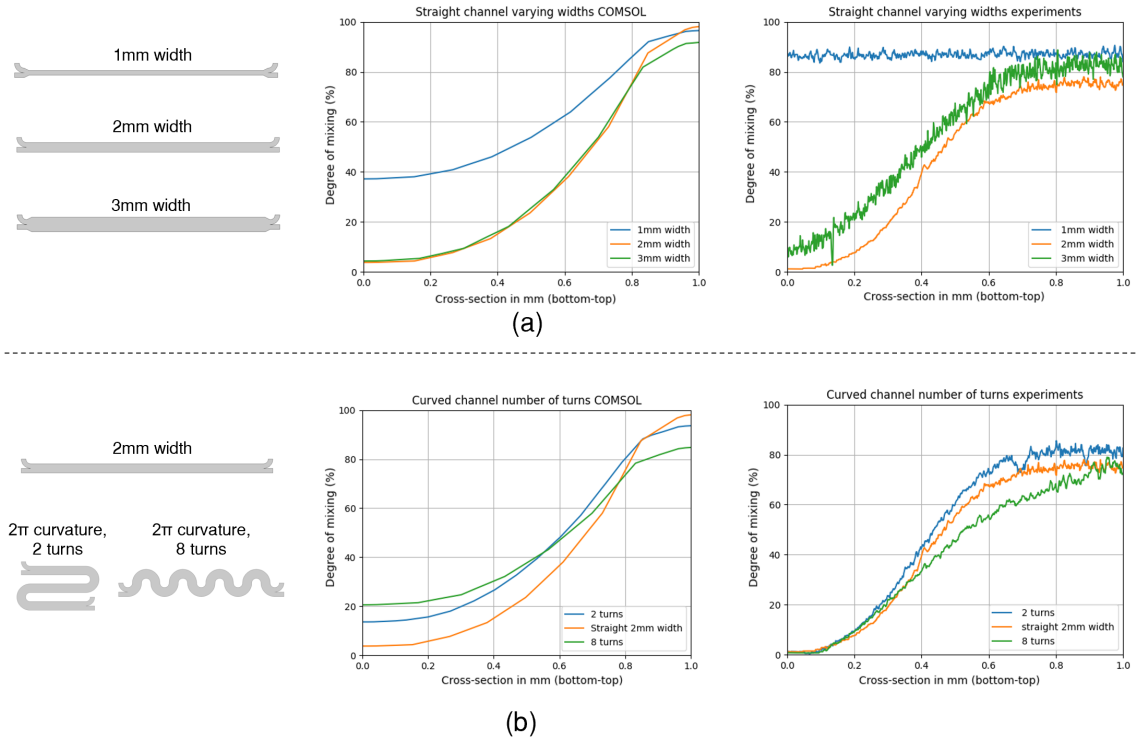

Figure 4.6: Comparison between COMSOL simulations and experiments. The left images show the geometries tested, the middle images show the simulation results and the right images show the experimental results. (a) Mixing results for straight structures with varying widths. (b) Mixing results of experiments with structures that have a varying number of curves with the same radius.

These results suggest that only geometries with obstacles or with a decreased width have a positive effect on the mixing efficiency. A serpentine geometry was chosen for the final proposed geometry shown in Fig. 4.7. The reason why this geometry was preferred over the obstacle geometry is further discussed in Chapter 6. This mixing geometry with a length of 60mm and a width of 1mm allows for a mixing index of 94.2% with a diffusion coefficient of $5.85 \cdot 10^{-10}$ $\frac{m^2}{s}$, which is the lowest diffusion rate found for organic compounds [148]. A CAD model of the SEBS layer with the proposed final mixing structure incorporated is shown in Appendix C.3.

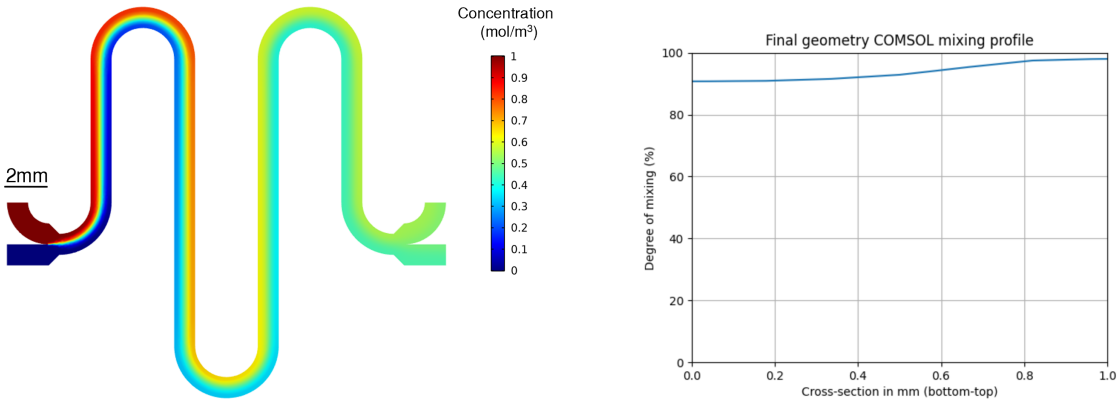

Figure 4.7: Final mixing geometry and its performance performance. (a) The concentration simulation shows that the geometry mixes the two flows to the equilibrium concentration of 0.5 mol/L. (b) A mixing profile of the bottom outflow channel.

4.5. Summary

By performing an analysis of the specific flow environment inside of the microfluidic channels, running numerical simulations and validating the results experimentally, it was attempted to optimize mixing performance in the shortest channel length. In this Chapter, it was found that with the used channel dimensions and flow rates the mixing performance was mainly dominated by diffusion. Therefore, diffusion distance and time are the dominant variables. The main constraint was that the mixer should be able to fit inside the space reserved on the microfluidic component. It resulted in the mixing geometry seen in Fig. 4.7. The structure has a low number of turns to keep the flow resistance as low as possible and a total length of 60mm which was deemed sufficient for a mixing of 94.2% for organic compounds with a low diffusion rate. Additionally, the high simplicity of the geometry makes it appealing for fabrication with the laser cutter.

Although the mixing component is easy to fabricate and integrate into the system, it was not included into the design that was used for the experiments in the next Chapter. The reason for this is the fact that the flow needs to be split after mixing to get rid of the excess liquid to make sure the flow rate remains 60μL/h in the second chip. This would require an additional pump actively removing the excess liquid. Due to limited time at the Wyss Institute it was decided not to include this redesign for the experiments of Chapter 5.

5

Cell experiments

With the knowledge and insights from the previous chapters, the next step is to put the system to the test. Two experiments are described in this section that involve tissue culture with the aim to prove the bio-compatibility of the system and to substantiate the importance of both the linking and of the added sensors.

5.1. Experiment 1: Bio-compatibility

In order to determine how the system reacts to the incubator environment for an extended period of time, a validation experiment was performed using cervical fibroblasts. For this experiment, conventional Emulate chips were used of which only the apical channel was seeded. The microfluidic component of the system comprised of layers of PMMA and PSA, connecting the apical channels of both chips.

Cell culture

Medium for the fibroblasts was prepared with 90% Dulbecco's modified eagle serum (DMEM) , 9% fetal bovine serum (FBS) and 1% pen-strep.The fibroblasts were thawed in a 37°C waterbath, transferred to a 15ml conical tube and centrifuged at 100G for 5 minutes. Excess Dymethyl Sulfoxide (DMSO) was removed and the remaining cells were dispersed in 10ml fresh medium before being transferred to a T-75 flask and left in an incubator overnight.

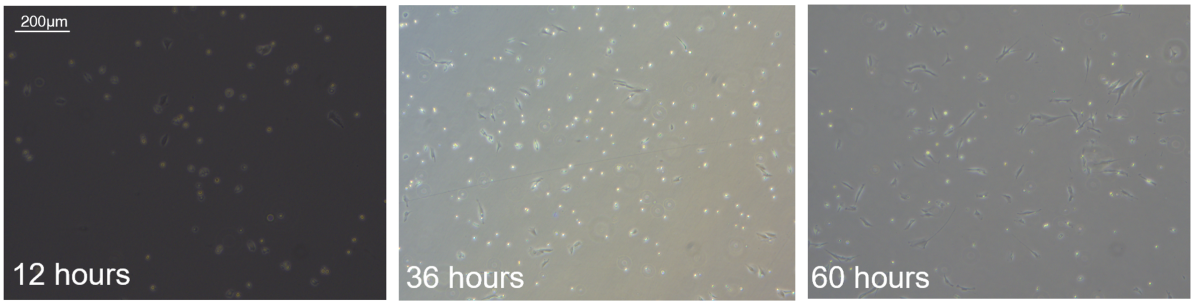

Figure 5.1: Fibroblast development after 12, 36 and 60 hours in a 37°C incubator.

Chip activation

In order to activate the channels, two emulate chips were placed in a tissue culture dish and desiccated for 30 minutes. An Emulate Reagent 1 (ER-1) powder and was diluted with 10ml of Emulate Reagent 2 (ER-2) in an 15ml conical tube. 20μl and 50μl of the solution was added to the apical and basal channels respectively. The chips were then transferred to a UV box and illuminated for 10 minutes for activation. The solution was

then aspirated from both channels, new solution was added to the channels and put back in the UV box for 5 minutes, after which the channels were aspirated, washed with 200μl ER-2 solution and 200μl sterile cold Dulbecco's phosphate-buffered saline (DPBS) . To coat the channels, a collagen I, Fibronectin and DPBS solution was used in a 20:3:77 ratio respectively. The coating solution was added to the channels and and the chips were incubated at 37°C for 2 hours to allow for polymerization. After incubation, the channels were washed with 200μl warm fibroblast media twice while excess media present on the surface was aspirated, leaving excess medium covering the inlet and the outlets until the chips were seeded with cells.

Chip seeding

To extract the cultured cells from the T-75 flask, the medium was aspirated and the cells were washed with 8ml DPBS before 2ml trypsin was added to detach the cells from the T-75 flask interior. After being incubated for 5 minutes, the trypsin solution was diluted with medium and transported to a 15ml conical tube which was centrifuged for 5 minutes at 100G. Excess medium got aspirated, 1ml of fresh medium was added and cells were counted to be at a 1.1x10^6/ml concentration. Cells were then loaded into the apical channels, as it can be observed in Fig. 5.2. The seeded chips were moved to a 37°C incubator overnight to allow for membrane binding and cell proliferation.

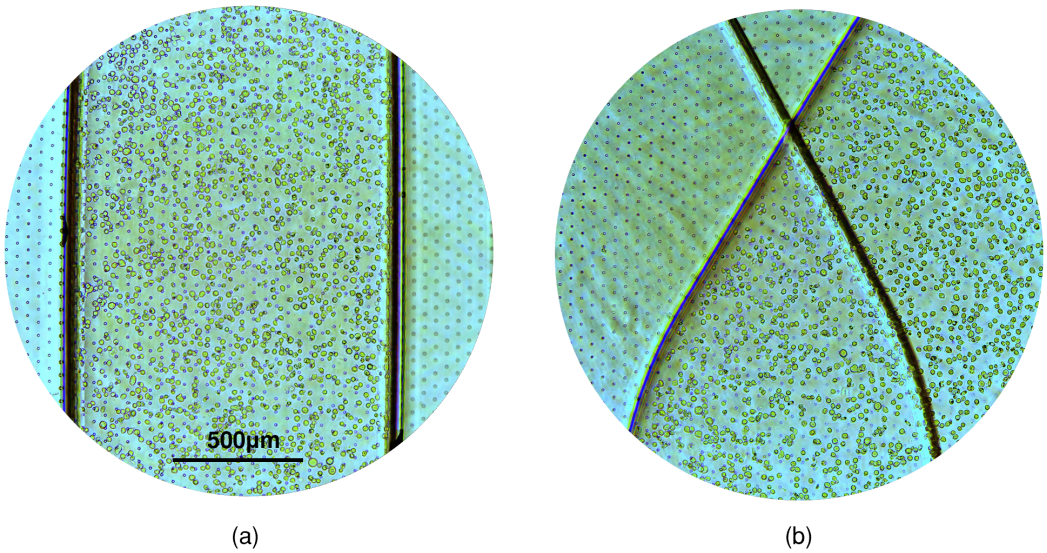

Figure 5.2: Seeded chip channels. (a) Middle of the apical channel seeded with fibroblasts. (b) Seeded apical channel with empty basal channel at bifurication.

System loading

The surfaces of all components of the system were washed with 70% ethanol. Parts that could not properly be cleaned with ethanol were sterilized using the Diener plasma sterilizer. After everything was sterile, the system was transported to the TC hood. Chips were taken out of the incubator, moved to the TC hood and both channels were washed with 100μl of fibroblast medium. After washing the channels a small droplet of fibroblast medium was left on both outlets and inlets and both chips are placed into the chips holder. To prepare the microfluidic components of the system for connection with the chips, the part was placed on the raised plateau and all pumps were set at 30μl/min to perfuse fibroblast medium through all inlet channels in order to reduce the formation of bubbles when the chips and the microfluidics are joined. When all inlet channels are filled and bubble free, the pumps were stopped leaving a small droplet at the end of the inlet channels. Then, the microfluidic part was moved up to swap the raised plateau with the chips that are secured in place by the chip holder. The microfluidic component was guided by the M4 screws while it was being lowered down to the point it makes contact with the chips. At this point, the connection was secured by screwing down the M4 nuts on the parts of the screws that stick out. To prepare the system for the incubator, the input reservoirs were filled completely to 4ml each. A complete setup of the system is shown in Fig. 5.3

Cell fixation

The chips were extracted from the system and each channel was washed with 200μl DPBS. As solution of 4% paraformaldehyde (PFA) in DPBS was made and added to the channels after which the cells were incubated at room temperature for 20 minutes. The channels were then washed with DPBS and stored in DPBS at 4°C.

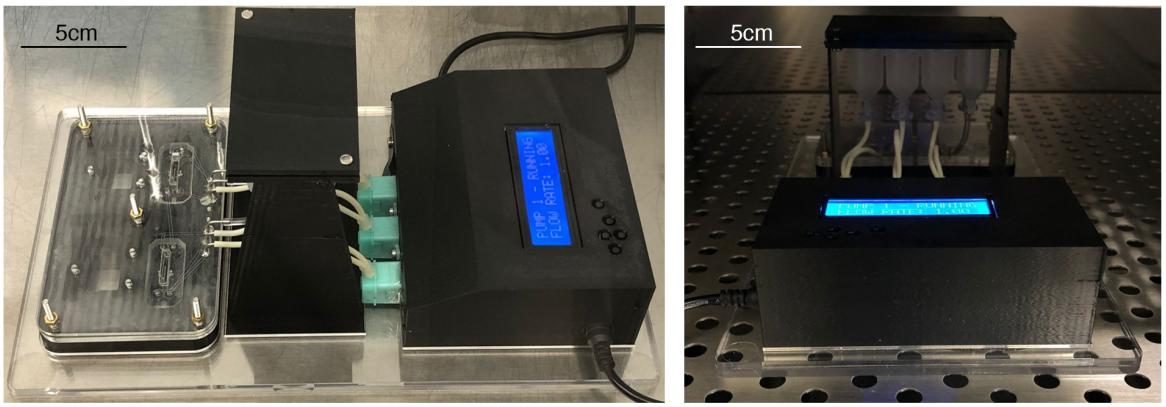

Figure 5.3: Complete setup for emulate chips. (a) Complete setup for Emulate chips loaded with fibroblasts. (b) Complete setup in incubator from user point of view.

5.1.1. Results

The results of the cell experiment using the fibroblasts are shown in Fig. 5.4. It shows the fibroblasts on both chips over 10 days of the experiment.

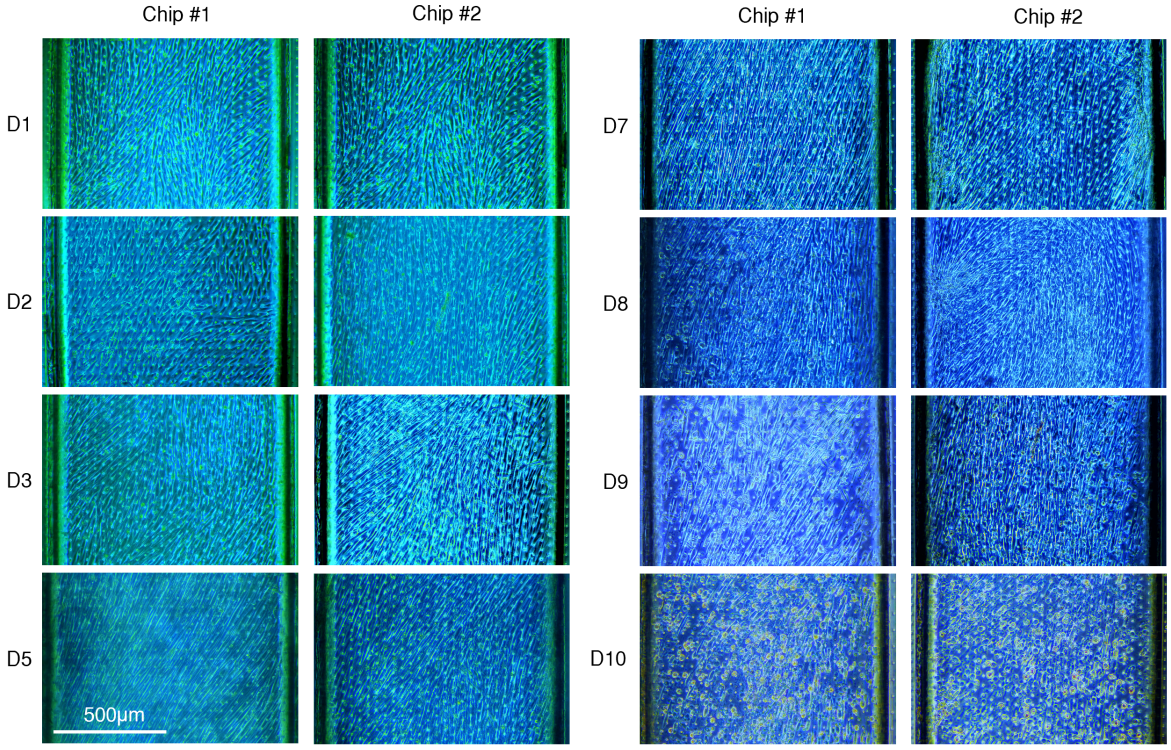

Figure 5.4: 10 day culture of Fibroblasts in separate chips with an apical connection inside the developed system.

After five days of incubation and perfusion, inside of the PSA layer in the microfluidic component branch-like structures started to appear starting from the channels moving inward (Fig. 5.5a). Also bubbles started

to form in the channels and imbalance of effluent volume between the different outflow reservoirs appeared. The apical outflow reservoir held about 75% less volume after 24 hours of perfusion than the basal outflow reservoir of chip #1 (Fig. 5.5b). In addition, location specific cell death was observed on chip #1. Fibroblasts located on the first part of the channel seemed less confluent compared to cell on the second half (Fig. 5.5c).

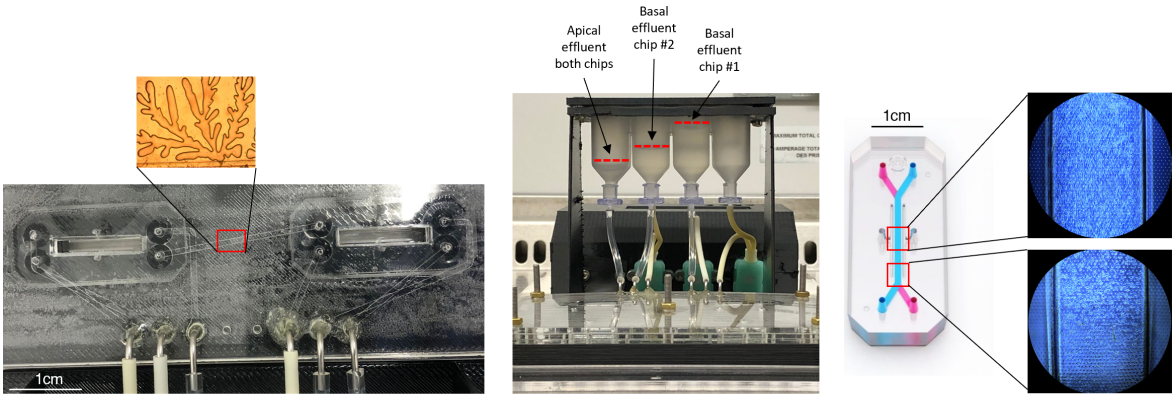

Figure 5.5: Issues with system. (a) After 5 days in the incubator, bubble formation inside of the channels appeared as well as branch-like structures in the PSA layer of the microfluidics component. (b) A difference in effluent volume between the reservoirs. (c) Location specific fibroblast death inside of the Emulate chips.

5.2. Experiment 2: sensor and linking functionality validation

The aim of the second experiment was to prove sensor functionality and test the barrier integrity of the cells. In this experiment, HUVECs were grown in the basal channel of the chips and Caco-2 cells were grown in the apical channels. Fluorescent labeled dextran is added to the basal reservoir for chip #1 and perfused for several hours to make sure the particles have time to travel from the input reservoir to the output reservoir. During this time, the fluorescence can be measured in all of the output reservoir to determine the ratio of particles that traveled along the basal channel, or crossed the cell barrier over to the apical channel. Also, TEER measurements are performed to keep track of the barrier integrity.

At a later point in time ethylene glycol-bis(β-aminoethyl ether)-N,N,N',N'-tetraacetic acid was added to the basal reservoir of chip #1. EGTA is known for its disruptive effect on tissue barriers [149]. From this moment, fluorescence measurement, TEER- and O_2 measurements are performed. It is hypothesized that in the first hours the barrier resistance measured by the TEER sensors in chip #1 will decrease, while the barrier resistance in chip #2 is unaffected. Also the O_2 values are expected to remain constant for both chips and the fluorescent values in the output reservoirs for chip #1 should increase while the fluorescence in the output reservoirs of chip #2 should be zero.

After 3 hours, when the liquid from the apical channel has been fully run through with fresh liquid, it is expected that the barrier resistance also drops in chip #2 and that fluorescence levels in the output reservoirs for chip #2 also show an increase. Observing these phenomena would imply that the added EGTA distributed the barrier function of the Caco-2 cells and HUVECs allowing the fluorescent labeled dextran and excess EGTA particles to pass over to the apical channel. The particles then continue through the connecting channel over to chip #2 where the EGTA again causes a barrier function decrease and allowing particles to pass over to the basal channel. A schematic overview of these different processes are shown in Fig. 5.6.

Cell culture

The Caco-2 cells and the HUVECs were cultured 10 days in a T-75 flask before they were transferred to the sensor chips. General protocols for these cell lines were used during in this stage [150][151]. A cluster of Caco-2 cells after 10 days of culture in a T-75 flask can be observed in Fig. 5.7a.

Chip activation

The same parameters for the fibroblasts were also used for the Caco-2 cells and HUVECs as is explained in the previous section. The only difference was that the Caco-2 medium was used for the apical channel and HUVEC medium for the basal channel. Caco-2 medium consists of DMEM with 10% fetal bovine serum, 1% non-essential amino acids (NEAA), 50 μM thioglycerol and 25mg/ml gentamycin. The medium for HUVECs consists of DMEM with 5% FBS.

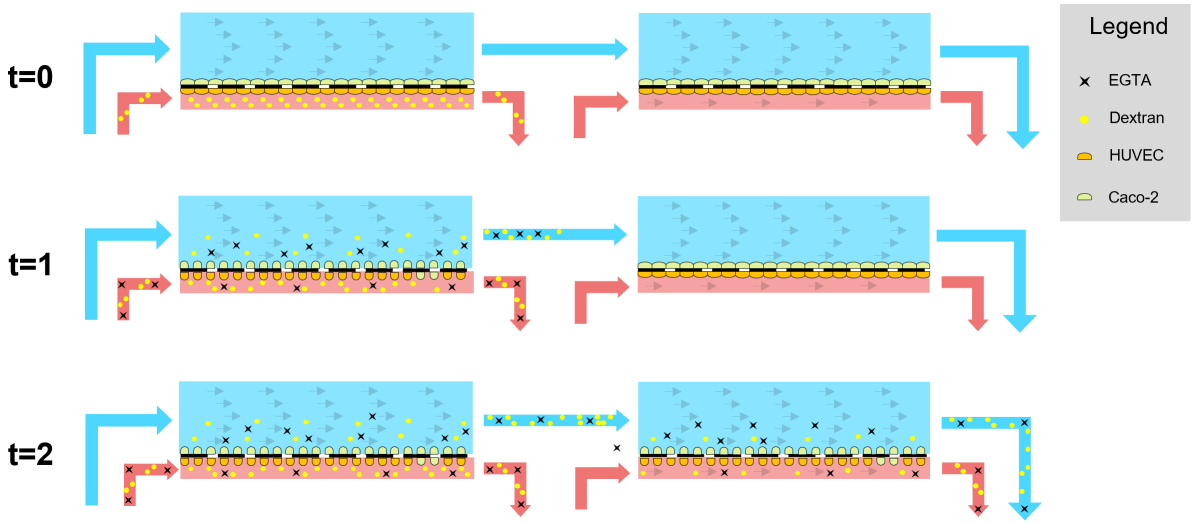

Figure 5.6: Experiment 2 set up. At t=0 only the basal input reservoir of chip #1 has fluorescent dextran which is only detectable in the basal output reservoir of chip #1 because the cell barriers are intact. At t=1 EGTA is added disrupting the barrier function and allowing for particles to pass over to the apical channel of chip #1. At t=2 the particles have had enough time to flow all the way over to chip #2 where the EGTA also disrupts the barrier integrity and allows particles to disperse over to the basal channel of chip #2.

Chip seeding

The procedure for loading the Caco-2 cells and the HUVECs into the channels of the sensor chips is similar to the fibroblast procedure in the previous section. However, because in this experiment both channels need to be seeded, an additional step was necessary. After the 2 hour incubation of the Caco-2 cells inside the apical channel, the HUVECs are seeded into the basal channel. The chips are then placed back inside the incubator upside down. This allows gravity to sink the cells onto the membrane which will eventually make them adhere. Fig. 5.7b and Fig. 5.7c show the Caco-2 cells and the HUVECs after seeding inside of the apical channel and the basal channel of the sensor chip respectively.

Figure 5.7: Experiment 2 cells in culture. (a) Clump of Caco-2 cells inside a T-75 flask.(b) Caco-2 cells in apical channel of the chip after seeding. (c) HUVECs inside the basal channel of the chip after seeding.

Static in-chip cell culture

After seeding the cells into the channels of the sensor chip, the cells were grown for 10 more days before the sensors chips would be placed inside of the linking system. During these 10 days the cells would be cultured in static conditions (Fig. 5.8). The basal channel was provided with 200μl of fresh HUVEC medium and the apical channel was provided with 200μl fresh Caco-2 medium every 24 hours.

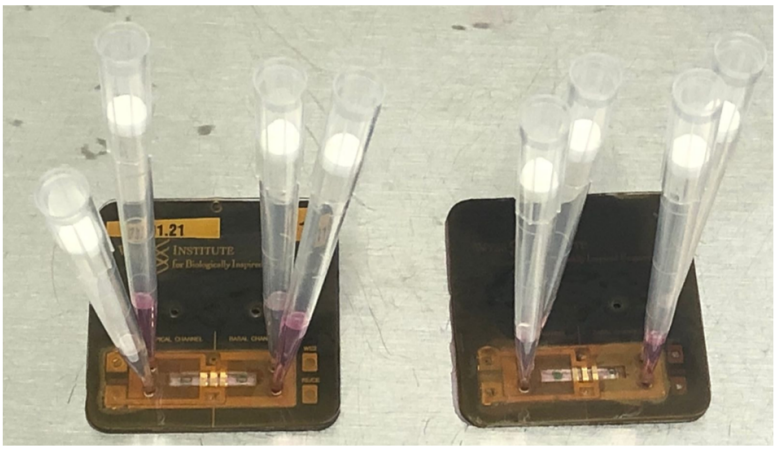

Figure 5.8: Static HUVEC and Caco-2 culture in sensor chips. Medium was refreshed every 24 hours and pipette tips were left in to prevent the channels from drying up overnight.

5.2.1. Results

After 10 days of static culture of the Caco-2 cells and HUVECs inside of the sensor chips cell death occurred (Fig. 5.9). Possible explanations for this event is explained in the next Chapter. The experiment could neither be continued nor started again due to limit time at the Wyss Institute.

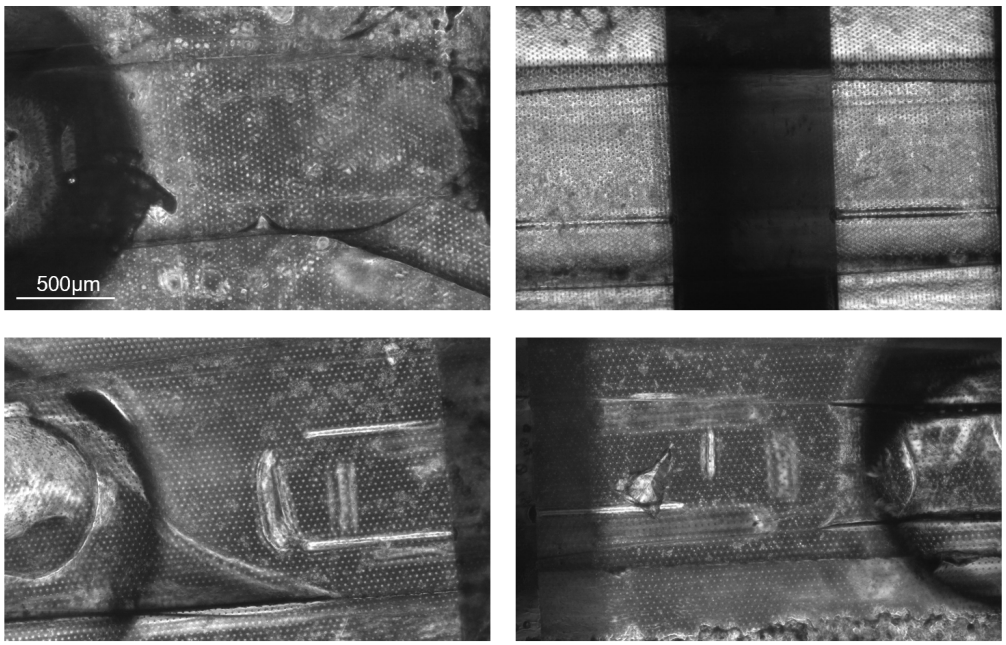

Figure 5.9: Cell death occurred in the first 10 days of culturing the cells inside both sensor chip #1 (top left and bottom left) and sensor chip #2 (top right and bottom right).

5.3. Summary

This Chapter tried to prove the functionality of the final design and substantiate the added value of the linking and the integrated sensors. The first experiment showed the biocompatibility of the system by demonstrating fibroblast growth in the first five days of culture. The second experiment aimed to link two gut models together and validate its barrier function using sensors and fluorescently labeled dextran. A manufacturing error made it necessary to culture the cells inside of the sensor chips in a static environment. During the final phase of the sensor chip fabrication process, the top layer of 1mm PDMS did not fully adhere to the thermal adhesive layer. This issue had occurred in previous batches as well and caused leaking in the long-term between these two layers. It was decided that the cells could be cultured statically inside the sensor chips, before loading them into the linking system. This would reduce the amount of time that the cells are under flow, but also decreases the possibility of any leaking occurring. Cell death occurred during this phase and the experiment could not be conducted. The next Chapter tries to elaborate on this issue and discusses other matters including the design and the simulations.

6

Discussion

In this part the results from the previous Chapters are interpreted, their significance is discussed, and suggestions for future research are presented.

6.1. Design

The final design shown in Chapter 3 has partly proven its functionality during the tissue culture experiments described in Chapter 5. Although it satisfies the most important requirements (e.g. compactness, biocompatibility, inexpensiveness etc.), certain aspects could be adjusted to improve its functionality and usability.

- The biggest improvement would be to replace the way the microfluidic component is connected to the chips. In the current design, this is done with five screws and nuts pressing down on the microfluidic components creating a seal. 400μm thick PDMS rings are added around the ports to account for any variability. Although this provides a sufficient connection, it is not user friendly. Screwing down the nuts on the screws in a tissue hood while wearing gloves, all the while keeping the components aligned, can be challenging. A structure that can be clamped down with one movement would significantly improve this step.

- The second design suggestion would include a single connector from the reservoirs to the microfluidic component. In the current design this link consists of eight separate connections which require the use of epoxy glue to attach steel rods to the microfluidic component. This step in the fabrication is time consuming and prone to errors. When the epoxy is not viscous enough, it can seep into the channels causing a blockage. The set epoxy is also prone to detaching from the PMMA which causes leakage. By designing a component that accounts for these issues, the fabrication process would become significantly faster and reliable. Additionally, this would decrease the channel length since the tubing going from the reservoir to the microfluidic component currently accounts for 29.2% of the total distance of the longest path.

- To improve the compactness of the system, a redesigned control unit for the pumps that is reduced in size would greatly impact on the total size of the system since that component accounts for 40% of its overall size. The current control unit has been built for functionality using a Raspberry Pi 4 microcontroller, but plenty of smaller alternatives exist.

- Another design change would be to add internal sensor components into the base to make the system truly autonomous. Using the system as its present form, an external laptop and potentiostat needs to be connected in order to do TEER readings and the chip and reservoir holder need to be detached to complete the O_2 measurements. This makes doing measurements time consuming and exposes the system to an outside environment, increasing the risk for contamination. Small sensor components like potentiostats and optical O_2 sensors are commercially available [1] and would make the system more complete overall.

[1] Companies like Metrohm (https://www.metrohm.com/) and Pyroscience (https://www.pyroscience.com/) offer such components.

- The final major change in design would be to include the mixing geometry that is discussed in Chapter 4. Not only would this mean changing the basal SEBS layer (as proposed in Appendix C.3), but also adding a fifth pump that extracts excess fluid from the flow that continues on to the second chip. This would make sure the second chip receives the same flow rate as the first chip. Additionally, the current peristaltic pumps were observed to deliver short bursts of motion which could potentially influence the fluid flow and therefore the cell behavior. Ideally the next design uses pumps that induce a more constant flow.

Besides these main design changes, it is also recommended to future researchers at the Wyss Institute to not use the Epilog Legend 36EXT laser cutter for fabrication of the microfluidic component. This laser cutter uses different versions of software, some of which are not compatible anymore, and causes inconsistencies in the locations of the cut outs. Appendix C.4 shows an example of these inconsistencies. This issue caused a significant time delay and has not yet been resolved. The biosensors group has acquired a new laser cutter because of this issue and it is recommended to use this machine for fabrication.
And finally it is also recommended that future researchers experiment with thicker layers of SEBS (100μm - 200μm). Bigger thicknesses reduce the likelihood of bubble formation and make the material easier to work with.

6.2. Mixing study

The main takeaway of the mixing study was that the flow rate and the specific channel dimensions causes the flow to have a very low Reynolds number, implying that the mixing coefficient is mainly diffusion dominated and that convection has little effect. The simulations supported this finding and in turn the experiments supported the simulations. We saw that adding obstacles or decreasing the channel width had the biggest positive effects on the mixing index and that adding curved turns has little effect. Both of these findings are in line the fact that the mixing is diffusion dominated and that the driving parameter is diffusion distance. Adding sharp turns or increasing the channel width has a negative effect on the mixing index. This seems counter intuitive as these geometries should not affect the diffusion distance. However, certain dead-zones are present in the sharp turns which increase the diffusion distance temporarily (See Appendix D.2 for more information). This would explain the decreasing mixing coefficient with a increasing number of sharp turns
The final mixing geometry consisting of a serpentine structure with a width of 1mm and a length of 60mm was chosen because it fit within the reserved area on the microfluidic component and showed sufficient mixing for compounds with a low diffusion coefficient (Fig. 4.6). Moreover, this geometry is compatible for fabrication with the laser cutter. Although this study offered some valid insights into the best mixing geometry, several things can be improved in order to substantiate these findings even more.

First and foremost, every geometry was only validated experimentally once, therefore the experimental results may only serve as a hint and not as evidence. It should also be noted that it was a challenge to get consistent images from the outflow channels. In order for the script to analyze the pixel's RGB values, objects should have consistent lighting when images are taken. Because of the differences in geometry and the transparency of the PMMA, some images would contain shadows or have an inconsistent brightness. This could be a reason for the large difference in mixing performance between the simulations and experiments of the 1mm wide channel (Fig. 4.6a). Additionally, due to the time constraint, the final geometry was never tested experimentally which is recommended to make sure the mixing is as efficient as the simulations imply.

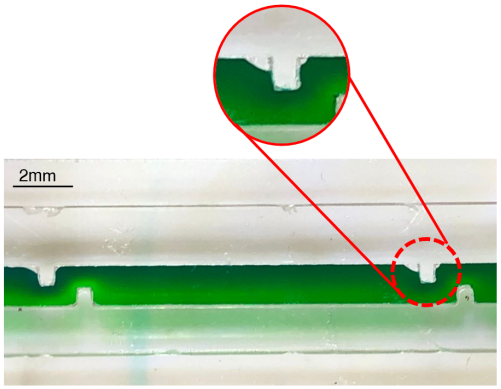

Figure 6.1: Bubbles trapped in obstacle geometry. The sharp corners of the obstacles make it easy for bubbles to get stuck.

It is also interesting to note why the obstacles were not included in the final geometry despite their positive effect on the mixing index. Two main reasons lie at the base of this decision. First, adding these smaller structures would make fabrication of the SEBS material significantly harder. Second, during tests it was observed that bubbles are prone to become trapped at the edges of these structures (Fig. 6.1).

6.3. Cell experiments

The cell experiments served as a proof of concept of the linking system. It showed that cells can survive for up to five days and that the system is capable of providing a consistent flow. From Fig. 5.4 it can be observed that the cell shape becomes thinner as space runs out and how the confluency of the fibroblasts increases until day 7, growing from a single monolayer to multiple layers. There is also a slight change in orientation of the cells, showing to be more in line with the flow direction as time progresses. On day 8 the confluency decreases dramatically and on day 10 some of the remaining dead cells are clearly visible. This event can be traced back to the flow not passing through the apical channel as shown in Fig. 5.5b. This image also shows that the fluid intended for the apical channel must have traveled through the membrane to the basal channel of the first chip, since this reservoir contained twice as much medium after 48 hours than normal. A plausible explanation for this could be air obstructing the passage of the flow through the channel that linked the two apical channels. In Fig. 5.5a it is shown how the PSA released air that was trapped within the PSA and the PMMA into the channels and bubbles started to form. A visual schematic of this explanation is shown in Figure 6.2. This description could also explain the location specific cell death shown in Fig. 5.5c that was observed on day 5. The absence of bubble formation and thicker cell layers on both sides of the membrane could prevent this phenomenon from occurring in future experiments. This is why the second experiment was designed to have a SEBS layer in stead of PSA and to have cells in both channels.

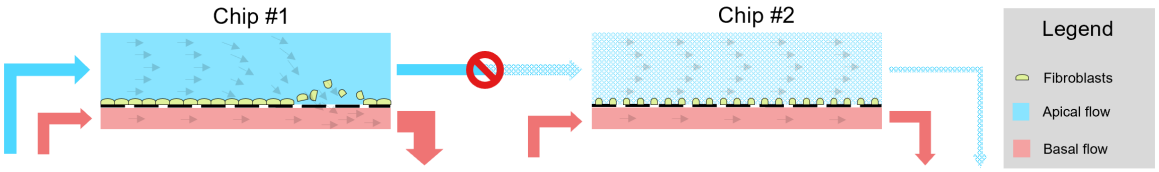

Figure 6.2: Visual representation of flow rerouting. A blockage in the apical linking channel caused by bubbles could have induced location specific cell death.

The second experiment aimed to show sensor and linking functionality. Due to a fabrication inaccuracy, the layer of 1mm PDMS on top of the sensor chip did not adhere correctly. This layer ensures a good seal between the chip and the microfluidic platform and any adherence issues of this layer to the chip will cause significant leaking. It was therefore decided to culture the Caco-2 cells and HUVECs inside of the sensor chips under static conditions. The channels were washed and provided with fresh medium every 24 hours and the pipette tips were left in the ports to prevent the channels from drying up, as shown in Fig. 5.8. An explanation for this event could be that the refresh frequency of once every 24 hours was not enough for to keep the Caco-2 cells and HUVECs alive. This, however, would be quaint since the pipette tips all contained about 400μl extra medium. Nutrients in the pipette tips could have reached the cells via diffusion. Another explanation could be that the cells themselves were damaged prior to the start of the experiment. Due to the big clumps shown in Fig. 5.7a the cells were subjected to trypsin for longer than usual, which is known to cause cell death. This could have impacted the cells even though they initially looked healthy after seeding.

7

Conclusion

The research goal of this thesis was to create an easy-to-fabricate and compact system for the set up of the Wyss Institute that could link a gut OoC model with a BBB OoC model that can keep track of O_2 levels and measure TEER values.

This thesis focused on using accessible and fast fabrication techniques to create the linking system and tried to partly prove its functionality via multiple days of cell culture. Additionally, it investigated the most efficient geometry to mix two fluid flows.

By using 3D printing and CO_2 laser cutting to fabricate main components, an inexpensive and easy to assemble platform was created that takes only a day from start to finish to build and is compact enough that several systems fit inside a single incubator. The whole assembly consists of a pump unit, a chip and reservoir holder, a microfluidic component and a base. The system uses 4 DC peristaltic pumps to perfuse the medium from the four input reservoirs, through the microfluidic component and the chips, to the output reservoirs. The detachable pump heads make it possible to detach the chip and reservoir holder and the microfluidic component from the base and pump unit to be used for imaging without introducing air into the channels.

The tissue culture experiment using fibroblasts made two things evident. Firstly, that the system was fully biocompatible. No contamination or cell death was found after 5 days of culture and medium outflow seemed normal. Second, that using PSA as a material from which the channels were cut was not sufficient. After five days of incubation, the PSA would detach from the PMMA and air would be introduced into the channels preventing the medium to flow through the channel freely. In order to resolve this issue, PSA was replaced with a SEBS polymer layer that showed sufficient binding to PMMA in additional experiments (Appendix C.2).

The second tissue culture experiment that was planned to prove sensor and linking functionality could not be conducted due to cell death that occurred in the 10 days prior to the experiment. Thus, full system functionality still needs validation.

Additionally, the project used COMSOL simulations and experimental data to find an efficient geometry for mixing two fluid flows. A serpentine geometry with a length of 60mm and a width of 1mm was deemed most convenient for mixing the two flows with diffusion being the main driver.

This research implies that the developed system can function as a foundation for a completely autonomous linking platform with integrated analytical components. It has partly proven its functionality, and both the mixing study and the tissue culture experiments provided important information for improvements that can be implemented into future iterations. It is advised that future researchers of the Wyss Institute focus on developing sensor components that can be added into the base of the system and to integrate the proposed mixing geometry.

A

Appendix - Fabrication and usage manual

Title: TEER-O2 sensor integrated chip linking system fabrication protocol	Author: Stijn (robbenstijn@gmail.com) +31628149709
TEER-O2 sensor integrated chip linking system fabrication protocol	Date: 08.02.21

Fabrication

Materials:

Before starting, make sure there following materials are in stock:

1. 4 DC peristaltic pumps from Tagasago with screw holes
2. 5 M2.5 screws and nuts
3. 1 pump control unit made by Hani Sallum
4. 5 minutes epoxy glue
5. Two rectangular spring-loaded connectors from Mc MasterCarr
6. One 25 DB-sub female connector from Mc MasterCarr
7. Standard wiring
8. 1.5mm PMMA
9. 100um SEBS or double-sided adhesive (preferably 150um)
10. 2 sets of 4 4.5ml fluid reservoirs from Chipshop
11. Standard tubing with 1mm inner diameter
12. Hollow steel rods with 0.5 inner diameter and 1mm outer diameter

3D printed components:

1. Reach out to Paul or John to get the Fortus 400 3D printer training.
2. Print the .STL files named "*Base", "Chip & reservoir holder"* and "*Pump housing".*
3. Print job will take up to 18 hours in total.

Microfluidic component:

1. Reach out to Paul or John to get the Laser cutter Epilog Legend 36EXT 75watts.
2. Cut out the .DXF files "*Bottom layer*", *"Middle layer"* and *"Top layer"* using the settings in the table below from a 1.5mm PMMA sheet

	Speed	Power	Frequency
1.5mm PMMA	20	60	5000
3mm PMMA	20	70	5000
PSA	100	20	2000
100μm SEBS	75	15	2000

3. Cut out the .DXF files *"Basal layer"* and *"Apical layer"* from the PSA or 100um SEBS material using the settings in table above.
4. Cut out 8 of the .DXF file *"Seal to chip"* from the PSA using the settings in the table above.
5. Clean the PMMA parts with IPA and place the bottom PMMA layer on a flat surface the face down that will be in contact with the chips.
6. Carefully remove the plastic from the basal PSA or SEBS material layer.
7. Slowly lower the exposed side of the PSA or SEBS layer on top of the PMMA part making sure that all the ports and cut outs are aligned.
8. Remove any trapped air with fingers in a rolling motion.
9. Remove the other plastic layer of the basal layer exposing the PSA or SEBS material on this side.
10. Repeat steps 7-9 for the middle PMMA layer, the apical layer and the top PMMA layer.

11. Place the complete assembly in a 85C oven with as much weight on top as possible overnight.
12. In the meantime, make a slab of 400um PDMS using the following protocol:
    a. Prepare PDMS (Ellsworth Adhesives #4019862) at a 10:1 ratio. Pour desired amount of PDMS base in a Thicky cup and add 1/10th of that mass of curing agent.
    b. Weigh PDMS + white Thicky cup holder (found in the Thicky mixer).
    c. Adjust the counterweight balance inside the Thinky Mixer with the appropriate weight.
    d. Place the holder with the cup of PDMS inside the mixer, ensuring that it is properly secured in the slot.
    e. Set the mixer to program 1 and press start.
    f. While PDMS is mixing, cut a 150mm x 150mm square sheet of clear, 1mm thick polycarbonate plastic (McMaster-Carr #85585K28). Remove the backing and clean with IPA and a cleanroom wipe.
    g. Place the PC sheet in the spin coater over the 4in size chuck and pour PDMS over the PC sheet. An appropriate amount of PDMS will cover the entire size of the chuck.
    h. Cycle through recipes by using (↑↓). Recipe 12 = 400um thick PDMS
    i. After selecting the recipe, press start and wait until spin coater displays the message “remove coated part”.
    j. Place the PDMS covered PC sheet on a cleanroom wipe and transfer to vacuum desiccator.
    k. Leave PDMS slab in the chamber for 2 minutes or until air bubbles are removed.
    l. Once degassed, move slab to 60C oven and let cure for at least 1 hour. PDMS slab may also be placed in 80C oven for 30 minutes.
    m. Use PET/PC film as a protective layer for storage and handling. Films can be found in large bin under middle bench (bench under desiccators).
    n. Cut film to size of PDMS slab, clean with IPA and a cleanroom wipe, and dry with compressed air.
13. Use the plot cutter to cut out the .DXF file “*Seal to chip*” 8 times from the PDMS slab using the CB15U-60 blade at 500um height, speed of 1, acceleration of 1, cut force of 23 and and offset of 0.
14. The next day, get the microfluidics component out of the oven and get the PSA and PDMS cutouts of the *“Seal to chip”* file.
15. Remove the plastic layer from the PSA cutout and place it around the ports of the bottom PMMA layer that will be in contact to the chips. Do this for all 8 cut outs.
16. Remove the second plastic layers of the PSA rings that are now attached to the PMMA part.
17. Place the total assembly into the plasma machine together with the PDMS rings cut-outs placed inside of a small plastic dish in such a way the the surfaces are exposed to the gass
18. Treat the surfaces with the “PMDS bonding” program.
19. Take the PDMS rings and PMMA-PSA assembly out of the plasma machine and attach the exposed PDMS surface to the PSA exposed surface and apply pressure with your fingers for about 10 seconds.
20. Use 5 minutes epoxy glue to attach the steel rods to the inlet ports on the top part of the PMMA layer, making sure the glue does not block the channel. It is best to wait 3 minutes after the glue has been mixed so that it is more viscous and can not seep into the channels.

Title: TEER-O2 sensor integrated chip linking system fabrication protocol	Author: Stijn (robbenstijn@gmail.com) +31628149709
TEER-O2 sensor integrated chip linking system fabrication protocol	Date: 08.02.21

Base fabrication:

1. Take the 3D printed base, 4 colors of wiring, 2 rectangular spring-loaded connectors and the DB-sub to the solder station
2. Cut the wiring to a sufficient length and strip away the plastic at the ends
3. Push the rectangular spring-loaded connectors through the rectangular openings in the base, making sure that the gold connectors are facing outwards and the four pins are facing towards the narrow part of the base.
4. Add a bit of flux fluid on the connector pins and solder the end of the wiring to the pins, add two heat shrink tubes on top of the wire and solder the other end to the correct DB-sub pins as

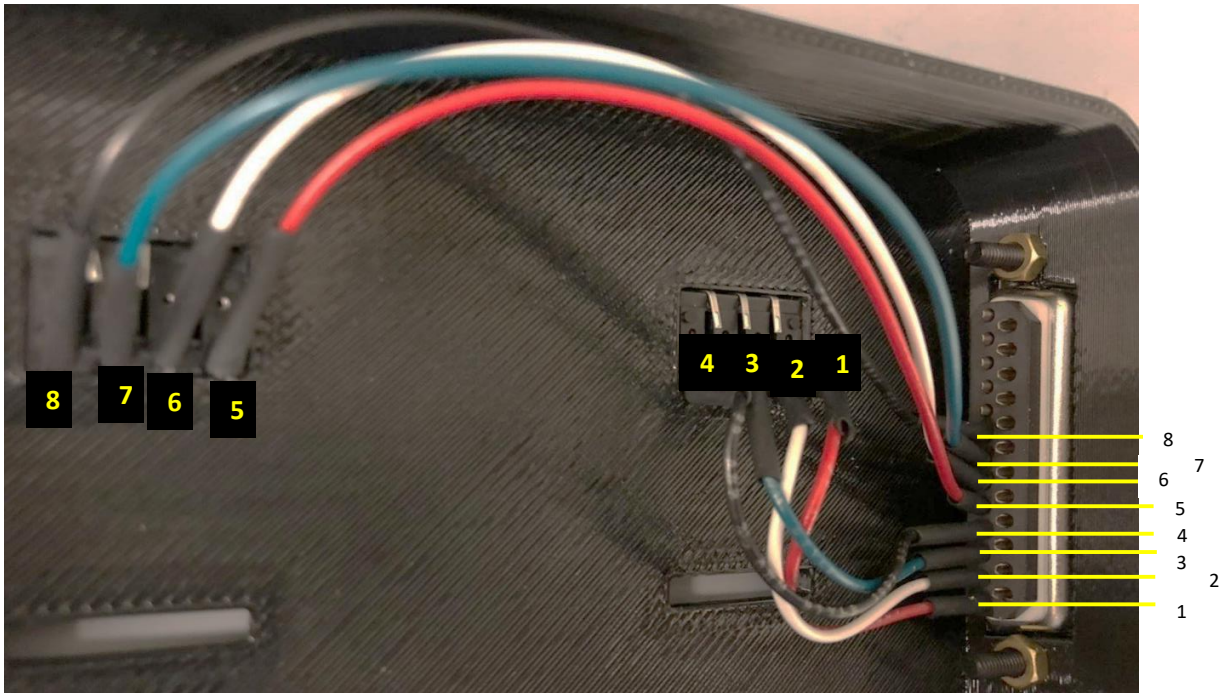

shown in the figure below.

5. Move the heat shrink rubbers over the soldered part and use the heat air blower to shrink them (make sure not to hold it too close otherwise the plastics of the wires will start to melt.)
6. Fix the DB-sub connector to the base with the two screws and nuts.

Chip & reservoir holder fabrication

1. Get the 5 M2.5 screws and move them through the screw holes from bottom to the top, exposing the wire side on the top.
2. Use 5 minutes epoxy glue to secure them in place.s

Pump unit fabrication

1. Solder the wiring in a consistent order to the pumps
2. Move the wires through the pump holes in the 3D housing so that the pump heads are positioned in the correct position.
3. Connect the other ends in a consistent order to the control unit by screwing down the connector screws.

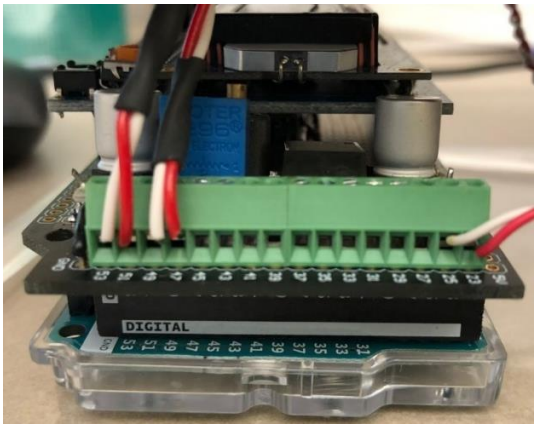

4. Use 8 M2 screws and nuts to attach the pumps to the 3D housing.

PMMA assembly holder

1. Laser cut the .DXF files *"Platform holder #1"* and *"Platform holder #2"* out of 1.5mm PMMA.
2. Use 5 minutes epoxy glue to attach #1 to #2

Assembly

1. Assemble everything to recreate the image below:

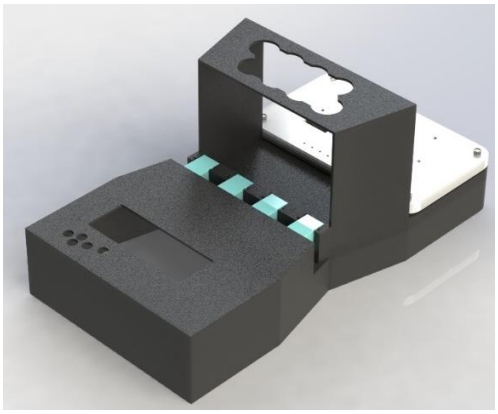

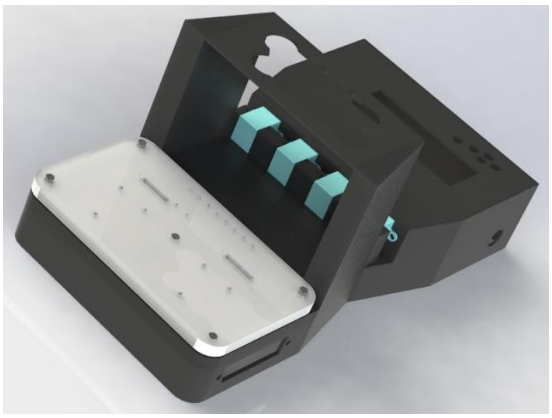

2. Connect the reservoirs, tubing and pump heads to recreate the images below
3.



Usage

1. In the TC hood, make sure the chips are seeded properly and on top of the inlets and outlets a small droplet of excess medium is present.
2. Use the prime holder to elevate the microfluidics component up a few cm's.
3. Run the perfusion speed at 30ul/min for about 5 minutes or stop when droplets have formed at the end of the channels.
4. Use buttons 1 and 3 to toggle between pumps (1-8)
5. Use buttons 2 and 4 to increase or decrease the flow rate (1-30ul/min)
6. Remove the prime holder and place the chips in the system while holding the microfluidics component up.
7. Slowly lower the microfluidics component onto the chips making sure the inlets and outlets of the microfluidics component align with the inlets and outlets of the chips.
8. Secure everything in place by screwing the nut down, starting with the one in the middle.

B

Appendix Design iterations

Figure B.1: First design iteration of linking system. The first design only includes the fluid reservoirs and the microfluidic component, not the pump unit. In this design, a custom PCB was used to fit the PDMS chips in and the microfluidic component would be placed on top of this. The fluid reservoirs were placed on top of the assembly to make everything as compact as possible.

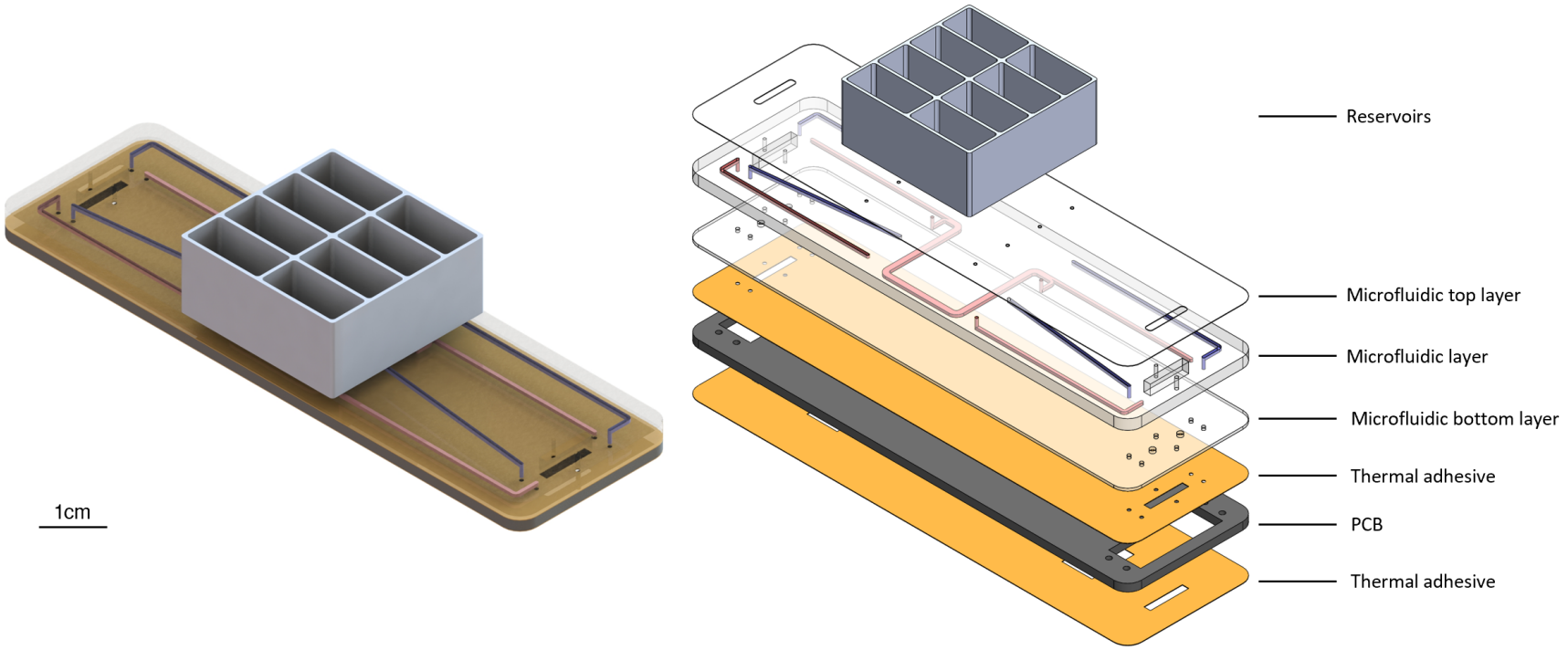

Figure B.2: Second design iteration of linking system. This design has a clustered reservoir unit compared to the first design and the chips are orientated outwards to leave more space for the mixing area.

Figure B.3: Third design iteration of linking system. This design does not rely on a custom made PCB anymore but used the conventional chip-PCB assembly. The chips are placed within a holder and the microfluidic layers and the reservoirs are added on top.

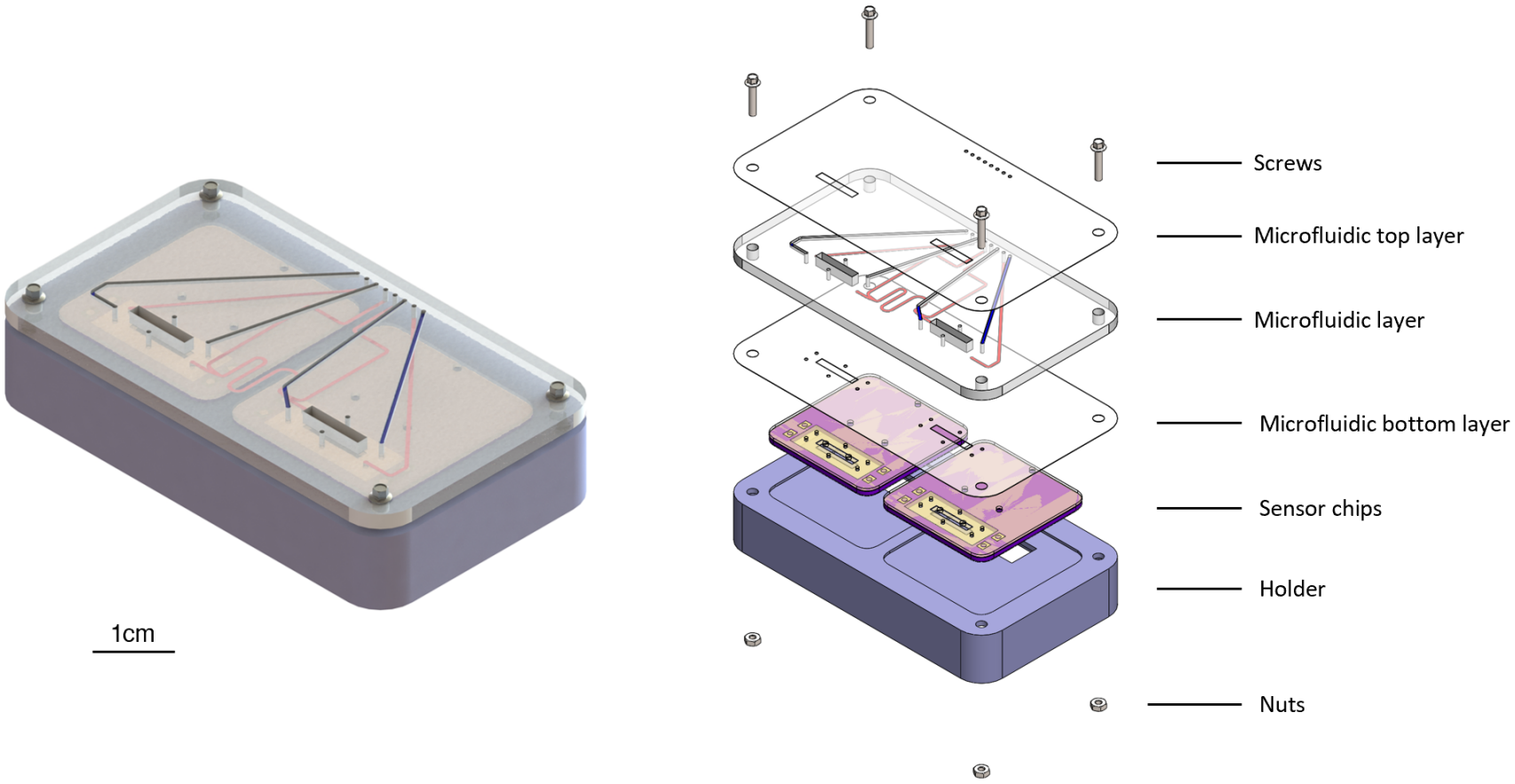

Figure B.4: Forth design iteration of linking system. The forth design uses bolts and nuts to keep all of the different layers in place and has a hollow holder that allows for extra space needed to incorporate sensor components.

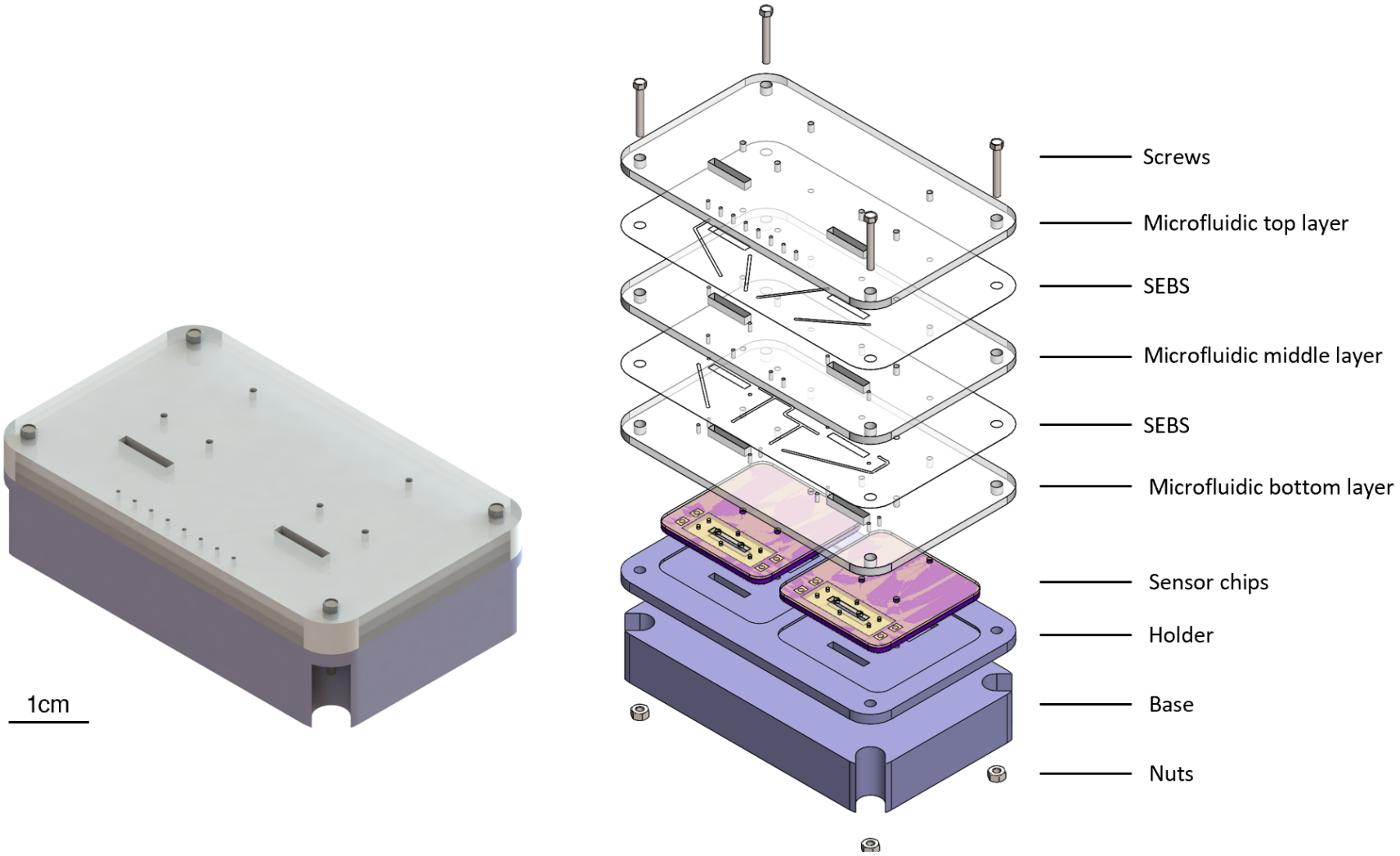

Figure B.5: Fifth design iteration of linking system. Compared to the previous design, the fifth iteration has cut outs from the base that allows for easier reachability of the screws and nuts. It also has the input ports located closer to the chip channels to decrease the total path length of the linked channels.

C

Appendix - Fabrication optimization and issues

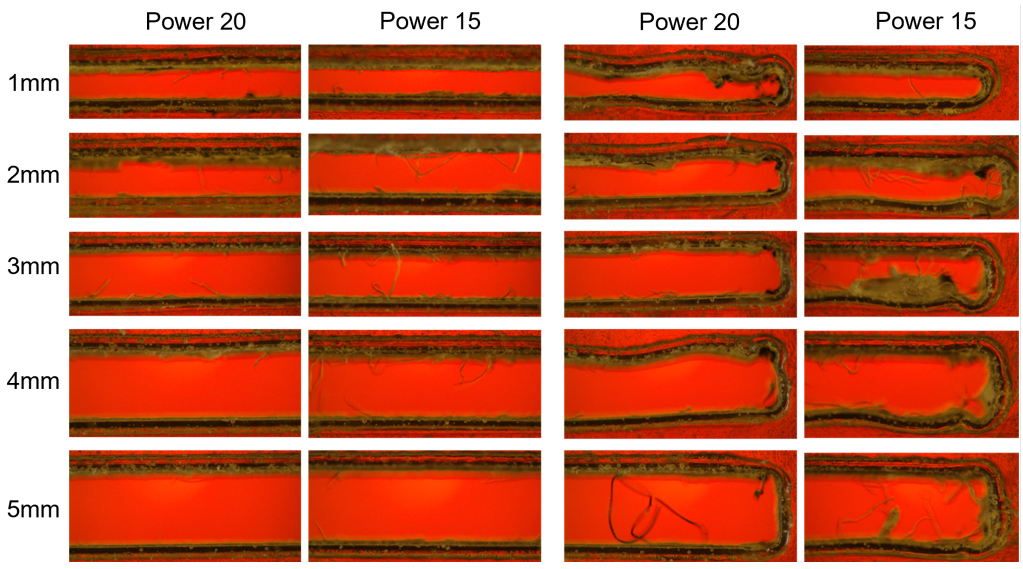

Figure C.1: Èdge smoothness of channels with varying width cut from SEBS material at varying laser cutter settings.

Figure C.2: PMMA-SEBS assemblies that were not plasma treated and were kept in a 90°C oven of 1 hour ere perfused with water and food dye for 7 days.No leaking occurred during this time.

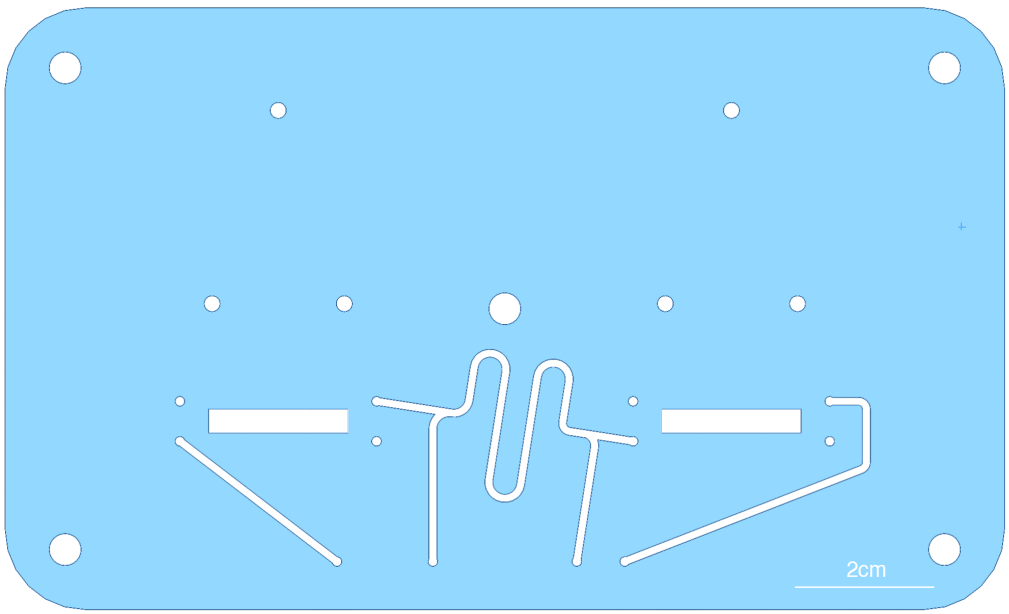

Figure C.3: Proposed mixing geometry incorporated connecting the two basal channels of the chips.

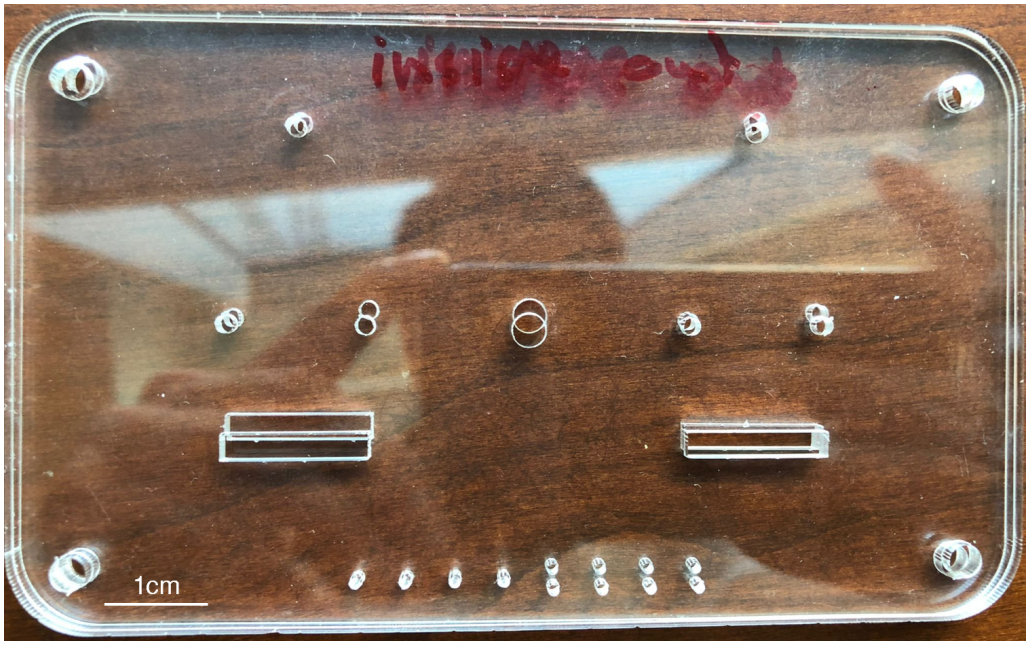

Figure C.4: Two sheets of PMMA cut from the same file with the same software settings. Variation in cut out locations can be observed. Some variations would be several millimeters, making correct alignment impossible.

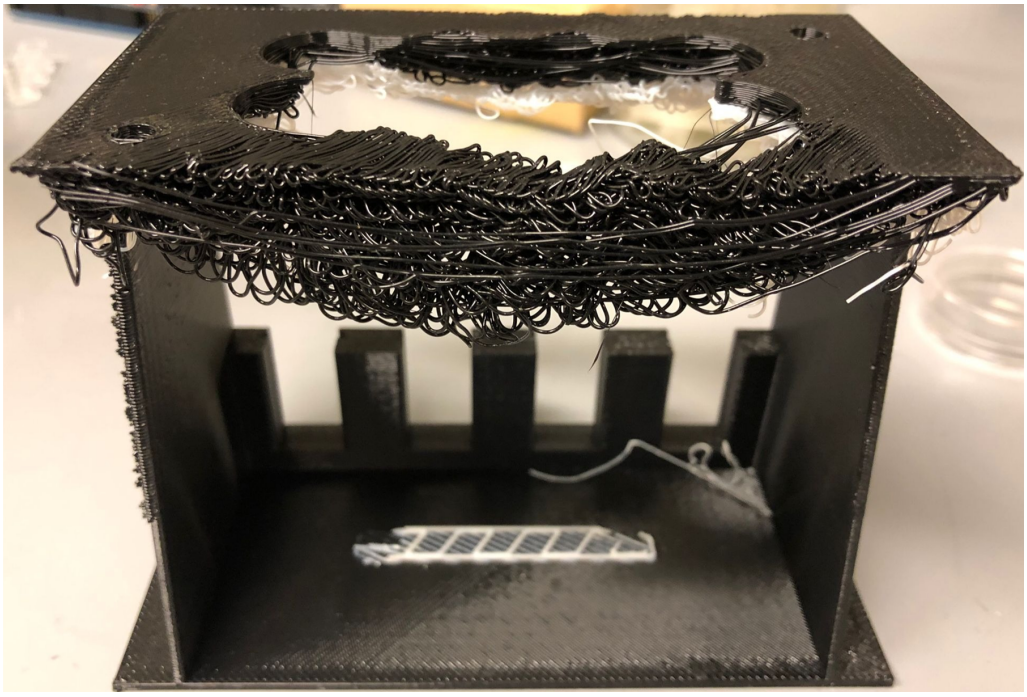

Figure C.5: 3D printer issue. Specific designs could not be printed due to insufficient support, causing the printer to extrude material in a vacuum.

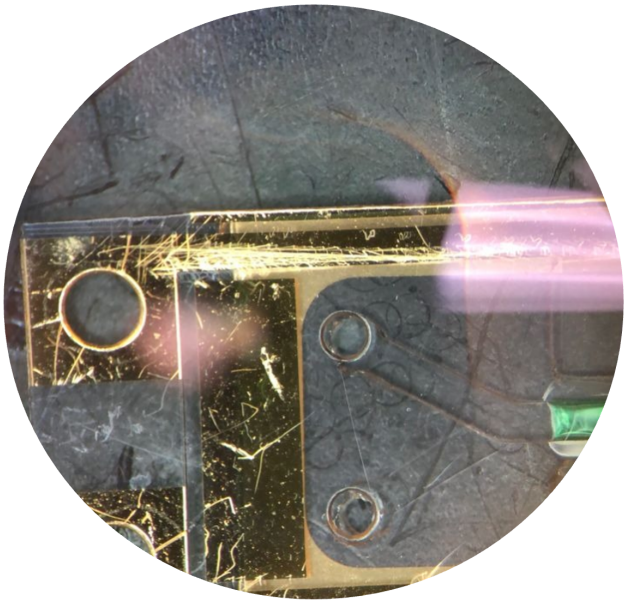

Figure C.6: Damaged chip electrode. Careless handling of the electrodes could result in damaged gold paths.

(a)

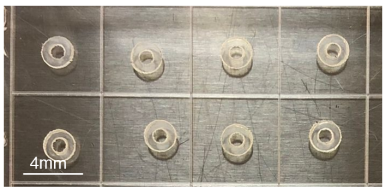

(b)

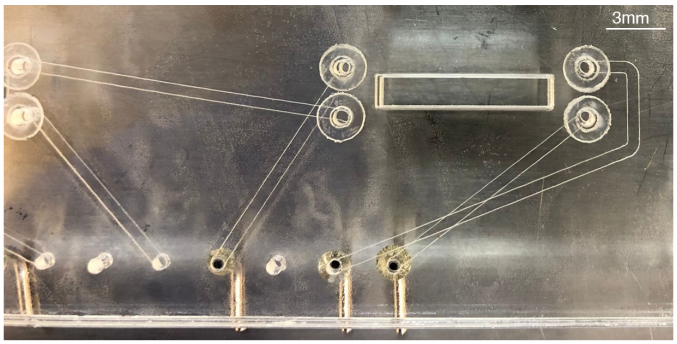

(c)

Figure C.7: PDMS and PSA rings around ports. (a) PDMS rings. (b) PSA rings. (c) The PMMA-PSA-PDMS assembly.

D

Appendix - Mixing study

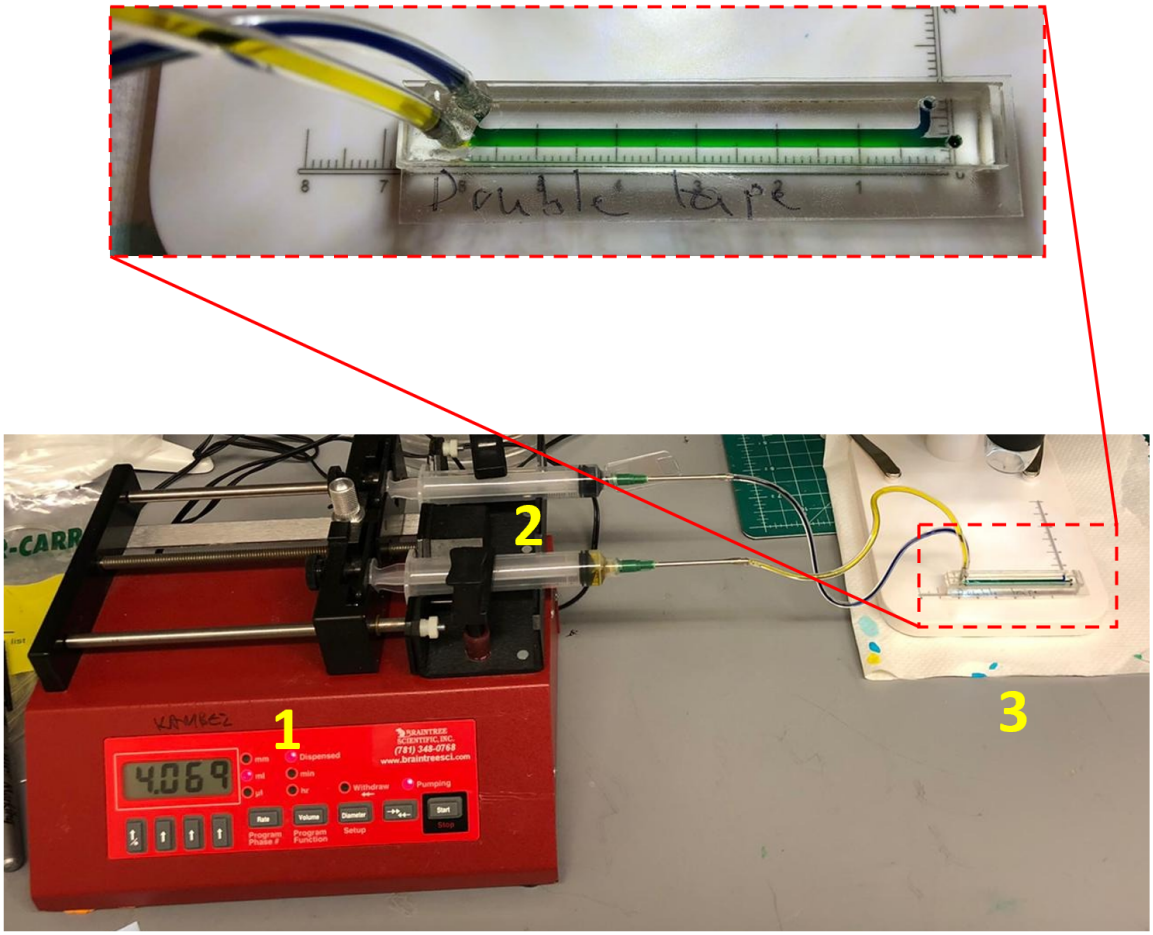

Figure D.1: Mixing setup. In order to see how geometries perform in terms of mixing, a syringe pump (1) was used to perfuse two types of food dye (2) through a microfluidic PMMA-PSA assembly (3).

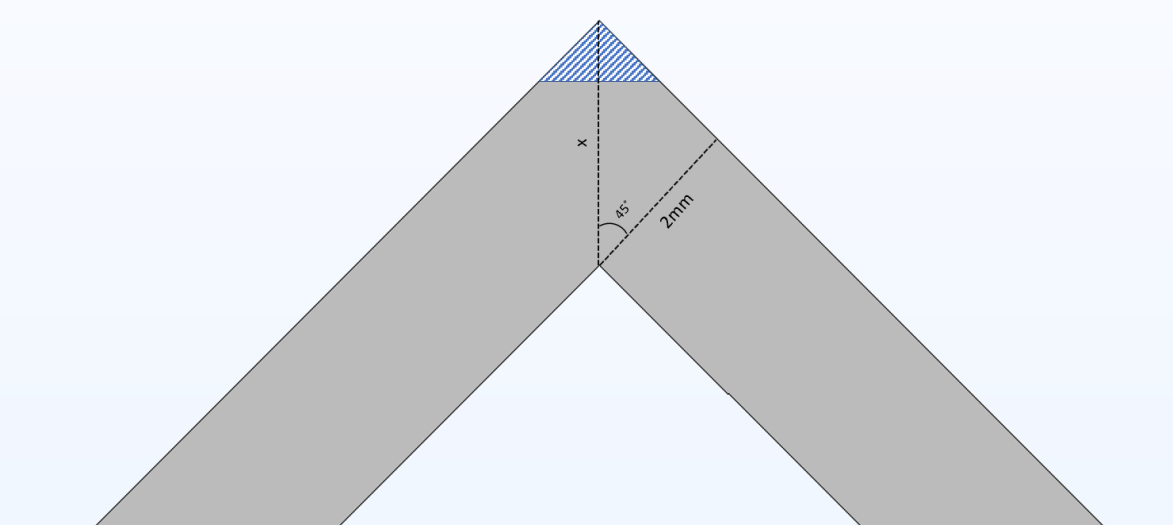

Figure D.2: Zigzag geometry analysis. The geometry in the sharp turns create a longer diffusion distance. The maximum diffusion distance in these turns is 2.81mm (x) compared to 2mm the rest of the geometry. This region is shown with the blue pattern.

E

Appendix - Sensor chip details

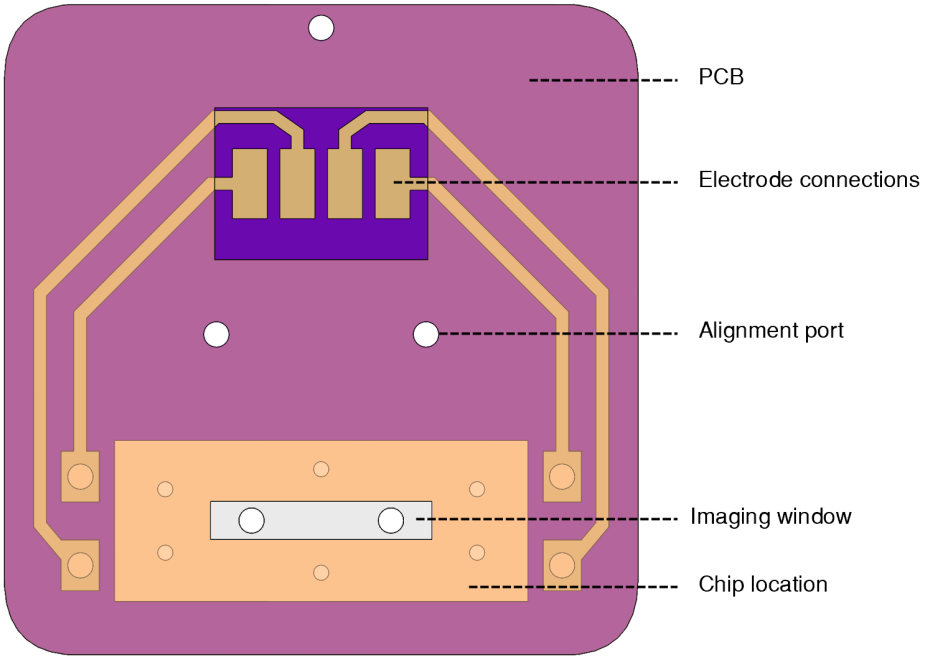

Figure E.1: Backside of the sensor chip.

F

Appendix - Sensor read-outs

(a)

(b)

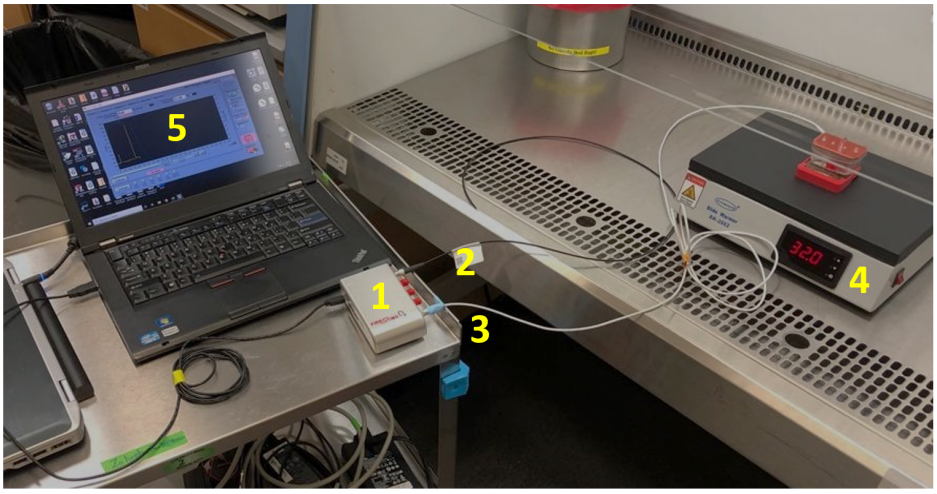

(c)

Figure F.1: O_2 read-out instruments from Pyroscience(Images obtained from https://www.pyroscience.com/en/). (a) A flexible fiber optic cable with a diameter of 2mm. (b) A Firesting O_2 meter. (c) Complete setup used for O_2 readouts including: 1. the Firesting meter 2. a fiber optic cable 3. A temperature sensor 4. A heat tray and 5. A laptop with the Pyroscience software

Figure F.2: Ivium potentiostat used for TEER read-outs.

Bibliography

[1] Dongeun Huh, Geraldine A Hamilton, and Donald E Ingber. From 3d cell culture to organs-on-chips. *Trends in cell biology*, 21(12):745–754, 2011.

[2] Jane A Foster and Karen-Anne McVey Neufeld. Gut–brain axis: how the microbiome influences anxiety and depression. *Trends in neurosciences*, 36(5):305–312, 2013.

[3] John F Cryan and Timothy G Dinan. Mind-altering microorganisms: the impact of the gut microbiota on brain and behaviour. *Nature reviews neuroscience*, 13(10):701–712, 2012.

[4] Janet Woodcock and Raymond Woosley. The fda critical path initiative and its influence on new drug development. *Annu. Rev. Med.*, 59:1–12, 2008.

[5] Harry Olson, Graham Betton, Denise Robinson, Karluss Thomas, Alastair Monro, Gerald Kolaja, Patrick Lilly, James Sanders, Glenn Sipes, William Bracken, et al. Concordance of the toxicity of pharmaceuticals in humans and in animals. *Regulatory Toxicology and Pharmacology*, 32(1):56–67, 2000.

[6] Steve Morgan, Paul Grootendorst, Joel Lexchin, Colleen Cunningham, and Devon Greyson. The cost of drug development: a systematic review. *Health policy*, 100(1):4–17, 2011.

[7] Chun Liu, Angelos Oikonomopoulos, Nazish Sayed, and Joseph C Wu. Modeling human diseases with induced pluripotent stem cells: from 2d to 3d and beyond. *Development*, 145(5):dev156166, 2018.

[8] Andries D van der Meer and Albert van den Berg. Organs-on-chips: breaking the in vitro impasse. *Integrative Biology*, 4(5):461–470, 2012.

[9] Sangeeta N Bhatia and Donald E Ingber. Microfluidic organs-on-chips. *Nature biotechnology*, 32(8): 760, 2014.

[10] J Miguel Oliveira and Rui L Reis. Biomaterials-and microfluidics-based tissue engineered 3d models.

[11] Olivier Frey, Patrick M Misun, David A Fluri, Jan G Hengstler, and Andreas Hierlemann. Reconfigurable microfluidic hanging drop network for multi-tissue interaction and analysis. *Nature communications*, 5(1):1–11, 2014.

[12] Ilka Wagner, Eva-Maria Materne, Sven Brincker, Ute Süßbier, Caroline Frädrich, Mathias Busek, Frank Sonntag, Dmitry A Sakharov, Evgeny V Trushkin, Alexander G Tonevitsky, et al. A dynamic multi-organ-chip for long-term cultivation and substance testing proven by 3d human liver and skin tissue co-culture. *Lab on a Chip*, 13(18):3538–3547, 2013.

[13] Yi Zhao, Ranjith Kumar Kankala, Shi-Bin Wang, and Ai-Zheng Chen. Multi-organs-on-chips: towards long-term biomedical investigations. *Molecules*, 24(4):675, 2019.

[14] Marinke W van Der Helm, Andries D Van Der Meer, Jan CT Eijkel, Albert van den Berg, and Loes I Segerink. Microfluidic organ-on-chip technology for blood-brain barrier research. *Tissue barriers*, 4 (1):e1142493, 2016.

[15] Jeffrey T Borenstein. Organs-on-chips: how microsystems technology can transform the drug development process. *IEEE pulse*, 7(2):22–26, 2016.

[16] George M Whitesides. The origins and the future of microfluidics. *Nature*, 442(7101):368–373, 2006.

[17] Dongeun Huh, Benjamin D Matthews, Akiko Mammoto, Martín Montoya-Zavala, Hong Yuan Hsin, and Donald E Ingber. Reconstituting organ-level lung functions on a chip. *Science*, 328(5986):1662–1668, 2010.

[18] Boyang Zhang, Anastasia Korolj, Benjamin Fook Lun Lai, and Milica Radisic. Advances in organ-on-a-chip engineering. *Nature Reviews Materials*, 3(8):257–278, 2018.

[19] Kwanchanok Viravaidya, Aaron Sin, and Michael L Shuler. Development of a microscale cell culture analog to probe naphthalene toxicity. *Biotechnology progress*, 20(1):316–323, 2004.

[20] Kwang-Ho Lee, Jaeseo Lee, Sang-Hoon Lee, et al. 3d liver models on a microplatform: well-defined culture, engineering of liver tissue and liver-on-a-chip. *Lab on a Chip*, 15(19):3822–3837, 2015.

[21] Ying I Wang, Hasan Erbil Abaci, and Michael L Shuler. Microfluidic blood–brain barrier model provides in vivo-like barrier properties for drug permeability screening. *Biotechnology and bioengineering*, 114 (1):184–194, 2017.

[22] Pranjul Shah, Joëlle V Fritz, Enrico Glaab, Mahesh S Desai, Kacy Greenhalgh, Audrey Frachet, Magdalena Niegowska, Matthew Estes, Christian Jäger, Carole Seguin-Devaux, et al. A microfluidics-based in vitro model of the gastrointestinal human–microbe interface. *Nature communications*, 7:11535, 2016.

[23] Anurag Mathur, Peter Loskill, Kaifeng Shao, Nathaniel Huebsch, SoonGweon Hong, Sivan G Marcus, Natalie Marks, Mohammad Mandegar, Bruce R Conklin, Luke P Lee, et al. Human ipsc-based cardiac microphysiological system for drug screening applications. *Scientific reports*, 5:8883, 2015.

[24] Elijah J Weber, Alenka Chapron, Brian D Chapron, Jenna L Voellinger, Kevin A Lidberg, Catherine K Yeung, Zhican Wang, Yoshiyuki Yamaura, Dale W Hailey, Thomas Neumann, et al. Development of a microphysiological model of human kidney proximal tubule function. *Kidney international*, 90(3): 627–637, 2016.

[25] Katharina Schimek, Hao-Hsiang Hsu, Moritz Boehme, Jacob Jan Kornet, Uwe Marx, Roland Lauster, Ralf Pörtner, and Gerd Lindner. Bioengineering of a full-thickness skin equivalent in a 96-well insert format for substance permeation studies and organ-on-a-chip applications. *Bioengineering*, 5(2):43, 2018.

[26] Shuo Xiao, Jonathan R Coppeta, Hunter B Rogers, Brett C Isenberg, Jie Zhu, Susan A Olalekan, Kelly E McKinnon, Danijela Dokic, Alexandra S Rashedi, Daniel J Haisenleder, et al. A microfluidic culture model of the human reproductive tract and 28-day menstrual cycle. *Nature communications*, 8:14584, 2017.

[27] Carl-Fredrik Mandenius. Conceptual design of micro-bioreactors and organ-on-chips for studies of cell cultures. *Bioengineering*, 5(3):56, 2018.

[28] Aziz Ur Rehman Aziz, Chunyang Geng, Mengjie Fu, Xiaohui Yu, Kairong Qin, and Bo Liu. The role of microfluidics for organ on chip simulations. *Bioengineering*, 4(2):39, 2017.

[29] Ishtiaq Ahmed, Hafiz MN Iqbal, and Zain Akram. Microfluidics engineering: Recent trends, valorization, and applications. *Arabian Journal for Science and Engineering*, 43(1):23–32, 2018.

[30] Suman Chakraborty et al. Microfluidics and microfabrication. 2010.

[31] Pilnam Kim, Keon Woo Kwon, Min Cheol Park, Sung Hoon Lee, Sun Min Kim, and Kahp Yang Suh. Soft lithography for microfluidics: a review. 2008.

[32] Robert H Todd, Dell K Allen, and Leo Alting. *Manufacturing processes reference guide*. Industrial Press Inc., 1994.

[33] Tugba Kilic, Fatemeh Navaee, Francesca Stradolini, Philippe Renaud, and Sandro Carrara. Organs-on-chip monitoring: sensors and other strategies. *Microphysiol. Syst*, 2(5), 2018.

[34] Kacey Ronaldson-Bouchard and Gordana Vunjak-Novakovic. Organs-on-a-chip: a fast track for engineered human tissues in drug development. *Cell stem cell*, 22(3):310–324, 2018.

[35] Ross Booth and Hanseup Kim. Characterization of a microfluidic in vitro model of the blood-brain barrier (μbbb). *Lab on a Chip*, 12(10):1784–1792, 2012.

[36] Arnout Schepers, Cheri Li, Arnav Chhabra, Benjamin Tschudy Seney, and Sangeeta Bhatia. Engineering a perfusable 3d human liver platform from ips cells. *Lab on a Chip*, 16(14):2644–2653, 2016.

[37] Anna Marsano, Chiara Conficconi, Marta Lemme, Paola Occhetta, Emanuele Gaudiello, Emiliano Votta, Giulia Cerino, Alberto Redaelli, and Marco Rasponi. Beating heart on a chip: a novel microfluidic platform to generate functional 3d cardiac microtissues. *Lab on a Chip*, 16(3):599–610, 2016.

[38] Sejoong Kim, Sasha Cai LesherPerez, Cameron Yamanishi, Joseph M Labuz, Brendan Leung, Shuichi Takayama, et al. Pharmacokinetic profile that reduces nephrotoxicity of gentamicin in a perfused kidney-on-a-chip. *Biofabrication*, 8(1):015021, 2016.

[39] Dee Unglaub Silverthorn, William C Ober, Claire W Garrison, Andrew C Silverthorn, and Bruce R Johnson. *Human physiology: an integrated approach*. Pearson/Benjamin Cummings San Francisco, 2010.

[40] Wendy S Garrett, Jeffrey I Gordon, and Laurie H Glimcher. Homeostasis and inflammation in the intestine. *Cell*, 140(6):859–870, 2010.

[41] Hyun Jung Kim, Hu Li, James J Collins, and Donald E Ingber. Contributions of microbiome and mechanical deformation to intestinal bacterial overgrowth and inflammation in a human gut-on-a-chip. *Proceedings of the National Academy of Sciences*, 113(1):E7–E15, 2016.

[42] Lonneke M Griep, Floor Wolbers, Bjorn de Wagenaar, Paulus Martinus ter Braak, BB Weksler, Ignacio A Romero, PO Couraud, I Vermes, Andries Dirk van der Meer, and Albert van den Berg. Bbb on chip: microfluidic platform to mechanically and biochemically modulate blood-brain barrier function. *Biomedical microdevices*, 15(1):145–150, 2013.

[43] Jacquelyn A Brown, Virginia Pensabene, Dmitry A Markov, Vanessa Allwardt, M Diana Neely, Mingjian Shi, Clayton M Britt, Orlando S Hoilett, Qing Yang, Bryson M Brewer, et al. Recreating blood-brain barrier physiology and structure on chip: A novel neurovascular microfluidic bioreactor. *Biomicrofluidics*, 9(5):054124, 2015.

[44] Iva Kelava and Madeline A Lancaster. Stem cell models of human brain development. *Cell stem cell*, 18 (6):736–748, 2016.

[45] Philip J Lee, Paul J Hung, and Luke P Lee. An artificial liver sinusoid with a microfluidic endothelial-like barrier for primary hepatocyte culture. *Biotechnology and bioengineering*, 97(5):1340–1346, 2007.

[46] Hüseyin AVCI, Fatma DOĞAN GÜZEL, Salim Erol, and Ali Akpek. Recent advances in organ-on-a-chip technologies and future challenges: a review. *Turkish Journal of Chemistry*, 42(3), 2018.

[47] Juan Eduardo Sosa-Hernández, Angel M Villalba-Rodríguez, Kenya D Romero-Castillo, Mauricio A Aguilar-Aguila-Isaías, Isaac E García-Reyes, Arturo Hernández-Antonio, Ishtiaq Ahmed, Ashutosh Sharma, Roberto Parra-Saldívar, and Hafiz Iqbal. Organs-on-a-chip module: a review from the development and applications perspective. *Micromachines*, 9(10):536, 2018.

[48] Abhinav Bhushan, Nina Senutovitch, Shyam S Bale, William J McCarty, Manjunath Hegde, Rohit Jindal, Inna Golberg, O Berk Usta, Martin L Yarmush, Lawrence Vernetti, et al. Towards a three-dimensional microfluidic liver platform for predicting drug efficacy and toxicity in humans. *Stem cell research & therapy*, 4(1):S16, 2013.

[49] Adam Williamson, Sukhdeep Singh, Uta Fernekorn, and Andreas Schober. The future of the patient-specific body-on-a-chip. *Lab on a Chip*, 13(18):3471–3480, 2013.

[50] Anna Grosberg, Patrick W Alford, Megan L McCain, and Kevin Kit Parker. Ensembles of engineered cardiac tissues for physiological and pharmacological study: heart on a chip. *Lab on a chip*, 11(24): 4165–4173, 2011.

[51] Lauran R Madden, Derek J Mortisen, Eric M Sussman, Sarah K Dupras, James A Fugate, Janet L Cuy, Kip D Hauch, Michael A Laflamme, Charles E Murry, and Buddy D Ratner. Proangiogenic scaffolds as functional templates for cardiac tissue engineering. *Proceedings of the National Academy of Sciences*, 107(34):15211–15216, 2010.

[52] Su Ryon Shin, Sung Mi Jung, Momen Zalabany, Keekyoung Kim, Pinar Zorlutuna, Sang bok Kim, Mehdi Nikkhah, Masoud Khabiry, Mohamed Azize, Jing Kong, et al. Carbon-nanotube-embedded hydrogel sheets for engineering cardiac constructs and bioactuators. *ACS nano*, 7(3):2369–2380, 2013.

[53] Ian Wheeldon, Amirhossein F Ahari, and Ali Khademhosseini. Microengineering hydrogels for stem cell bioengineering and tissue regeneration. *JALA: Journal of the Association for Laboratory Automation*, 15 (6):440–448, 2010.

[54] Kyung-Jin Jang and Kahp-Yang Suh. A multi-layer microfluidic device for efficient culture and analysis of renal tubular cells. *Lab on a Chip*, 10(1):36–42, 2010.

[55] Courtney M Sakolish, Brian Philip, and Gretchen J Mahler. A human proximal tubule-on-a-chip to study renal disease and toxicity. *Biomicrofluidics*, 13(1):014107, 2019.

[56] Frans Schutgens, Maarten B Rookmaaker, Thanasis Margaritis, Anne Rios, Carola Ammerlaan, Jitske Jansen, Linda Gijzen, Marianne Vormann, Annelotte Vonk, Marco Viveen, et al. Tubuloids derived from human adult kidney and urine for personalized disease modeling. *Nature biotechnology*, 37(3): 303–313, 2019.

[57] Tom TG Nieskens and Anna-Karin Sjögren. Emerging in vitro systems to screen and predict drug-induced kidney toxicity. In *Seminars in nephrology*, volume 39, pages 215–226. Elsevier, 2019.

[58] Julia Rogal, Christopher Probst, and Peter Loskill. Integration concepts for multi-organ chips: how to maintain flexibility?! *Future science OA*, 3(2):FSO180, 2017.

[59] Gordana Vunjak-Novakovic, Sangeeta Bhatia, Christopher Chen, and Karen Hirschi. Heliva platform: integrated heart-liver-vascular systems for drug testing in human health and disease. *Stem cell research & therapy*, 4(1):1–6, 2013.

[60] John P Wikswo, Erica L Curtis, Zachary E Eagleton, Brian C Evans, Ayeeshik Kole, Lucas H Hofmeister, and William J Matloff. Scaling and systems biology for integrating multiple organs-on-a-chip. *Lab on a Chip*, 13(18):3496–3511, 2013.

[61] Daniel A Tatosian and Michael L Shuler. A novel system for evaluation of drug mixtures for potential efficacy in treating multidrug resistant cancers. *Biotechnology and bioengineering*, 103(1):187–198, 2009.

[62] Yuki Imura, Kiichi Sato, and Etsuro Yoshimura. Micro total bioassay system for ingested substances: assessment of intestinal absorption, hepatic metabolism, and bioactivity. *Analytical chemistry*, 82(24): 9983–9988, 2010.

[63] Simone Bersini, Jessie S Jeon, Gabriele Dubini, Chiara Arrigoni, Seok Chung, Joseph L Charest, Matteo Moretti, and Roger D Kamm. A microfluidic 3d in vitro model for specificity of breast cancer metastasis to bone. *Biomaterials*, 35(8):2454–2461, 2014.

[64] Zhiyun Xu, Encheng Li, Zhe Guo, Ruofei Yu, Hualong Hao, Yitong Xu, Zhao Sun, Xiancheng Li, Jianxin Lyu, and Qi Wang. Design and construction of a multi-organ microfluidic chip mimicking the in vivo microenvironment of lung cancer metastasis. *ACS applied materials & interfaces*, 8(39):25840–25847, 2016.

[65] Aleksander Skardal, Mahesh Devarasetty, Steven Forsythe, Anthony Atala, and Shay Soker. A reductionist metastasis-on-a-chip platform for in vitro tumor progression modeling and drug screening. *Biotechnology and bioengineering*, 113(9):2020–2032, 2016.

[66] T Satoh, S Sugiura, K Shin, R Onuki-Nagasaki, S Ishida, K Kikuchi, M Kakiki, and T Kanamori. A multi-throughput multi-organ-on-a-chip system on a plate formatted pneumatic pressure-driven medium circulation platform. *Lab on a Chip*, 18(1):115–125, 2018.

[67] Michael L Shuler. Organ-, body-and disease-on-a-chip systems. *Lab on a Chip*, 17(14):2345–2346, 2017.

[68] Jong Hwan Sung, Carrie Kam, and Michael L Shuler. A microfluidic device for a pharmacokinetic–pharmacodynamic (pk–pd) model on a chip. *Lab on a Chip*, 10(4):446–455, 2010.

[69] Ilka Maschmeyer, Alexandra K Lorenz, Katharina Schimek, Tobias Hasenberg, Anja P Ramme, Juliane Hübner, Marcus Lindner, Christopher Drewell, Sophie Bauer, Alexander Thomas, et al. A four-organ-chip for interconnected long-term co-culture of human intestine, liver, skin and kidney equivalents. *Lab on a Chip*, 15(12):2688–2699, 2015.

[70] Eva-Maria Materne, Anja Patricia Ramme, Ana Paula Terrasso, Margarida Serra, Paula Marques Alves, Catarina Brito, Dmitry A Sakharov, Alexander G Tonevitsky, Roland Lauster, and Uwe Marx. A multi-organ chip co-culture of neurospheres and liver equivalents for long-term substance testing. *Journal of biotechnology*, 205:36–46, 2015.

[71] Carlota Oleaga, Anne Riu, Sandra Rothemund, Andrea Lavado, Christopher W McAleer, Christopher J Long, Keisha Persaud, Narasimhan Sriram Narasimhan, My Tran, Jeffry Roles, et al. Investigation of the effect of hepatic metabolism on off-target cardiotoxicity in a multi-organ human-on-a-chip system. *Biomaterials*, 182:176–190, 2018.

[72] Hasan Erbil Abaci and Michael L Shuler. Human-on-a-chip design strategies and principles for physiologically based pharmacokinetics/pharmacodynamics modeling. *Integrative Biology*, 7(4):383–391, 2015.

[73] Dae-Wook Kang, Jin Gyoon Park, Zehra Esra Ilhan, Garrick Wallstrom, Joshua LaBaer, James B Adams, and Rosa Krajmalnik-Brown. Reduced incidence of prevotella and other fermenters in intestinal microflora of autistic children. *PloS one*, 8(7):e68322, 2013.

[74] E Barrett, RP Ross, PW O'toole, GF Fitzgerald, and C Stanton. γ-aminobutyric acid production by culturable bacteria from the human intestine. *Journal of applied microbiology*, 113(2):411–417, 2012.

[75] Eileen A Curran, Sinéad M O'Neill, John F Cryan, Louise C Kenny, Timothy G Dinan, Ali S Khashan, and Patricia M Kearney. Research review: Birth by caesarean section and development of autism spectrum disorder and attention-deficit/hyperactivity disorder: A systematic review and meta-analysis. *Journal of Child Psychology and Psychiatry*, 56(5):500–508, 2015.

[76] Elaine Y Hsiao, Sara W McBride, Sophia Hsien, Gil Sharon, Embriette R Hyde, Tyler McCue, Julian A Codelli, Janet Chow, Sarah E Reisman, Joseph F Petrosino, et al. Microbiota modulate behavioral and physiological abnormalities associated with neurodevelopmental disorders. *Cell*, 155(7):1451–1463, 2013.

[77] Duc TT Phan, R Hugh F Bender, Jillian W Andrejecsk, Agua Sobrino, Stephanie J Hachey, Steven C George, and Christopher CW Hughes. Blood–brain barrier-on-a-chip: Microphysiological systems that capture the complexity of the blood–central nervous system interface. *Experimental Biology and Medicine*, 242(17):1669–1678, 2017.

[78] Arianna Oddo, Bo Peng, Ziqiu Tong, Yingkai Wei, Wing Yin Tong, Helmut Thissen, and Nicolas Hans Voelcker. Advances in microfluidic blood–brain barrier (bbb) models. *Trends in biotechnology*, 37(12): 1295–1314, 2019.

[79] Ben M Maoz, Anna Herland, Edward A FitzGerald, Thomas Grevesse, Charles Vidoudez, Alan R Pacheco, Sean P Sheehy, Tae-Eun Park, Stephanie Dauth, Robert Mannix, et al. A linked organ-on-chip model of the human neurovascular unit reveals the metabolic coupling of endothelial and neuronal cells. *Nature biotechnology*, 36(9):865–874, 2018.

[80] Sudhir P Deosarkar, Balabhaskar Prabhakarpandian, Bin Wang, Joel B Sheffield, Barbara Krynska, and Mohammad F Kiani. A novel dynamic neonatal blood-brain barrier on a chip. *PloS one*, 10(11): e0142725, 2015.

[81] Jonathan W Song and Lance L Munn. Fluid forces control endothelial sprouting. *Proceedings of the National Academy of Sciences*, 108(37):15342–15347, 2011.

[82] Mohammad A Kaisar, Ravi K Sajja, Shikha Prasad, Vinay V Abhyankar, Taylor Liles, and Luca Cucullo. New experimental models of the blood-brain barrier for cns drug discovery. *Expert opinion on drug discovery*, 12(1):89–103, 2017.

[83] Daniela E Eigenmann, Gongda Xue, Kwang S Kim, Ashlee V Moses, Matthias Hamburger, and Mouhssin Oufir. Comparative study of four immortalized human brain capillary endothelial cell lines, hcmec/d3, hbmec, ty10, and bb19, and optimization of culture conditions, for an in vitro blood–brain barrier model for drug permeability studies. *Fluids and Barriers of the CNS*, 10(1):33, 2013.

[84] Giulia Adriani, Dongliang Ma, Andrea Pavesi, Roger D Kamm, and Eyleen LK Goh. A 3d neurovascular microfluidic model consisting of neurons, astrocytes and cerebral endothelial cells as a blood–brain barrier. *Lab on a Chip*, 17(3):448–459, 2017.

[85] S Aday, R Cecchelli, D Hallier-Vanuxeem, MP Dehouck, and L Ferreira. Stem cell-based human blood–brain barrier models for drug discovery and delivery. *Trends in Biotechnology*, 34(5):382–393, 2016.

[86] Reka Natarajan, Nicole Northrop, and Bryan Yamamoto. Fluorescein isothiocyanate (fitc)-dextran extravasation as a measure of blood-brain barrier permeability. *Current protocols in neuroscience*, 79 (1):9–58, 2017.

[87] Hansang Cho, Ji Hae Seo, Keith HK Wong, Yasukazu Terasaki, Joseph Park, Kiwan Bong, Ken Arai, Eng H Lo, and Daniel Irimia. Three-dimensional blood-brain barrier model for in vitro studies of neurovascular pathology. *Scientific reports*, 5:15222, 2015.

[88] Ju Hun Yeon, Dokyun Na, Kyungsun Choi, Seung-Wook Ryu, Chulhee Choi, and Je-Kyun Park. Reliable permeability assay system in a microfluidic device mimicking cerebral vasculatures. *Biomedical microdevices*, 14(6):1141–1148, 2012.

[89] Anil Kumar H Achyuta, Amy J Conway, Richard B Crouse, Emilee C Bannister, Robin N Lee, Christopher P Katnik, Adam A Behensky, Javier Cuevas, and Shivshankar S Sundaram. A modular approach to create a neurovascular unit-on-a-chip. *Lab on a Chip*, 13(4):542–553, 2013.

[90] Balabhaskar Prabhakarpandian, Ming-Che Shen, Joseph B Nichols, Ivy R Mills, Marta Sidoryk-Wegrzynowicz, Michael Aschner, and Kapil Pant. Sym-bbb: a microfluidic blood brain barrier model. *Lab on a Chip*, 13(6):1093–1101, 2013.

[91] Jeong Ah Kim, Hong Nam Kim, Sun-Kyoung Im, Seok Chung, Ji Yoon Kang, and Nakwon Choi. Collagen-based brain microvasculature model in vitro using three-dimensional printed template. *Biomicrofluidics*, 9(2):024115, 2015.

[92] Katelyn L Sellgren, Brian T Hawkins, and Sonia Grego. An optically transparent membrane supports shear stress studies in a three-dimensional microfluidic neurovascular unit model. *Biomicrofluidics*, 9 (6):061102, 2015.

[93] Fruzsina R Walter, Sándor Valkai, András Kincses, András Petneházi, Tamás Czeller, Szilvia Veszelka, Pál Ormos, Mária A Deli, and András Dér. A versatile lab-on-a-chip tool for modeling biological barriers. *Sensors and Actuators B: Chemical*, 222:1209–1219, 2016.

[94] Anna Herland, Andries D van der Meer, Edward A FitzGerald, Tae-Eun Park, Jelle JF Sleeboom, and Donald E Ingber. Distinct contributions of astrocytes and pericytes to neuroinflammation identified in a 3d human blood-brain barrier on a chip. *PLoS One*, 11(3):e0150360, 2016.

[95] Hui Xu, Zhongyu Li, Yue Yu, Saman Sizdahkhani, Winson S Ho, Fangchao Yin, Li Wang, Guoli Zhu, Min Zhang, Lei Jiang, et al. A dynamic in vivo-like organotypic blood-brain barrier model to probe metastatic brain tumors. *Scientific reports*, 6:36670, 2016.

[96] Andrea P Falanga, Gabriele Pitingolo, Maurizio Celentano, Armando Cosentino, Pietro Melone, Raffaele Vecchione, Daniela Guarnieri, and Paolo A Netti. Shuttle-mediated nanoparticle transport across an in vitro brain endothelium under flow conditions. *Biotechnology and bioengineering*, 114(5):1087–1095, 2017.

[97] Paul P Partyka, George A Godsey, John R Galie, Mary C Kosciuk, Nimish K Acharya, Robert G Nagele, and Peter A Galie. Mechanical stress regulates transport in a compliant 3d model of the blood-brain barrier. *Biomaterials*, 115:30–39, 2017.

[98] Tori B Terrell-Hall, Amanda G Ammer, Jessica IG Griffith, and Paul R Lockman. Permeability across a novel microfluidic blood-tumor barrier model. *Fluids and Barriers of the CNS*, 14(1):1–10, 2017.

[99] Seokyoung Bang, Seung-Ryeol Lee, Jihoon Ko, Kyungmin Son, Dongha Tahk, Jungho Ahn, Changkyun Im, and Noo Li Jeon. A low permeability microfluidic blood-brain barrier platform with direct contact between perfusable vascular network and astrocytes. *Scientific reports*, 7(1):1–10, 2017.

[100] Attilio Marino, Omar Tricinci, Matteo Battaglini, Carlo Filippeschi, Virgilio Mattoli, Edoardo Sinibaldi, and Gianni Ciofani. A 3d real-scale, biomimetic, and biohybrid model of the blood-brain barrier fabricated through two-photon lithography. *Small*, 14(6):1702959, 2018.

[101] Nienke R Wevers, Dhanesh G Kasi, Taylor Gray, Karlijn J Wilschut, Benjamin Smith, Remko Van Vught, Fumitaka Shimizu, Yasuteru Sano, Takashi Kanda, Graham Marsh, et al. A perfused human blood–brain barrier on-a-chip for high-throughput assessment of barrier function and antibody transport. *Fluids and Barriers of the CNS*, 15(1):23, 2018.

[102] Sehoon Jeong, Sunja Kim, John Buonocore, Jaewon Park, C Jane Welsh, Jianrong Li, and Arum Han. A three-dimensional arrayed microfluidic blood–brain barrier model with integrated electrical sensor array. *IEEE Transactions on Biomedical Engineering*, 65(2):431–439, 2017.

[103] Iason Papademetriou, Else Vedula, Joseph Charest, and Tyrone Porter. Effect of flow on targeting and penetration of angiopep-decorated nanoparticles in a microfluidic model blood-brain barrier. *PloS one*, 13(10):e0205158, 2018.

[104] Abraham L Kierszenbaum and Laura Tres. *Histology and Cell Biology: an introduction to pathology E-Book*. Elsevier Health Sciences, 2015.

[105] Richard J Grand, John B Watkins, and Frank M Torti. Development of the human gastrointestinal tract: a review. *Gastroenterology*, 70(5):790–810, 1976.

[106] Amir Bein, Woojung Shin, Sasan Jalili-Firoozinezhad, Min Hee Park, Alexandra Sontheimer-Phelps, Alessio Tovaglieri, Angeliki Chalkiadaki, Hyun Jung Kim, and Donald E Ingber. Microfluidic organ-on-a-chip models of human intestine. *Cellular and molecular gastroenterology and hepatology*, 5(4): 659–668, 2018.

[107] Nureddin Ashammakhi, Rohollah Nasiri, Natan Roberto De Barros, Peyton Tebon, Jai Thakor, Marcus Goudie, Amir Shamloo, Martin G Martin, and Ali Khademhosseni. Gut-on-a-chip: Current progress and future opportunities. *Biomaterials*, page 120196, 2020.

[108] Sebastiaan J Trietsch, Elena Naumovska, Dorota Kurek, Meily C Setyawati, Marianne K Vormann, Karlijn J Wilschut, Henriëtte L Lanz, Arnaud Nicolas, Chee Ping Ng, Jos Joore, et al. Membrane-free culture and real-time barrier integrity assessment of perfused intestinal epithelium tubes. *Nature communications*, 8(1):1–8, 2017.

[109] Sasan Jalili-Firoozinezhad, Francesca S Gazzaniga, Elizabeth L Calamari, Diogo M Camacho, Cicely W Fadel, Amir Bein, Ben Swenor, Bret Nestor, Michael J Cronce, Alessio Tovaglieri, et al. A complex human gut microbiome cultured in an anaerobic intestine-on-a-chip. *Nature biomedical engineering*, 3(7):520, 2019.

[110] Y Sambuy, I De Angelis, G Ranaldi, ML Scarino, A Stammati, and F Zucco. The caco-2 cell line as a model of the intestinal barrier: influence of cell and culture-related factors on caco-2 cell functional characteristics. *Cell biology and toxicology*, 21(1):1–26, 2005.

[111] Tor Lea. Caco-2 cell line. In *The impact of food bioactives on health*, pages 103–111. Springer, Cham, 2015.

[112] Nureddin A Ashammakhi and Adam Elzagheid. Organ-on-a-chip: new tool for personalized medicine. *Journal of Craniofacial Surgery*, 29(4):823–824, 2018.

[113] Meiying Chi, Banya Yi, Seunghan Oh, Dong-June Park, Jong Hwan Sung, and Sungsu Park. A microfluidic cell culture device (μfccd) to culture epithelial cells with physiological and morphological properties that mimic those of the human intestine. *Biomedical microdevices*, 17(3):58, 2015.

[114] Alexandre Grassart, Valérie Malardé, Samy Gobaa, Anna Sartori-Rupp, Jordan Kerns, Katia Karalis, Benoit Marteyn, Philippe Sansonetti, and Nathalie Sauvonnet. Bioengineered human organ-on-chip reveals intestinal microenvironment and mechanical forces impacting shigella infection. *Cell host & microbe*, 26(3):435–444, 2019.

[115] J Cooper McDonald and George M Whitesides. Poly (dimethylsiloxane) as a material for fabricating microfluidic devices. *Accounts of chemical research*, 35(7):491–499, 2002.

[116] Courtney M Sakolish, Mandy B Esch, James J Hickman, Michael L Shuler, and Gretchen J Mahler. Modeling barrier tissues in vitro: methods, achievements, and challenges. *EBioMedicine*, 5:30–39, 2016.

[117] Balaji Srinivasan, Aditya Reddy Kolli, Mandy Brigitte Esch, Hasan Erbil Abaci, Michael L Shuler, and James J Hickman. Teer measurement techniques for in vitro barrier model systems. *Journal of laboratory automation*, 20(2):107–126, 2015.

[118] Manuela Teresa Raimondi, Diego Albani, and Carmen Giordano. An organ-on-a-chip engineered platform to study the microbiota–gut–brain axis in neurodegeneration. *Trends in molecular medicine*, 25(9):737–740, 2019.

[119] Nikolaos Tsamandouras, Wen Li Kelly Chen, Collin D Edington, Cynthia L Stokes, Linda G Griffith, and Murat Cirit. Integrated gut and liver microphysiological systems for quantitative in vitro pharmacokinetic studies. *The AAPS journal*, 19(5):1499–1512, 2017.

[120] Lawrence Vernetti, Albert Gough, Nicholas Baetz, Sarah Blutt, James R Broughman, Jacquelyn A Brown, Jennifer Foulke-Abel, Nesrin Hasan, Julie In, Edward Kelly, et al. Functional coupling of human microphysiology systems: intestine, liver, kidney proximal tubule, blood-brain barrier and skeletal muscle. *Scientific reports*, 7:42296, 2017.

[121] Ben M Maoz, Anna Herland, Olivier YF Henry, William D Leineweber, Moran Yadid, John Doyle, Robert Mannix, Ville J Kujala, Edward A FitzGerald, Kevin Kit Parker, et al. Organs-on-chips with combined multi-electrode array and transepithelial electrical resistance measurement capabilities. *Lab on a Chip*, 17(13):2294–2302, 2017.

[122] Yu Shrike Zhang, Julio Aleman, Su Ryon Shin, Tugba Kilic, Duckjin Kim, Seyed Ali Mousavi Shaegh, Solange Massa, Reza Riahi, Sukyoung Chae, Ning Hu, et al. Multisensor-integrated organs-on-chips platform for automated and continual in situ monitoring of organoid behaviors. *Proceedings of the National Academy of Sciences*, 114(12):E2293–E2302, 2017.

[123] Jochen Kieninger, Andreas Weltin, Hubert Flamm, and Gerald A Urban. Microsensor systems for cell metabolism–from 2d culture to organ-on-chip. *Lab on a Chip*, 18(9):1274–1291, 2018.

[124] Roland Thuenauer, Enrique Rodriguez-Boulan, and Winfried Römer. Microfluidic approaches for epithelial cell layer culture and characterisation. *Analyst*, 139(13):3206–3218, 2014.

[125] Olivier YF Henry, Remi Villenave, Michael J Cronce, William D Leineweber, Maximilian A Benz, and Donald E Ingber. Organs-on-chips with integrated electrodes for trans-epithelial electrical resistance (teer) measurements of human epithelial barrier function. *Lab on a Chip*, 17(13):2264–2271, 2017.

[126] Hyun Jung Kim, Dongeun Huh, Geraldine Hamilton, and Donald E Ingber. Human gut-on-a-chip inhabited by microbial flora that experiences intestinal peristalsis-like motions and flow. *Lab on a Chip*, 12(12):2165–2174, 2012.

[127] Ludivine Bol, Jean-Christophe Galas, Hervé Hillaireau, Isabelle Le Potier, Valérie Nicolas, Anne-Marie Haghiri-Gosnet, Elias Fattal, and Myriam Taverna. A microdevice for parallelized pulmonary permeability studies. *Biomedical microdevices*, 16(2):277–285, 2014.

[128] Paul A Vogel, Stephen T Halpin, R Scott Martin, and Dana M Spence. Microfluidic transendothelial electrical resistance measurement device that enables blood flow and postgrowth experiments. *Analytical chemistry*, 83(11):4296–4301, 2011.

[129] Elsbeth GBM Bossink, Olivier YF Henry, Maximilian A Benz, Loes Segerink, Donald E Ingber, and Mathieu Odijk. A miniaturized clark oxygen sensor for organ-on-chip devices. In *22nd International Conference on Miniaturized Systems for Chemistry and Life Sciences, μTAS 2018*, pages 889–892, 2018.

[130] Ingo Klimant and Otto S Wolfbeis. Oxygen-sensitive luminescent materials based on silicone-soluble ruthenium diimine complexes. *Analytical chemistry*, 67(18):3160–3166, 1995.

[131] Seyed Ali Mousavi Shaegh, Fabio De Ferrari, Yu Shrike Zhang, Mahboubeh Nabavinia, Niema Binth Mohammad, John Ryan, Adel Pourmand, Eleanor Laukaitis, Ramin Banan Sadeghian, Akhtar Nadhman, et al. A microfluidic optical platform for real-time monitoring of ph and oxygen in microfluidic bioreactors and organ-on-chip devices. *Biomicrofluidics*, 10(4):044111, 2016.

[132] Vishal Sharma, Ramandeep Kaur, Archana Bhatnagar, and Jagdeep Kaur. Low-ph-induced apoptosis: role of endoplasmic reticulum stress-induced calcium permeability and mitochondria-dependent signaling. *Cell stress and chaperones*, 20(3):431–440, 2015.

[133] Santiago Solé-Domènech, Dana L Cruz, Estibaliz Capetillo-Zarate, and Frederick R Maxfield. The endocytic pathway in microglia during health, aging and alzheimer's disease. *Ageing research reviews*, 32:89–103, 2016.

[134] Kyungmin Ji, Linda Mayernik, Kamiar Moin, and Bonnie F Sloane. Acidosis and proteolysis in the tumor microenvironment. *Cancer and Metastasis Reviews*, 38(1-2):103–112, 2019.

[135] Gabriel Helmlinger, Fan Yuan, Marc Dellian, and Rakesh K Jain. Interstitial ph and po 2 gradients in solid tumors in vivo: high-resolution measurements reveal a lack of correlation. *Nature medicine*, 3(2): 177–182, 1997.

[136] Shumaila Islam, Hazri Bakhtiar, Shahzad Naseem, Muhammad Safwan Bin Abd Aziz, Noriah Bidin, Saira Riaz, and Jalil Ali. Surface functionality and optical properties impact of phenol red dye on mesoporous silica matrix for fiber optic ph sensing. *Sensors and actuators A: Physical*, 276:267–277, 2018.

[137] Massimo Mastrangeli, Sylvie Millet, Janny van den Eijnden-van Raaij, et al. Organ-on-chip in development: towards a roadmap for organs-on-chip. 2019.

[138] 2021. `https://emulatebio.com/products-services/` [Accessed: 12 Aug 2021].

[139] Greenfield Sluder and Joshua J Nordberg. Microscope basics. *Methods in cell biology*, 114:1–10, 2013.

[140] Lance Davidson and Raymond Keller. Basics of a light microscopy imaging system and its application in biology. In *Methods in Cellular Imaging*, pages 53–65. Springer, 2001.

[141] Yun Wook Hwang and Min Soo Kim. The pressure drop in microtubes and the correlation development. *International journal of heat and mass transfer*, 49(11-12):1804–1812, 2006.

[142] Kevin Ward and Z Hugh Fan. Mixing in microfluidic devices and enhancement methods. *Journal of Micromechanics and Microengineering*, 25(9):094001, 2015.

[143] Edward M Purcell. Life at low reynolds number. *American journal of physics*, 45(1):3–11, 1977.

[144] Marijke Huysmans and Alain Dassargues. Review of the use of péclet numbers to determine the relative importance of advection and diffusion in low permeability environments. *Hydrogeology Journal*, 13(5): 895–904, 2005.

[145] Xueye Chen, Tiechuan Li, Hong Zeng, Zengliang Hu, and Baoding Fu. Numerical and experimental investigation on micromixers with serpentine microchannels. *International Journal of Heat and Mass Transfer*, 98:131–140, 2016.

[146] COMSOL Multiphysics. Introduction to comsol multiphysics®. *COMSOL Multiphysics, Burlington, MA, accessed Feb*, 9:2018, 1998.

[147] S Kendig. Use of microchannels to determine diffusion of food coloring in water. *Microelectronics Processing Technology Fall Term*, 2003.

[148] JMPQ Delgado. Molecular diffusion coefficients of organic compounds in water at different temperatures. *Journal of phase Equilibria and Diffusion*, 28(5):427–432, 2007.

[149] Scherrine Tria, Leslie H Jimison, Adel Hama, Manuelle Bongo, and Róisín M Owens. Sensing of egta mediated barrier tissue disruption with an organic transistor. *Biosensors*, 3(1):44–57, 2013.

[150] Ismael J Hidalgo, Thomas J Raub, and Ronald T Borchardt. Characterization of the human colon carcinoma cell line (caco-2) as a model system for intestinal epithelial permeability. *Gastroenterology*, 96(2):736–749, 1989.

[151] Siân E Hughes. Functional characterization of the spontaneously transformed human umbilical vein endothelial cell line ecv304: Use in anin vitromodel of angiogenesis. *Experimental cell research*, 225(1): 171–185, 1996.